

Sampling from high-dimensional, multimodal distributions using automatically tuned, tempered Hamiltonian Monte Carlo

Joonha Park

Department of Mathematics, University of Kansas
1460 Jayhawk Blvd. Lawrence, KS 66045, USA
email: j.park@ku.edu

Abstract

Hamiltonian Monte Carlo (HMC) is widely used for sampling from high-dimensional target distributions with probability density known up to proportionality. While HMC possesses favorable dimension scaling properties, it encounters challenges when applied to strongly multimodal distributions. Traditional tempering methods, commonly used to address multimodality, can be difficult to tune, particularly in high dimensions. In this study, we propose a method that combines a tempering strategy with Hamiltonian Monte Carlo, enabling efficient sampling from high-dimensional, strongly multimodal distributions. Our approach involves proposing candidate states for the constructed Markov chain by simulating Hamiltonian dynamics with time-varying mass, thereby searching for isolated modes at unknown locations. Moreover, we develop an automatic tuning strategy for our method, resulting in an automatically-tuned, tempered Hamiltonian Monte Carlo (ATHMC). Unlike simulated tempering or parallel tempering methods, ATHMC provides a distinctive advantage in scenarios where the target distribution changes at each iteration, such as in the Gibbs sampler. We numerically show that our method scales better with increasing dimensions than an adaptive parallel tempering method and demonstrate its efficacy for a variety of target distributions, including mixtures of log-polynomial densities and Bayesian posterior distributions for a sensor network self-localization problem.

1 Introduction

Hamiltonian Monte Carlo (HMC) is a class of Markov chain Monte Carlo (MCMC) algorithms that leverage Hamiltonian dynamics to sample from unnormalized target densities (Duane et al., 1987). HMC exhibits superior scaling properties in high-dimensional spaces compared to other commonly used MCMC algorithms such as random-walk Metropolis or the Metropolis-adjusted Langevin algorithm (MALA). This advantage arises from its utilization of local geometric information regarding the log target density function to propose global moves (Roberts et al., 1997; Roberts and Rosenthal, 1998; Beskos et al., 2013; Neal, 2011). The favorable scalability has propelled HMC into widespread adoption across various domains, including Bayesian data analysis (Gelman et al., 2013; Neal, 2012; Brooks et al., 2009; Landau and Binder, 2021).

However, in the case of strongly multimodal target distributions, HMC methods often encounter challenges in efficiently exploring multiple modes. These challenges manifest in constructed Markov chains that exhibit infrequent transitions between modes (Mangoubi

et al., 2018). Furthermore, depending on the initial state, these chains may fail to visit globally dominant modes, potentially leading to a misrepresentation of the target distribution. One potential strategy to address this issue involves running parallel chains with diverse initial states to enhance the likelihood of identifying dominant modes. However, the proportion of chains settling into different local modes might not accurately reflect the relative probabilities associated with those modes.

Numerous strategies have been developed in the literature to address efficient sampling from multimodal target distributions. One class of methods involve utilizing optimization procedures to identify the locations and approximate shapes of the modes within the target posterior, subsequently constructing an MCMC kernel facilitating transitions between these modes (Andricioaei et al., 2001; Sminchisescu and Welling, 2011; Pompe et al., 2020). Darting Monte Carlo, for instance, employs an independent Metropolis-Hastings (MH) sampler that proposes candidates near known mode locations (Andricioaei et al., 2001; Sminchisescu and Welling, 2011). A practical extension suggested by Ahn et al. (2013) involves adaptively tuning the independent MH sampler using parallel chains at regeneration times. These methods often rely on approximating the target distribution with models like mixtures of truncated normal distributions, with parameters estimated using the chain’s history. However, such approximations may become inaccurate and challenging to implement as the dimension of the space increases.

Tempering is a strategy that involves using a series of auxiliary distributions, often obtained by raising the target density to a certain power known as the inverse temperature. These auxiliary distributions facilitate transitions between isolated modes, with points in low-density regions being more frequently drawn when the inverse-temperature level is set to a low level. Simulated tempering, introduced by Marinari and Parisi (1992), constructs a Markov chain targeting a mixture of tempered distributions at different temperature levels. Effective sampling with simulated tempering requires careful selection of mixture weights for the tempered distributions, which may be achieved through adaptive tuning techniques, such as those proposed by Wang and Landau (2001) and Atchadé and Liu (2010). Parallel tempering, proposed by Swendsen and Wang (1986) and Geyer (1991), involves constructing parallel chains, each targeting a different tempered distribution. Similarly, the equi-energy sampler, introduced by Kou et al. (2006), employs parallel chains targeting distributions at various temperatures. However, unlike parallel tempering, state exchanges in the equi-energy sampler occur exclusively between points within the same potential energy band. The tempered transitions method, developed by Neal (1996), applies a series of transition kernels corresponding to a sequence of decreasing and increasing inverse temperature levels, facilitating exploration of the target distribution.

In this paper, we propose a method that combines Hamiltonian Monte Carlo with the tempered transitions method to facilitate frequent mode transitions in high-dimensional and multimodal target distributions. The method, termed as Tempered Hamiltonian Monte Carlo (THMC), efficiently explores unknown modes in high dimensions by utilizing the gradient of the negative log target density function, denoted by $U(x)$. Our approach involves simulating Hamiltonian dynamics for the potential energy function $U(x)$, while modulating the mass of the simulated particle according to a predetermined schedule. During the first half of the simulation path, the mass gradually increases, providing the necessary energy to traverse low-probability regions between modes. During the second half of the simulation, the mass

gradually decreases, allowing the particle to settle in another mode. Our contributions in this paper include the development of an automatic tuning algorithm for tempered HMC through an in-depth analysis of the simulated Hamiltonian dynamics. The automatically-tuned, tempered HMC algorithm possesses favorable dimension scaling properties and offers particular advantages when integrated into a Gibbs sampler framework, as elaborated in detail in Sections 4.3 and 4.4.

The remainder of the paper is organized as follows. Section 2 gives a brief review of standard Hamiltonian Monte Carlo and examines the challenges it faces when dealing with multimodal target distributions. We introduce a toy algorithm that involves mass enhancement and discuss its limitations, motivating our tempered Hamiltonian Monte Carlo (THMC) method. In Section 3, we present the THMC algorithm in detail, utilizing alternative formulations of Hamiltonian dynamics that provide insights into how the method works. Section 4 delves into an automatic tuning strategy for THMC and demonstrates the efficacy of our method using a mixture of log-polynomial distributions. In particular, we show that our automatically tuned, tempered HMC possesses significantly improved dimension scaling properties relative to an adaptive parallel tempering method. In Section 5, we explore applications of the method to a sensor network self-localization problem. Section 6 provides a review of recent approaches for sampling from multimodal distributions. Lastly, Section 7 concludes with a reflection on potential avenues for further research. An R package implementing our automatically tuned, tempered Hamiltonian Monte Carlo algorithm is available at <https://github.com/joonhap/athmc>. All source codes used to carry out numerical experiments in this paper are provided as supplementary materials.

2 Hamiltonian Monte Carlo and multimodality

2.1 Hamiltonian Monte Carlo

We consider a target density

$$\bar{\pi}(x) = \pi(x) / \int_{\mathbf{X}} \pi(x) dx$$

defined on space $\mathbf{X} = \mathbb{R}^d$. The unnormalized density $\pi(x)$ can be evaluated pointwise, but its normalizing constant is unknown. A broad class of MCMC methods including HMC and some variants of the bouncy particle sampler (Vanetti et al., 2017; Bouchard-Côté et al., 2018; Park and Atchadé, 2020) targets density $\Pi(x, v) = \bar{\pi}(x)\psi(v)$ defined on the augmented space $\mathbf{X} \times \mathbf{V} = \mathbb{R}^{2d}$ and having $\bar{\pi}(x)$ as its marginal density. The density $\psi(v)$ for the auxiliary *velocity* variable is often chosen as $\psi(v) = \phi(v; 0, M^{-1})$, the multivariate normal density with mean 0 and variance M^{-1} . The matrix M is symmetric, positive definite, and is viewed as the *mass* of the particle in analogy with Hamiltonian mechanics. In Hamiltonian Monte Carlo (HMC), a candidate for the next state of the constructed Markov chain is obtained by simulating Hamiltonian dynamics

$$\frac{dx}{dt} = v, \quad \frac{dv}{dt} = -M^{-1} \frac{\partial U}{\partial x}, \quad (1)$$

where $U(x) := -\log \pi(x)$ is called the potential energy ¹. Equation (1) is referred to as Hamiltonian equations of motion (HEM). The Hamiltonian is defined as the sum of the potential energy $U(x)$ and the kinetic energy $K(v)$, where $K(v) = \frac{1}{2}v^\top Mv$. The Hamiltonian represents the total energy of a particle at location x having velocity v . Given the i -th state $X^{(i)}$ of the Markov chain constructed by HMC, a candidate for the $i+1$ -st state is obtained by numerically simulating the Hamiltonian dynamics for a certain time duration t starting from $x(0) = X^{(i)}$ with initial velocity $v(0)$ drawn from $\mathcal{N}(0, M^{-1})$. The end point of the numerically simulated path, denoted by $\Psi_t(x(0), v(0))$, serves as the proposed candidate. Its x -component is accepted as $X^{(i+1)}$ if and only if

$$\Lambda < \exp \left[-H\{\Psi_t(x(0), v(0))\} + H\{x(0), v(0)\} \right] \cdot \left| \frac{\partial \Psi_t(x(0), v(0))}{\partial(x(0), v(0))} \right|, \quad (2)$$

where Λ is a Uniform(0, 1) random variable drawn independently of all other Monte Carlo draws. If (2) is not satisfied, $X^{(i+1)}$ is equal to $X^{(i)}$.

A commonly used numerical approximation method for solving the HEM is called the leapfrog method (Duane et al., 1987; Leimkuhler and Reich, 2004). One leapfrog step approximately simulates the time evolution of the Hamiltonian dynamics for time duration ϵ . It alternately updates the velocity and position (x, v) in half steps as follows:

$$\begin{aligned} v\left(t + \frac{\epsilon}{2}\right) &= v(t) - \frac{\epsilon}{2} \cdot M^{-1} \cdot \nabla U(x(t)) \\ x(t + \epsilon) &= x(t) + \epsilon v\left(t + \frac{\epsilon}{2}\right) \\ v(t + \epsilon) &= v\left(t + \frac{\epsilon}{2}\right) - \frac{\epsilon}{2} \cdot M^{-1} \cdot \nabla U(x(t + \epsilon)). \end{aligned} \quad (3)$$

The time increment unit ϵ will be referred to as the leapfrog step size. Since each line in (3) is a translation of either v or x by an amount determined by the other variable, the Jacobian determinant of the leapfrog update is equal to unity. Therefore, the numerical integrator constructed by the leapfrog method preserves the volume element:

$$\left| \frac{\partial \Psi_t(x, v)}{\partial(x, v)} \right| \equiv 1.$$

Denoting by \mathcal{S}_ϵ the leapfrog update (3) from $(x(t), v(t))$ to $(x(t + \epsilon), v(t + \epsilon))$ and $\mathcal{T}(x, v) := (x, -v)$, we can check that the numerical solution map $\Psi_{K\epsilon} = \mathcal{S}_\epsilon^K$ satisfies the time-reversibility property:

$$\mathcal{T} \circ \mathcal{S}_\epsilon^K \circ \mathcal{T} \circ \mathcal{S}_\epsilon^K(x, v) = (x, v), \quad \forall(x, v) \in \mathbf{X} \times \mathbf{V}. \quad (4)$$

The numerical stability of the leapfrog method depends on its step size ϵ . For instance, if the target density is multivariate normal with covariance Σ , the numerical error diverges exponentially fast if and only if the step size ϵ is greater than twice the square root of the smallest eigenvalue of ΣM . From this observation, we can speculate that the numerical stability of the leapfrog method is critically dependent on the relative size of its step size to the inverse square root of the largest eigenvalue of the Hessian of the log target density.

¹Usually the Hamiltonian dynamics is described in terms of the position variable x and the momentum variable p , but in this paper we analyze it using x and $v = M^{-1}p$ for convenience.

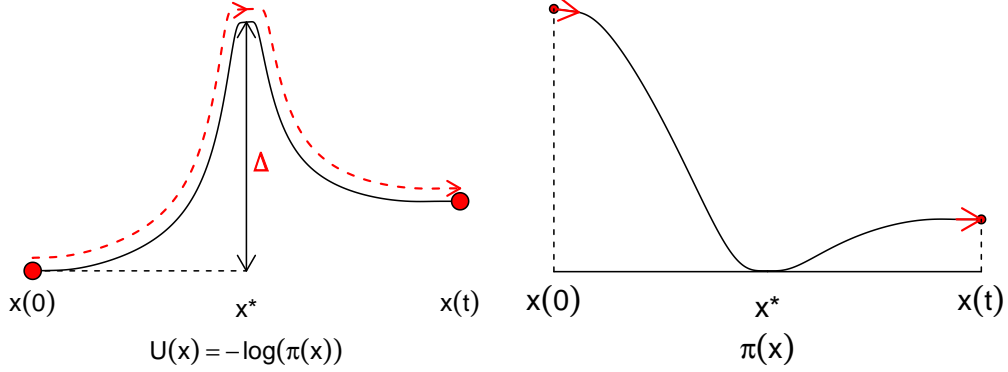


Figure 1: An illustrative diagram of the Hamiltonian path traversing a region of low target probability density.

Provided that ϵ is sufficiently small, the numerical integration by the leapfrog method possesses long-term numerical accuracy. This is due to the symplecticness of Ψ_t , meaning that it satisfies

$$\left(\frac{\partial \Psi_t(x, p)}{\partial(x, p)} \right)^\top J^{-1} \left(\frac{\partial \Psi_t(x, p)}{\partial(x, p)} \right) = J^{-1}, \quad \text{where } J = \begin{pmatrix} 0 & I_d \\ -I_d & 0 \end{pmatrix}$$

(Leimkuhler and Reich, 2004). Consequently, the Hamiltonian of the numerical solution is close to the initial Hamiltonian for a long period of time:

$$H\{\Psi_t(x(0), v(0))\} \approx H\{x(0), v(0)\}.$$

Due to the long term stability and volume preservation, the probability of accepting the candidate $\Psi_t(x(0), v(0))$ according to the criterion (2) can be arbitrarily close to one if we employ a sufficiently small leapfrog step size.

When the target distribution is multimodal, HMC typically fails to visit separated modes. Denoting $(x(s), v(s)) = \Psi_s(x(0), v(0))$, we have

$$H\{x(0), v(0)\} = U\{x(0)\} + K\{v(0)\} \approx H\{x(s), v(s)\} = U\{x(s)\} + K\{v(s)\}.$$

Consequently, the maximum potential energy increment along the path,

$$\Delta := \max_{0 \leq s \leq t} U\{x(s)\} - U\{x(0)\} = -\log \frac{\min_{0 \leq s \leq t} \pi(x(s))}{\pi(x(0))},$$

is approximately bounded above by the initial kinetic energy $K\{v(0)\}$. Figure 1 schematically illustrates the potential energy $U(x)$ and the target density $\pi(x)$ for a path that connects two isolated modes. Since $v(0)$ is drawn from $\mathcal{N}(0, M^{-1})$, we have

$$2K(v(0)) = v(0)^\top M v(0) = \|M^{1/2} v(0)\|_2^2 \sim \chi_d^2,$$

where χ_d^2 denotes the chi-squared distribution with d degrees of freedom. Therefore, if there are isolated modes in the target distribution π , the probability that a path starting from one mode reaches another has a Chernoff bound

$$\mathcal{P}(K(v(0)) > \Delta) = \mathcal{P}(\chi_d^2 > 2\Delta) \leq \left(\frac{2\Delta}{d} \right)^{d/2} e^{\frac{d}{2} - \Delta}. \quad (5)$$

The probability (5) is independent of the choice of M and decreases exponentially fast as Δ increases. Due to this fact, standard HMC has a poor global mixing property for highly multimodal target distributions.

2.2 Simulation of the Hamiltonian dynamics with enhanced mass

In order to construct paths connecting isolated modes of the target distribution, we may simulate Hamiltonian dynamics with increased mass $\check{M} = \alpha M$ with $\alpha > 1$. The increased initial kinetic energy $\check{K}(v(0)) := \frac{1}{2}v(0)^\top \check{M}v(0) = \alpha K(v(0))$ enables the simulated particle to traverse regions between isolated modes where the potential energy $U(x)$ is high. To obtain a candidate for the next state of the Markov chain, we numerically solve a modified HEM given by

$$\frac{dx}{dt} = v, \quad \frac{dv}{dt} = -\check{M}^{-1} \frac{\partial U}{\partial x} \quad (6)$$

for a certain duration t . The candidate, denoted by $\check{\Psi}_t(x(0), v(0))$, is accepted if it satisfies the same condition (2) as standard HMC, namely

$$\Lambda < \exp \left[-H\{\check{\Psi}_t(x(0), v(0))\} + H\{x(0), v(0)\} \right] \cdot \left| \frac{\partial \check{\Psi}_t(x(0), v(0))}{\partial(x(0), v(0))} \right|, \quad (7)$$

where $\Lambda \sim \text{Uniform}(0, 1)$. The Jacobian determinant for $\check{\Psi}_t(\cdot, \cdot)$ is equal to unity if the leapfrog method is used for numerical simulation. This method, which we call *mass-enhanced HMC*, is discussed in detail in the supplementary text (Section S6). Here we briefly mention its shortcomings, motivating a tempered HMC algorithm developed in Section 3.

When simulating Hamiltonian dynamics with enhanced mass, the particle may escape the local basin it starts from thanks to its increased kinetic energy. However, the path simulated for a fixed time duration t will end at a high potential energy point with high probability. To address this issue, we stop the simulation as soon as the condition (7) is satisfied for a certain number (say L) of times during the recursive leapfrog steps, where a *common value* of Λ is used for all intermediate points. The stopped position becomes the next state of the Markov chain. This method constructs Markov chains with stationary distribution $\bar{\pi}$ for any choice of $L \geq 1$ (Park and Atchadé, 2020; Campos and Sanz-Serna, 2015). This strategy of considering a sequence of proposals can be applied generally for MCMC methods involving Metropolis-Hastings-type acceptance or rejection. A chain constructed by the sequential proposal strategy follows the same law as that constructed using the delayed rejection method proposed by Mira (2001).

Mass-enhanced HMC can efficiently sample from multimodal target distributions when the dimension is low (say $d \lesssim 5$). However, in high-dimensional spaces, the simulated path with enhanced mass \check{M} generally has a low probability of ever approaching local minima of the potential function. To address this challenge, we instead increase and then decrease the mass gradually along the simulated path, allowing the particle to settle near a local minimum by the end of the simulation. We elaborate on this method, termed as tempered Hamiltonian Monte Carlo (Algorithm 1), in Section 3.

Neal (2011) proposed a method that is equivalent to tempered Hamiltonian Monte Carlo under a certain setting by employing an alternative, velocity scaling, approach. Our results show that this velocity scaling method proposed by Neal (2011) in Section 5.5.7 is sub-optimal

unless the potential energy function is locally quadratic. The relationship between Neal (2011)’s method and our tempered HMC method is elaborated in supplementary section S4. In the current paper, we delve into optimal tuning of the method and develop an automatic tuning algorithm.

3 Tempered Hamiltonian Monte Carlo

3.1 Two equivariance properties of the Hamiltonian equations of motion

In this section, we consider two equivariance properties of the Hamiltonian equations of motion (1) relevant for our development of tempered Hamiltonian Monte Carlo (Algorithm 1) and the automatic tuning algorithm (Algorithm 2). The *mass–temperature scale equivariance* property elucidates the connection between tempering and mass scaling. The *mass–time scale equivariance* property provides insights into the selection of the leapfrog step size and the mass scaling schedule for Hamiltonian dynamics.

Mass–temperature scale equivariance. Tempering techniques, often used for sampling from multimodal distributions, can be analogized to raising or lowering the temperature of a physical system. When a physical system is in thermal contact with an outside system at constant temperature T , its internal configurations form a canonical ensemble, where a certain configuration denoted by x and having internal energy $U(x)$ occurs with a probability proportional to $e^{-U(x)/T}$. Thus mathematically, increasing the temperature from $T = 1$ to $T = \alpha (> 1)$ is equivalent to scaling down the energy function from $U(x)$ to $\alpha^{-1}U(x)$. As α increases, the degree of multimodality of the target density $\check{\pi}(x) \propto \pi^{\alpha^{-1}U(x)}$ decreases, allowing more frequent transitions between modes.

The modified HEM

$$\frac{dx}{dt} = v, \quad \frac{dv}{dt} = -M^{-1} \frac{\partial \alpha^{-1}U}{\partial x} = -(\alpha M)^{-1} \frac{\partial U}{\partial x} \quad (8)$$

indicate that the HEM for temperature $T = \alpha$ and mass M are equivalent to those for $T = 1$ and $\check{M} = \alpha M$:

$$(M, T = \alpha) \quad \overset{\text{equivalent}}{\longleftrightarrow} \quad (\check{M} = \alpha M, T = 1). \quad (9)$$

Mass–time scale equivariance. Another equivariance property of HEM is obtained by considering a new time scale and a new pair of variables

$$d\check{t} := \alpha^{1/2} dt, \quad \check{v} := \alpha^{-1/2} v. \quad (10)$$

If (x, v, t) satisfies the HEM (1), then $(x, \check{v}, \check{t})$ satisfies

$$\begin{aligned} \frac{dx}{d\check{t}} &= \alpha^{-1/2} \frac{dx}{dt} = \alpha^{-1/2} v = \check{v}, \\ \frac{d\check{v}}{d\check{t}} &= \frac{\alpha^{-1/2} dv}{\alpha^{1/2} dt} = -\alpha^{-1} M^{-1} \frac{\partial U}{\partial x} = -\check{M}^{-1} \frac{\partial U}{\partial x}, \end{aligned} \quad (11)$$

Equation (11) shows that $(x, \check{v}, \check{t})$ solves the HEM with mass $\check{M} = \alpha M$, establishing a mass-time scale equivariance:

$$(dt, v, M) \underset{\text{equivalent}}{\longleftrightarrow} (d\check{t} = \alpha^{1/2} dt, \check{v} = \alpha^{-1/2} v, \check{M} = \alpha M). \quad (12)$$

This equivariance property indicates that when observing Hamiltonian dynamics in slow motion, the particle behaves as if it has an increased mass.

The time scale transformation (10) suggests numerical integration of (11) with a scaled leapfrog step size $\check{\epsilon} = \alpha^{1/2} \epsilon$. The path numerically simulated with initial state $(x(0), \check{v}(0)) = (x(0), \alpha^{-1/2} v(0))$, mass \check{M} , and leapfrog step size $\check{\epsilon} = \alpha^{1/2} \epsilon$ is identical to that simulated with initial state $(x(0), v(0))$, mass M , and leapfrog step size ϵ , as can be seen by the following equations.

$$\begin{aligned} \check{v} \left(\check{t} + \frac{\check{\epsilon}}{2} \right) &= \alpha^{-1/2} v \left(t + \frac{\epsilon}{2} \right) = \alpha^{-1/2} v(t) - \alpha^{-1/2} \frac{\epsilon}{2} M^{-1} \nabla U(x(t)) \\ &= \check{v}(\check{t}) - \frac{\check{\epsilon}}{2} (\alpha M)^{-1} \nabla U(x(\check{t})), \\ x(\check{t} + \check{\epsilon}) &= x(t + \epsilon) = x(t) + \epsilon v \left(t + \frac{\epsilon}{2} \right) \\ &= x(t) + \alpha^{-1/2} \check{\epsilon} \alpha^{1/2} \check{v} \left(\check{t} + \frac{\check{\epsilon}}{2} \right) \\ &= x(\check{t}) + \check{\epsilon} \check{v} \left(\check{t} + \frac{\check{\epsilon}}{2} \right), \\ \check{v}(\check{t} + \check{\epsilon}) &= \alpha^{-1/2} v(t + \epsilon) = \alpha^{-1/2} v \left(t + \frac{\epsilon}{2} \right) - \alpha^{-1/2} \frac{\epsilon}{2} M^{-1} \nabla U(x(t + \epsilon)) \\ &= \check{v} \left(\check{t} + \frac{\check{\epsilon}}{2} \right) - \frac{\check{\epsilon}}{2} (\alpha M)^{-1} \nabla U(x(\check{t} + \check{\epsilon})). \end{aligned}$$

Here $x(\check{t})$ denotes the position of the particle at \check{t} on the transformed time scale. Since \check{t} corresponds to t on the original time scale, we write $x(\check{t}) = x(t)$. The equations above show that the numerical simulation of $(x, \check{v}, \check{t})$ is stable if and only if the numerical simulation of (x, v, t) is stable.

3.2 Tempered Hamiltonian dynamics

In order to construct Hamiltonian paths that connect isolated modes, we utilize Hamiltonian dynamics with time-varying mass,

$$\frac{dx}{d\check{t}} = \check{v}, \quad \frac{d\check{v}}{d\check{t}} = -\{\alpha(\check{t})M\}^{-1} \frac{\partial U}{\partial x}, \quad (13)$$

as mentioned in Section 2.2. We let $\alpha(\check{t})$ start from $\alpha(0) = 1$, increase to its maximum value, and then decrease back to 1. We numerically simulate the dynamics (13) using the leapfrog method, where each step employs fixed mass $\alpha(\check{t})M$. We will refer to \check{t} as the *simulation time scale*, because our algorithm will numerically simulate Hamiltonian dynamics on this time scale. The numerical integration of (13) by the leapfrog method is symplectic, thereby possessing long-term accuracy provided that the leapfrog step size is sufficiently small. The

selection of the leapfrog step size will be discussed in Section 4. Throughout this paper, we will write

$$\eta = \frac{1}{2} \log \alpha, \quad \text{or} \quad \alpha := e^{2\eta}. \quad (14)$$

We showed in Section 3.1 that when α is constant, the change of time scale (10), $d\check{t} = \alpha^{1/2} dt$, transforms the original HEM (1) to another HEM with scaled mass $\check{M} = \alpha M$ and velocity $\check{v} = \alpha^{-1/2} v$. However, if α is varying, the change of time scale $dt = \alpha^{-1/2} d\check{t}$ transforms (13) into a non-Hamiltonian dynamics, where the position x and velocity $v = \alpha^{1/2} \check{v}$ satisfy

$$\begin{aligned} \frac{dx}{dt} &= \frac{dx}{d\check{t}} \cdot \frac{d\check{t}}{dt} = \check{v} \cdot \alpha^{1/2} = v, \\ \frac{dv}{dt} &= \frac{d}{d\check{t}} (e^\eta \check{v}) \cdot \frac{d\check{t}}{dt} \\ &= \left[\frac{d\check{v}}{d\check{t}} e^\eta + \check{v} e^\eta \frac{d\eta}{d\check{t}} \right] \cdot e^\eta \\ &= -\{\alpha M\}^{-1} \frac{\partial U}{\partial x} \cdot e^{2\eta} + v \frac{d\eta}{dt} \cdot \frac{dt}{d\check{t}} \cdot e^\eta \\ &= -M^{-1} \frac{\partial U}{\partial x} + v \frac{d\eta}{dt}. \end{aligned} \quad (15)$$

Numerical simulation of (15) amounts to the velocity scaling method proposed by Neal (2011) in Section 5.5.7, where the velocity is increased by a certain multiplicative factor (say ξ) after every leapfrog step for a certain number of steps and then decreased by the same factor for the same number of steps. We can view η as a cumulative log velocity scaling factor, where the change in η per leapfrog step equals $\pm \log \xi$. Section S4 in the supplementary text shows that Neal (2011)'s velocity scaling method, which simulates (15) with a constant step size ϵ , is equivalent to our tempered HMC method simulating (13) with varying leapfrog step size $\check{\epsilon} = e^\eta \epsilon$. Since the leapfrog integrator, being symplectic, possesses a long-term numerical accuracy, the numerical solution for (15) by Neal (2011)'s velocity scaling method is also accurate for long periods of time. However, this important property is not readily seen without the help of the mass-scaling formulation.

Neal (2011)'s use of constant step size ϵ corresponds to using $\check{\epsilon} = e^\eta \epsilon$ for simulating (13). When the target density is not locally Gaussian, however, this choice is not optimal, potentially leading to numerically unstable simulation paths. In Section 4, we develop a tuning strategy by considering a new time scale $d\bar{t}$, on which the dynamics possesses a certain stationarity property. Our tuning strategy suggests using leapfrog step sizes that scale as $\check{\epsilon} = e^{2a\eta} \bar{\epsilon}$ where $\bar{\epsilon}$ is a fixed baseline step size and a is a constant that depends on the polynomial degree of the growth of $U(x)$.

3.3 The tempered Hamiltonian Monte Carlo algorithm

In this section, we develop the tempered Hamiltonian Monte Carlo (THMC) algorithm in detail. A candidate for the next state of the Markov chain is proposed by numerically simulating the modified HEM (13). Formally, we employ a pair of auxiliary variables (k, \check{v}) , where k is an index for a sequence of mass scaling factors $\{\alpha_k\}$. We consider a modified target density given by

$$\Pi^{\text{mod}}(x, k, \check{v}) \propto \pi(x) \phi(\check{v}; 0, \alpha_k^{-1} M^{-1}). \quad (16)$$

Algorithm 1: Tempered Hamiltonian Monte Carlo

Input : Potential energy function $U(x) = -\log \pi(x)$; Mass matrix, M ; Mass scaling schedule, $\{\alpha_k = e^{2\eta_k}; k = 0, \frac{1}{2}, 1, \dots, K - \frac{1}{2}, K\}$; Baseline leapfrog step size, \bar{c} ; Simulation time scale coefficient, a ; Length of constructed Markov chain, I ;

```

1 Initialize: Choose  $X^{(0)}$  arbitrarily
2 for  $i \leftarrow 0 : I - 1$  do
3   Draw  $\Lambda \sim \text{Uniform}(0, 1)$ 
4   Let  $x\{0\} = X^{(i)}$  and draw  $\check{v}\{0\} \sim \mathcal{N}(0, M^{-1})$ 
5   Optionally, draw  $c \sim \text{Uniform}(0.9, 1.1)$ . Otherwise, let  $c \leftarrow 1$ 
6   for  $k \leftarrow 1 : K$  do
7     Let  $\alpha_{k-\frac{1}{2}} = e^{2\eta_{k-\frac{1}{2}}}$  and  $\check{c}_{k-\frac{1}{2}} = e^{2a\eta_{k-\frac{1}{2}}} \cdot c\bar{c}$ 
8     Let  $(x\{k\}, k, \check{v}\{k\}) \leftarrow \check{S}_1(x\{k-1\}, k-1, \check{v}\{k-1\})$  (one leapfrog step, (18))
9   end
10  Let  $\Delta H^{\text{mod}} = U(x\{K\}) + \frac{1}{2}\check{v}\{K\}^\top M\check{v}\{K\} - U(x\{0\}) - \frac{1}{2}\check{v}\{0\}^\top M\check{v}\{0\}$ 
11  if  $\Lambda < e^{-\Delta H^{\text{mod}}}$  then
12    Let  $X^{(i+1)} \leftarrow x\{K\}$ 
13  else
14    Let  $X^{(i+1)} \leftarrow X^{(i)}$ 
15  end
16 end
Output: A draw of Markov chain,  $(X^{(i)})_{i \in 1 : I}$ 

```

The modified Hamiltonian

$$H^{\text{mod}}(x, k, \check{v}) = U(x) + \frac{1}{2}\check{v}^\top \{\alpha_k M\} \check{v} - \frac{1}{2} \log \det \{\alpha_k M\} \quad (17)$$

is equal to $-\log \Pi^{\text{mod}}(x, k, \check{v})$ up to an additive constant. Note that when $\alpha_k = 1$, $H^{\text{mod}}(x, k, \check{v})$ is equal to $H(x, \check{v}) = U(x) + \frac{1}{2}\check{v}^\top M\check{v}$. The sequence of mass scaling factors $\{\alpha_k\}$ is defined for $k \in \{0, \frac{1}{2}, 1, \frac{3}{2}, \dots, K - \frac{1}{2}, K\}$, where K is an integer. It is required to satisfy $\alpha_0 = \alpha_K = 1$. For an integer k , α_k is used to evaluate the modified Hamiltonian $H^{\text{mod}}(x, k, \check{v})$ between successive leapfrog steps. For a half-integer k , α_k is used to scale the mass for each leapfrog step. For integer $k = 0, \dots, K - 1$, the k -th leapfrog step is carried out by

$$\begin{aligned} \check{S}_1(x\{k\}, k, \check{v}\{k\}) &:= (x\{k+1\}, k+1, \check{v}\{k+1\}), \text{ where} \\ \check{v}\{k + \frac{1}{2}\} &= \check{v}\{k\} - \frac{\check{c}}{2}(\alpha_{k+\frac{1}{2}}M)^{-1}\nabla U(x\{k\}) \\ x\{k+1\} &= x\{k\} + \check{c}_{k+\frac{1}{2}}\check{v}\{k + \frac{1}{2}\} \\ \check{v}\{k+1\} &= \check{v}\{k + \frac{1}{2}\} - \frac{\check{c}}{2}(\alpha_{k+\frac{1}{2}}M)^{-1}\nabla U(x\{k+1\}). \end{aligned} \quad (18)$$

Here $x\{k\}$ and $v\{k\}$ signify the position and velocity at the end of the k -th leapfrog step. The map \check{S}_1 increases k by one and carries out one leapfrog step with mass $\alpha_{k+\frac{1}{2}}M$ and step size

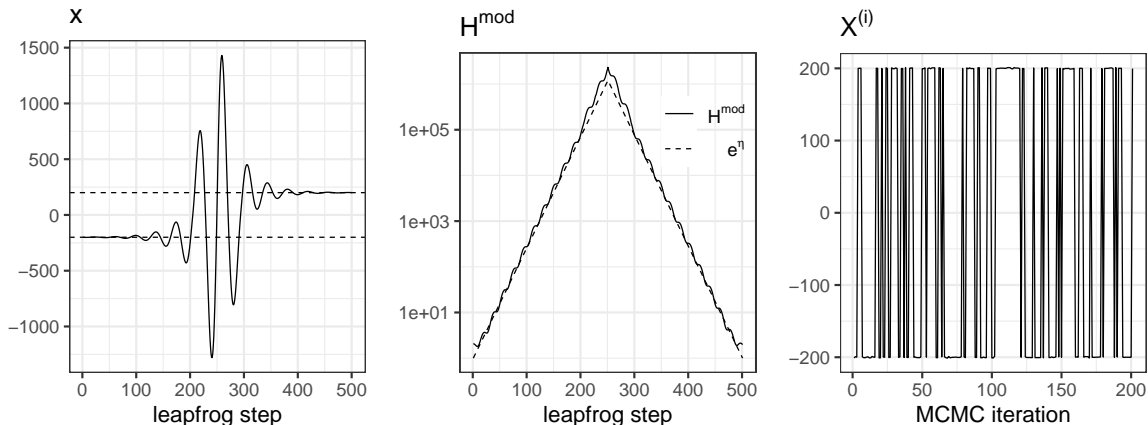


Figure 2: Left, an example trajectory constructed by tempered Hamiltonian Monte Carlo (Algorithm 1) for the target density $\frac{1}{2}\phi(x; -200, 1^2) + \frac{1}{2}\phi(x; 200, 1^2)$. The centers of the two density components are shown by the two horizontal dashed lines. Middle, the modified Hamiltonian $H^{\text{mod}}(x, k, \check{v}) = U(x) + \frac{1}{2}\check{v}^\top \{\alpha_k M\} \check{v} - \frac{1}{2} \log \det \{\alpha_k M\}$ and e^{η_k} . Right, the traceplot of the constructed Markov chain $\{X^{(i)}; i \in 1:200\}$.

ǔ. The sequence $\{\alpha_k\}$ must be symmetric in the sense that $\alpha_k = \alpha_{K-k}, \forall k$, in order to ensure detailed balance of the constructed chains. In accordance with (14), we write $\eta_k := \frac{1}{2} \log \alpha_k$. We will show in Section 4 that a desirable choice for the leapfrog step size is given by

$$\check{\epsilon}_{k+\frac{1}{2}} := \alpha_{k+\frac{1}{2}}^a \bar{\epsilon}, \quad (19)$$

for some baseline leapfrog step size $\bar{\epsilon} > 0$ and a suitably chosen constant a . In practice, perturbing $\bar{\epsilon}$ in each iteration often improves the robustness of the method. This is because the net increase in the Hamiltonian is often strongly dependent on $K\bar{\epsilon}$, the total simulation time, but not on the initial position $x\{0\}$ or the initial velocity $v\{0\}$.

The i -th iteration of tempered HMC starts with $k = 0$, $x\{0\} = X^{(i)}$, and $\check{v}\{0\}$ drawn from $\mathcal{N}(0, M^{-1})$. A candidate is obtained by $\check{\mathcal{S}}_1^K(x\{0\}, 0, \check{v}\{0\})$. Since the map $\check{\mathcal{S}}_1$ has unit Jacobian determinant, the proposed candidate is accepted if

$$\Lambda < \frac{\Pi^{\text{mod}}(x\{K\}, K, \check{v}\{K\})}{\Pi^{\text{mod}}(x\{0\}, 0, \check{v}\{0\})} = e^{-H^{\text{mod}}(x\{K\}, K, \check{v}\{K\}) + H^{\text{mod}}(x\{0\}, 0, \check{v}\{0\})}$$

where $\Lambda \sim \text{Uniform}(0, 1)$. The main focus in tuning is to reduce the average increment in the modified Hamiltonian, $H^{\text{mod}}(x\{K\}, K, \check{v}\{K\}) - H^{\text{mod}}(x\{0\}, 0, \check{v}\{0\})$. Algorithm 1 gives a pseudocode for the tempered HMC method.

The proof of the following result is given in the supplementary text.

Proposition 1. *The tempered Hamiltonian Monte Carlo algorithm (Algorithm 1) constructs a reversible Markov chain $\{X^{(i)}\}$ with respect to the target density $\bar{\pi}(x)$.*

The following bimodal example is used to demonstrate how Algorithm 1 works.

Example 0 Consider the target distribution given by a mixture of two Gaussian components

$$\frac{1}{2}\mathcal{N}(-200, 1^2) + \frac{1}{2}\mathcal{N}(200, 1^2).$$

The left plot of Figure 2 displays an example simulated Hamiltonian path constructed by Algorithm 1. This path originates from a point drawn from one of the two components, $\mathcal{N}(-200, 1^2)$. The sequence of mass scale factor is given by $\alpha_k = 14 \cdot \min(k, 500 - k) / (\frac{500}{2})$, $k \in 0:500$. As α_k increases during the first half, the simulated path oscillates over an interval much wider than the standard deviation of the initial density component. As the Hamiltonian decreases during the second half, the path settles near the other mode. The middle plot in Figure 2 demonstrates that the modified Hamiltonian H^{mod} scales almost linearly with $e^\eta = \alpha^{\frac{1}{2}}$ for this target density. In fact, Equation (23) in Section 4.1 shows that the modified Hamiltonian scales approximately as $e^{\frac{2\gamma}{\gamma+2}\eta}$ if the potential energy $U(x)$ grows polynomially with degree γ ($\gamma = 2$ for this example). The net increase in the modified Hamiltonian over the displayed path was -0.09. This might appear surprising, considering that the Hamiltonian undergoes an exponential increase and decrease along the path. However, if the sequence of mass scaling factors $\{\alpha_k\}$ and the leapfrog step sizes $\{\check{\epsilon}_{k+\frac{1}{2}}\}$ were not adequately tuned, the net increase in H^{mod} could be significantly greater than 0, leading to an extremely small acceptance probability. Addressing this issue in Section 4, we develop an automatic tuning strategy for $\{\eta_k\}$ and $\{\check{\epsilon}_k\}$. The right plot in Figure 2 illustrates the frequent transitions between the two modes in a Markov chain constructed by Algorithm 1. \square

4 Tuning strategy for tempered Hamiltonian Monte Carlo

In this section, we examine some numerical properties of Hamiltonian dynamics with time-varying mass and develop an automatic tuning algorithm (Algorithm 2) for tempered HMC.

4.1 Theoretical and numerical insight gained from the case $U(x) \propto \|x\|^\gamma$

To gain insight into the behavior of the simulated paths, we initially consider target density π defined by the expression:

$$-\log \pi(x) = U(x) \propto \|x\|_B^\gamma := (x^\top Bx)^{\gamma/2},$$

where $\gamma > 0$ and B is a symmetric positive definite matrix. Our objective is to ensure that the increment in the modified Hamiltonian $H^{\text{mod}}(x, k, \check{v})$ along the simulated path is small.

To study the stability of the modified HEM

$$\frac{dx}{d\check{t}} = \check{v}, \quad \frac{d\check{v}}{d\check{t}} = -(e^{2\eta} M)^{-1} \frac{\partial U}{\partial x}, \quad (13 \text{ revisited})$$

we introduce a time scale

$$d\bar{t} = e^{-2a\eta} d\check{t}. \quad (20)$$

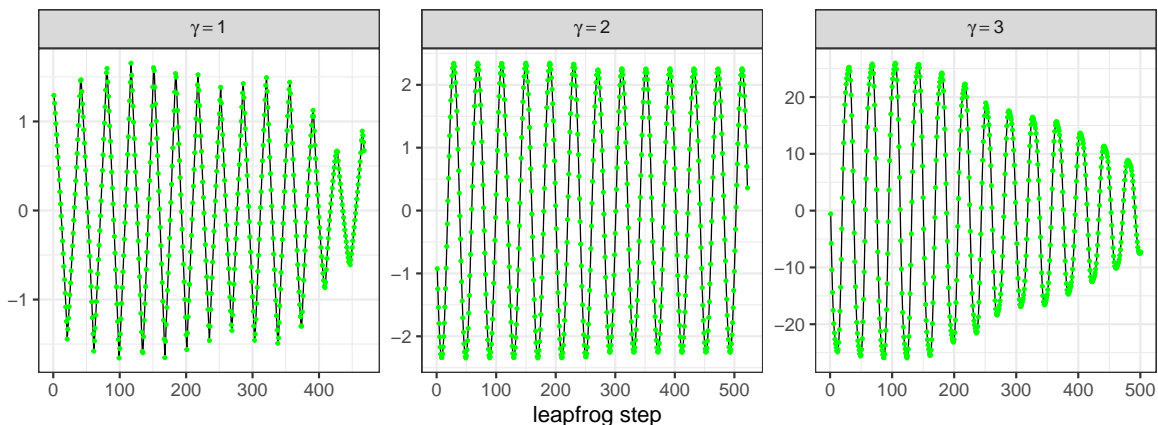


Figure 3: Traceplots for the first coordinate of the scaled velocity vector $\bar{v} = \check{v} \cdot e^{a\eta}$ for simulated paths, where the target density is given by $\pi(x) \propto e^{-\|x-\mu_1\|^\gamma} + e^{-\|x-\mu_2\|^\gamma}$, $x \in \mathbb{R}^{10000}$ with varied γ . In these simulations, we set $a = \frac{2}{\gamma+2}$, and the values of η_* , K , and ϵ were automatically tuned using Algorithm 2 developed in Section 4.2.

We note that this relationship between $d\check{t}$ and $d\bar{t}$ is consistent with the selection of the leapfrog step size $\check{\epsilon} = e^{2a\eta}\bar{\epsilon}$ (19), where $\check{\epsilon}$ represents an increment in \check{t} and $\bar{\epsilon}$ an increment in \bar{t} . We define variables

$$\bar{v} := \check{v} \cdot e^{a\eta}, \quad \bar{x} := x \cdot e^{-a\eta}. \quad (21)$$

We will refer to \bar{t} as the *tuning time scale* because the algorithm parameters will be adjusted by utilizing the approximately stationary behavior of \bar{v} on this time scale. Specifically, when $a = \frac{2}{\gamma+2}$, the solutions for $\bar{v}(\bar{t})$ and $\bar{x}(\bar{t})$ have almost constant amplitudes and frequencies if η is slowly varying. This suggests that, in an MCMC step, there is a reasonably high probability that the net increase in $U(\bar{x}) + \frac{1}{2}\bar{v}^\top M\bar{v}$ over a simulated path is close to zero or negative. We set η to zero at both the start and the end of a simulated path (i.e., $\alpha_k = 1$ for both $k = 0$ and $k = K$). At these end points, we have $\bar{x} = x$, $\bar{v} = \check{v}$, and thus

$$U(\bar{x}) + \frac{1}{2}\bar{v}^\top M\bar{v} = U(x) + \frac{1}{2}\check{v}^\top M\check{v} = H^{\text{mod}}(x, 0, \check{v}) = H^{\text{mod}}(x, K, \check{v}).$$

Hence, the net increase in $H^{\text{mod}}(x, k, \check{v})$ over a simulated path can often be close to zero or negative.

Example 1 We consider target densities given by

$$\pi(x) \propto e^{-\|x-\mu_1\|^\gamma} + e^{-\|x-\mu_2\|^\gamma}, \quad x \in \mathbb{R}^{10000}, \quad (22)$$

where $\|\mu_1 - \mu_2\| = 400$ and γ is varied.

Figure 3 demonstrates that the oscillations of $\bar{v}(\bar{t})$ are approximately stationary for simulated paths for the target density (22) for $\gamma = 1, 2$, and 3. We note that if the potential function is given by $U(x) = c\|x\|_B^\gamma$, we have

$$U(\bar{x}) = c\|\bar{x}\|_B^\gamma = e^{-\gamma a\eta}c\|x\|_B^\gamma = e^{-\gamma a\eta} \cdot U(x). \quad (23)$$

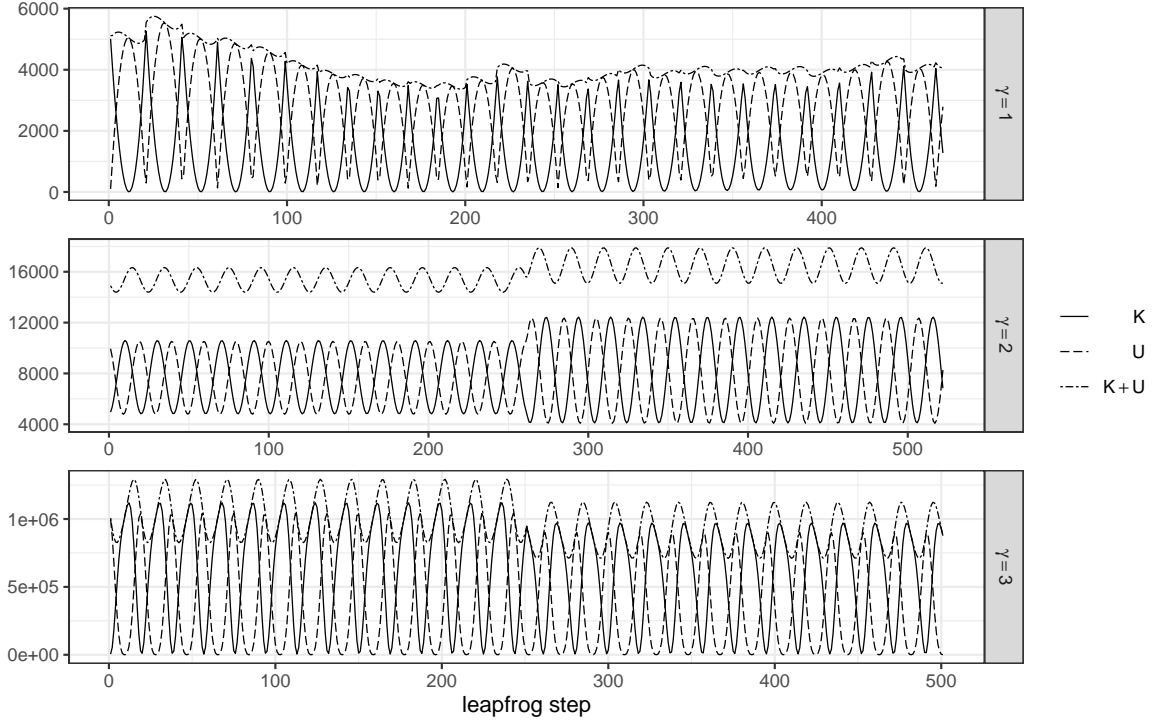


Figure 4: Traceplots for $K(\bar{v})$, $e^{-\gamma a \eta} U(x)$, and their sum for the same simulated paths shown in Figure 3.

Hence, $K(\bar{v}) = \frac{1}{2} \bar{v}^\top M \bar{v}$ and $e^{-\gamma a \eta} U(x)$ may serve as proxies for monitoring the stability of the dynamics of \bar{v} and \bar{x} as \bar{t} increases. Figure 4 plots the scaled kinetic energy $K(\bar{v}) = \frac{1}{2} \bar{v}^\top M \bar{v}$, the scaled potential energy $e^{-\gamma a \eta} U(x)$, and their sum, demonstrating that the net increase in Hamiltonian can be negative. These paths were constructed on the simulation time scale \check{t} by recursively applying the map $\check{\mathcal{S}}_1$ with leapfrog step size

$$\check{\epsilon}_{k+\frac{1}{2}} = \bar{\epsilon} \cdot e^{2a\eta_{k+\frac{1}{2}}}$$

where $a = \frac{2}{\gamma+2}$. The map $\check{\mathcal{S}}_1$ serves as an approximation to the time evolution of the modified Hamiltonian dynamics (13) for an increment of $\check{\epsilon}$ on the simulation time scale \check{t} , corresponding to a time advancement from $\bar{t} = k\bar{\epsilon}$ to $\bar{t} = (k+1)\bar{\epsilon}$ on the tuning time scale \bar{t} (see (20)). An explicit connection to the continuous time ordinary differential equations (ODE) (13) is established through $\eta(\bar{t})$ satisfying

$$\eta(k\bar{\epsilon}) = \eta_k = \frac{1}{2} \log \alpha_k, \quad k = 0, \frac{1}{2}, \dots, K.$$

Various forms of the mass scaling schedule $\{\eta_k\}$ can be considered, such as

$$\text{piecewise linear } \eta_k = \frac{2\eta_*}{K} \min\{k, K-k\}, \quad \text{or} \quad (24)$$

$$\text{sinusoidal } \eta_k = \frac{\eta_*}{2} \left\{ 1 - \cos\left(\frac{2\pi k}{K}\right) \right\}, \quad (25)$$

where $\eta_* > 0$ is the maximum of $\{\eta_k\}$.

The following results support the fact that $\bar{x}(\bar{t})$ and $\bar{v}(\bar{t})$ have approximately stationary oscillations when $a = \frac{2}{\gamma+2}$, providing a foundation on which we build tuning strategies in Section 4.2. All proofs in this section are given in the supplementary text.

Proposition 2. *Consider a potential function $U(x) \propto \|x\|_B^\gamma = (x^\top Bx)^{\gamma/2}$ where $\gamma > 0$ and B is a symmetric positive definite matrix. Then $\bar{v} := \check{v} \cdot e^{a\eta}$ and $\bar{x} := x \cdot e^{-a\eta}$ satisfy the following equations*

$$\begin{aligned} \frac{d\bar{x}}{d\bar{t}} &= \bar{v} - \bar{x} \cdot a \frac{d\eta}{d\bar{t}}, \\ \frac{d\bar{v}}{d\bar{t}} &= -e^{\{a(\gamma+2)-2\}\eta} M^{-1} \nabla U(\bar{x}) + \bar{v} \cdot a \frac{d\eta}{d\bar{t}}. \end{aligned} \tag{26}$$

When $a = \frac{2}{\gamma+2}$, the ordinary differential equation (ODE) (26) becomes time independent. In the special case where $\gamma = 2$, (26) is a linear ODE with rate matrix having zero trace. Leveraging this fact, Corollary 1 below shows that the solutions are given by stationary oscillations under certain conditions. Numerical results in Figures 3 and 4 show that the solutions are approximately stationary oscillations for other values of γ as well, which may be theoretically explained by considering (26) as a system of nonlinear differential equations perturbed from the linear one corresponding to $\gamma = 2$.

Corollary 1. *Consider the potential function given by $U(x) = \|x\|_B^2 = x^\top Bx$ (i.e., $\gamma = 2$). Let $a = \frac{2}{\gamma+2} = \frac{1}{2}$ and suppose that $d\eta/d\bar{t}$ is constant. Then $\bar{v} := \check{v} \cdot e^{a\eta}$ and $\bar{x} := x \cdot e^{-a\eta}$, the solution to (26), are linear combinations of sinusoidal functions with constant amplitude and constant frequency, provided that*

$$2\lambda_{\min}(M^{-1}B) > a^2 \left(\frac{d\eta}{d\bar{t}} \right)^2,$$

where $\lambda_{\min}(M^{-1}B)$ signifies the smallest eigenvalue of $M^{-1}B$, which is positive.

Corollary 1 suggests that the $\{\eta_k\}$ sequence should be slowly varying. The upper bound on the rate of change $d\eta/d\bar{t}$ does not depend on the space dimension d , provided that M is close to the local covariance structure of the target distribution, B . Utilizing these insights, we develop an adaptive tuning strategy in Section 4.2, where $\{\eta_k\}$ is varied sufficiently slowly by ensuring that the graph of $\bar{v}(\bar{t})$ includes at least a certain number of oscillations throughout the simulation.

Although Proposition 2 and Corollary 1 consider a unimodal potential $U(x) \propto \|x\|_B^\gamma$, the results can also be relevant for multimodal distributions where the graph of $U(x)$ is approximately a disjoint union of local basins that each looks like a unimodal basin. The plot of $\bar{v}(\bar{t})$ may exhibit somewhat altered patterns after the path crosses between unimodal basins, but the degree of change can often be mild, as demonstrated by Figure 3. In particular, Figure 4 shows that the net increase in Hamiltonian can still be negative when the simulated path traverses across local basins.

Parameter	Description	Tuning guidelines
$\{\eta_k\}$	mass scaling schedule	$\{\eta_k; k \in 0:K\}$ must be symmetric about $k = \frac{K}{2}$. Reasonable choices include piecewise linear, (24), and sinusoidal, (25), sequences.
$a = \frac{2}{\hat{\gamma}+2}$	time scale coefficient	a should be tuned such that the oscillation amplitude and frequency of $\bar{v}(\bar{t})$ are approximately constant over the simulated path. For $U(x) \propto \ x\ _B^\gamma$, the optimal value is $a = \frac{2}{\gamma+2}$.
K	period of $\{\eta_k\}$	K should be sufficiently large to ensure that the simulated path includes a sufficient number (≈ 25) of oscillation cycles of $K(\bar{v})$.
$\check{\epsilon}$	leapfrog step size	$\check{\epsilon} = \bar{\epsilon} \cdot e^{2a\eta}$.
$\bar{\epsilon}$	baseline leapfrog step size	$\bar{\epsilon}$ should be small enough to ensure that the oscillation cycles of $K(\bar{v})$ comprise a sufficient number (≈ 20) of leapfrog steps.
η_*	maximum of $\{\eta_k\}$	η_* should be large enough to ensure that the simulated path can reach isolated modes.

Table 1: Tuning guidelines for tempered Hamiltonian Monte Carlo (Algorithm 1)

4.2 Adaptive tuning strategy

In this section, we propose parameter tuning leading to candidate states that are accepted with reasonably high probabilities. Automating this tuning procedure, we develop an algorithm that facilitates fast mixing of Markov chains for a wide array of multimodal distributions.

Tuning of a and $\hat{\gamma}$. In practical applications, the degree γ of the local polynomial growth of $U(x)$ may be unknown. We develop a method for estimating γ by iterative simulations. The simulations employ $a = \frac{2}{\hat{\gamma}+2}$, where $\hat{\gamma}$ is the current estimated value for γ , for scaling the leapfrog step sizes as $\check{\epsilon} = e^{2a\eta}\bar{\epsilon}$. Figure 5 shows the plot of $\bar{v} = \check{v} \cdot e^{a\eta}$ as a function of \bar{t} where the value of $a = \frac{2}{\hat{\gamma}+2}$ is different than the optimal value $\frac{2}{\gamma+2}$. Green dots indicate the values of $\bar{v}(\bar{t})$ after each leapfrog step. If $\hat{\gamma}$ overestimates γ , the oscillation amplitude and the frequency decrease as η increases, and the opposite happens if $\hat{\gamma}$ underestimates γ .

The value of $\hat{\gamma}$ can be tuned adaptively as follows. Given a state $x(0) = X^{(i)}$ in a local basin of $U(x)$, we simulate a path for (x, \check{v}, \bar{t}) with leapfrog step sizes $\check{\epsilon} = e^{2a\eta}\bar{\epsilon}$ using an initial guess for a . We then evaluate $\bar{v} = \check{v} \cdot e^{a\eta}$ as a function of \bar{t} . Note that \bar{t} grows linearly with the number of leapfrog steps. If the oscillation amplitude of $\bar{v}(\bar{t})$ decreases with increasing η , the value of a should be increased, and in the opposite case, it should be decreased. The amount of change in a can be determined as follows. Suppose that a_{opt} is an optimal value of a , making the oscillation amplitude of $\bar{v}_{\text{opt}} = e^{a_{\text{opt}}\eta}\check{v}$ approximately constant over the simulated path. Since \bar{v} scales as $e^{a\eta}$, the oscillation amplitude of \bar{v} scales as $e^{(a-a_{\text{opt}})\eta}$. Let

$$r_j := \frac{\max_{0 \leq k < \frac{K}{8}} |\bar{v}_j\{k\}|}{\max_{\frac{3K}{8} \leq k < \frac{K}{2}} |\bar{v}_j\{k\}|}, \quad j \in 1:d, \quad (27)$$

where $|\bar{v}_j\{k\}|$ denotes the absolute value of the j -th coordinate value of the velocity $\bar{v}\{k\}$ at the end of the k -th leapfrog step. We then have approximately

$$r_j \approx e^{(a-a_{\text{opt}})\Delta\eta}$$

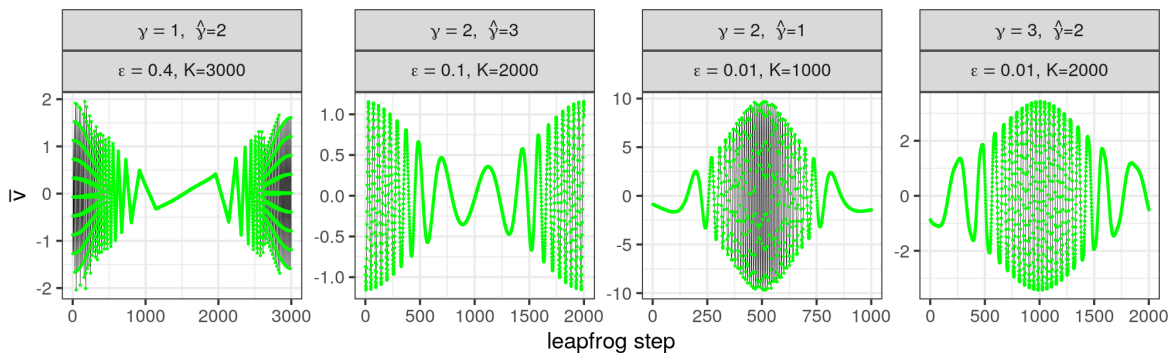


Figure 5: Traceplots for $\bar{v} = \check{v} \cdot \exp\{\frac{-2}{\hat{\gamma}+2}\eta\}$ for simulated paths where the polynomial degree γ of $U(x)$ was incorrectly estimated (i.e., $\hat{\gamma} \neq \gamma$). The $\{\eta_k\}$ sequence was given by $\eta_k = 6\{1 - \cos(2\pi k/K)\}$, and the leapfrog step size by $\check{\epsilon} = \bar{\epsilon} \cdot \exp\{\frac{4}{\hat{\gamma}+2}\eta\}$.

where $\Delta\eta = \eta_{\lfloor \frac{7K}{16} \rfloor} - \eta_{\lfloor \frac{K}{16} \rfloor}$ is the increase in η_k between the two time intervals. The optimal value a_{opt} can thus be approximated by

$$a_{\text{opt}} \approx a - \text{median}\{\log r_j; j \in 1:d\} / \Delta\eta. \quad (28)$$

The right hand side of (28) can be used for simulating the path in the next tuning step. Numerical results suggest, however, that the stability of the tuning cycles can be improved by decreasing the size of innovation, for instance by setting

$$a \leftarrow a - 0.6 \cdot \text{median}\{\log r_j; j \in 1:d\} / \Delta\eta.$$

The polynomial degree γ is estimated by $\hat{\gamma} = \frac{2}{a} - 2$, which satisfies $a = \frac{2}{\hat{\gamma}+2}$. We stop the recursive updates when $|\text{median}\{\log r_j\}|$ is less than, say, 0.2. Figure 6 shows the finally tuned values of $\hat{\gamma}$ where the starting values were varied from 0.5 to 4. The target density was given by Equation (22), where γ varied over the values of 1, 2, and 3. The tuned values of $\hat{\gamma}$ were generally close to γ . Over iterated MCMC steps, the tuned values of $\hat{\gamma}$ generally approach even closer the true value γ (see Figure 9).

Tuning of η_* . The maximum of $\{\eta_k; 0 \leq k \leq K\}$, namely η_* , determines the search scope for isolated modes, or, how far the simulated Hamiltonian paths reach. When a is suitably chosen so that $U(\bar{x})$ is stable in a local basin, $U(x) = e^{\gamma a \eta} U(\bar{x})$ (see (23)) scales approximately linearly with $e^{\gamma a \eta}$. Therefore, we should have

$$\eta_* \gtrsim O\{\log(\text{the depths of local basins of } U(x))\}.$$

A reasonable value for η_* can be found adaptively by increasing its value until the simulated path meets a certain search scope criterion. For instance, for a suitably chosen reference point $x^0 \in \mathbb{R}^d$ and coordinate-wise desired search scales $\{s_j; j \in 1:d\}$, the criterion may be characterized by

$$\begin{aligned} \text{a rectangular search scope: } & \max_{k \in 0:K} |x_j\{k\} - x_j^0| \geq s_j \text{ for all } j \in 1:d, \text{ or} \\ \text{an ellipsoidal search scope: } & \max_{k \in 0:K} \sum_{j=1}^d (x_j\{k\} - x_j^0)^2 / s_j^2 > d, \end{aligned} \quad (29)$$

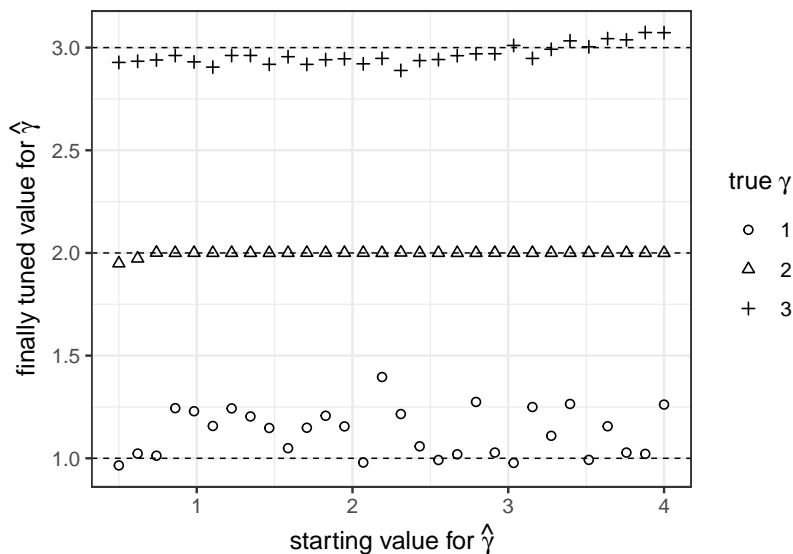


Figure 6: Automatically tuned $\hat{\gamma}$ values using the automatic tuning algorithm (Algorithm 2) for varied starting values. The bimodal target density was given by (22), where $d = 10000$ and γ was varied over $\{1, 2, 3\}$.

where $x_j\{k\}$ denotes the j -th coordinate of the position $x\{k\}$ at the end of the k -th leapfrog step.

Tuning of $\{\eta_k; k \in 0:K\}$. The value η_k for $k = 0, \frac{1}{2}, \dots, K - \frac{1}{2}, K$ can be considered as the value of $\eta(\bar{t})$ for the continuous time dynamics (26) evaluated at time points $\bar{t} = k\bar{\epsilon}$. In order to ensure that the constructed Markov chain is time-reversible with respect to the target density $\bar{\pi}$, the sequence $\{\eta_k\}$ must be symmetric about $k = K/2$. Without loss of generality, we can let the minimum of η_k over $k \in 0:K$ ($=\eta_0 = \eta_K$) equal to zero². Numerical simulations suggest that both the piecewise linear $\{\eta_k\}$ sequence (24) and the sinusoidal sequence (25) give comparable results (see Figure 8). These results imply that boundedness in the gradient of η is critical for stability of numerical simulations, whereas smoothness of η does not have significant impact.

Tuning of $\bar{\epsilon}$. The time scale $d\check{t} = e^{2a\eta}d\bar{t}$ suggests the use of leapfrog step size $\check{\epsilon} = e^{2a\eta}\bar{\epsilon}$ where $\bar{\epsilon}$ is a baseline step size. In order for the numerical simulation of $(x(\check{t}), \check{v}(\check{t}))$ to be stable and accurate, $\bar{\epsilon}$ should not be too large. An appropriate level for $\bar{\epsilon}$ can be selected by ensuring that each oscillation cycle of $\bar{v}(\bar{t})$ comprises a sufficient number of leapfrog steps. We can use $K(\bar{v}) = \frac{1}{2}\bar{v}^\top M\bar{v}$ as a proxy summarizing the oscillations of all $\bar{v}_j(\bar{t})$, $j = 1:d$. Our suggestion is to adjust $\bar{\epsilon}$ such that the median number of leapfrog steps per oscillation cycle of $K(\bar{v})$ to be around 20. That is, if we denote by m_{len} the median length of the oscillation cycles of $K(\bar{v}\{k\})$, a suggested value for $\bar{\epsilon}$ is its current value times $m_{\text{len}}/20$. This criterion can be expressed as $\bar{\epsilon} \approx \frac{1}{20}\bar{t}_0$ where \bar{t}_0 signifies the median oscillation period of $K\{\bar{v}(\bar{t})\}$ measured in \bar{t} . However, a slower recursive update $\bar{\epsilon} \leftarrow \bar{\epsilon} \cdot \sqrt{m_{\text{len}}/20}$ can help to avoid unstable tuning

²This is because if we replace η_k by $\eta'_k = \eta_k + c$ for some constant c , then the simulated path obtained through (18) remains unchanged if we use $\bar{\epsilon}' = \bar{\epsilon} \cdot e^{(-2a+1)c}$ and the initial velocity $\check{v}'(0) = \check{v}(0) \cdot e^{-c}$. This modified initial velocity follows the distribution $\check{v}'(0) \sim \mathcal{N}(0, e^{-2\eta'_0} M^{-1})$, as required by (16).

cycles.

Tuning of K . In order to check the stability of \bar{v} and to inform the tuning of a , we need to ensure that the traceplot of $K(\bar{v}) = \frac{1}{2}\bar{v}^\top M\bar{v}$ comprises a sufficient number of oscillation cycles (≈ 25). This requirement can be expressed as $K\bar{\epsilon} \approx 25\bar{t}_0$. Denoting by n_{cycle} the total number of oscillation cycles in $K(\bar{v})$, we suggest a recursive update $K \leftarrow \lceil K \cdot \sqrt{20/n_{\text{cycle}}} \rceil$, where $\lceil x \rceil$ is the smallest integer greater than x .

Recursive tuning algorithm. A recursive algorithm that automatically tunes η_* , a , K , and $\bar{\epsilon}$ according to our suggestions is given by Algorithm 2. We terminate the tuning iterations when (a) there are an adequate number of oscillation cycles of $K(\bar{v})$ in the simulated path, (b) each oscillation cycle comprises an adequate number of leapfrog steps, (c) the innovation size for a falls below a certain threshold (i.e., $|\text{median}_{j \in 1:d} \log r_j| < 0.2$), and (d) the search criterion (29) is satisfied.

Automatically tuned, tempered Hamiltonian Monte Carlo (ATHMC). Incorporating the automatic tuning algorithm (Algorithm 2) into tempered HMC (Algorithm 1), we obtain automatically tuned, tempered Hamiltonian Monte Carlo (ATHMC, Algorithm 3). For each MCMC step, the automatic tuning algorithm finds the values of η_* , $\hat{\gamma}$, K , and $\bar{\epsilon}$ suitable for the current state $X^{(i)}$. Since the values of the tuning parameters depend on $X^{(i)}$, the constructed chain may not exactly have the target $\bar{\pi}$ as its stationary density. However, if the finally tuned parameter values are approximately the same regardless of the state $X^{(i)}$, the chain may be approximately stationary with respect to $\bar{\pi}$. In order to induce convergence of parameter values, we may also gradually shrink the size of innovations as MCMC iterations progress.

We suggest using the finally tuned values for η_* , $\hat{\gamma}$, K , and $\bar{\epsilon}$ from the previous MCMC step as the starting values for the next step. This in principle introduces an auto-correlation of tuning parameters, breaking the Markovian nature of the constructed chain ($X^{(i)}$). Then the adaptive MCMC framework can be used to study the ergodicity of the constructed chains, which is ensured under a simultaneous uniform ergodicity condition and a diminishing adaptation condition (Andrieu and Thoms, 2008; Roberts and Rosenthal, 2007). Nevertheless, if the outcomes of the automatic tuning algorithm do not significantly depend on the starting values, the constructed chain will be approximately Markovian. An alternative to the adaptive MCMC approach is to freeze the tuned parameters and use those values for all later MCMC steps once the average number of tuning cycles falls below a certain threshold. The code that we used for numerical experiments in this paper is available at <https://github.com/joonhap/athmc>.

Figure 7 shows example paths simulated for the target density (22) for $\gamma = 1, 2$, and 3 , where η_* , a , K , and $\bar{\epsilon}$ were automatically tuned using Algorithm 2. A piecewise linear $\{\eta_k\}$, (24), was used. The initial point $x\{0\}$ was arbitrarily chosen close to one of the modes, μ_1 . The particle moves away from the initial mode as the total energy increases due to increasing mass, searching for isolated modes in the 10000 dimensional space by utilizing the gradient of the potential energy function. The path settles on one of the modes as the mass decreases during the second half. We note that for $\gamma = 1$, the end point of the simulation was not as close to the modes as for the other cases, $\gamma = 2$ or 3 , because the potential energy grew less steeply.

Figure 8 shows the running estimates of the probability $P_{\bar{\pi}}[\|X - \mu_1\| < \|X - \mu_2\|]$, which is equal to $\frac{1}{2}$ due to the symmetry of the two modes. The plots in Figure 8 show

Algorithm 2: Automatic tuning algorithm for η_* , $a = \frac{2}{\hat{\gamma}+2}$, K , and $\bar{\epsilon}$

Input : $x\{0\} = X^{(i)}$, the current (i -th) state of the constructed Markov chain; $\check{v}\{0\}$, initial velocity drawn from $N(0, M^{-1})$; Mass matrix, M ; Starting values $\eta_{*,0}$, $a_0 = \frac{2}{\hat{\gamma}_0+2}$, K_0 , and $\bar{\epsilon}_0$ for tuning; Maximum number of tuning iteration steps, l_{\max}

1 **initialize:** Let $\eta_* \leftarrow \eta_{*,0}$, $a \leftarrow a_0$, $K \leftarrow K_0$, $\bar{\epsilon} \leftarrow \bar{\epsilon}_0$
2 **for** $l \leftarrow 1:l_{\max}$ **do**
3 Let $\eta_k = \frac{2\eta_*}{K} \min\{k, K - k\}$ for $0 \leq k \leq K$ (or use a sinusoidal alternative)
4 **for** $k \leftarrow 1:K$ **do**
5 Let $\alpha_{k-\frac{1}{2}} = e^{2\eta_{k-\frac{1}{2}}}$ and $\check{\epsilon}_{k-\frac{1}{2}} = e^{2a\eta_{k-\frac{1}{2}}} \cdot \bar{\epsilon}$
6 Let $(x\{k\}, k, \check{v}\{k\}) = \check{\mathcal{S}}_1(x\{k-1\}, k-1, \check{v}\{k-1\})$ (one leapfrog step, (18))
7 Let $\bar{v}\{k\} = \check{v}\{k\} \cdot e^{a\eta_k}$ and $K(\bar{v}\{k\}) = \frac{1}{2}\bar{v}\{k\}^\top M\bar{v}\{k\}$
8 Mark the start of a new oscillation cycle of $K(\bar{v})$ when $K(\bar{v}\{k-1\})$ is smaller than both $K(\bar{v}\{k-2\})$ and $K(\bar{v}\{k\})$
9 **end**
10 Let $\Delta H^{\text{mod}} = U(x\{K\}) + \frac{1}{2}\check{v}\{K\}^\top M\check{v}\{K\} - U(x\{0\}) - \frac{1}{2}\check{v}\{0\}^\top M\check{v}\{0\}$
11 Let $n_{\text{cycle}} \leftarrow$ total number of oscillation cycles of $K(\bar{v})$
12 For each oscillation cycle of $K(\bar{v})$, find the number of leapfrog steps it comprises
13 Let $m_{\text{len}} \leftarrow$ median length of the oscillation cycles (in k)
14 Let $K \leftarrow \lceil K \cdot \sqrt{25/n_{\text{cycle}}} \rceil$ and $\bar{\epsilon} \leftarrow \bar{\epsilon} \cdot \sqrt{m_{\text{len}}/20}$
15 Let r_j be the ratio of the maxima of $|\check{v}_j\{k\}|$ between $0 \leq k < \frac{K}{8}$ and $\frac{3K}{8} \leq k < \frac{K}{2}$ (see (27))
16 Let $a \leftarrow a - 0.6 \cdot \text{median}_{j \in 1:d} \log r_j / \Delta\eta$ where $\Delta\eta = \eta_{\lfloor \frac{K}{16} \rfloor} - \eta_{\lfloor \frac{7K}{16} \rfloor}$
17 Let $\hat{\gamma} \leftarrow 2a^{-1} - 2$
18 **if** the search scope condition (29) is not met **then**
19 | Let $\eta_* \leftarrow \eta_* + 0.4$
20 **end**
21 **if** $\text{median}_{j \in 1:d} |\log r_j| < 0.2$, $10 \leq n_{\text{cycle}} \leq 100$, $10 \leq m_{\text{len}} \leq 100$, and the search scope condition (29) is met **then**
22 | Stop further tuning iterations
23 **end**
24 **end**
Output: Tuned parameters η_* , $a = \frac{2}{\hat{\gamma}+2}$, K , and $\bar{\epsilon}$

Algorithm 3: Automatically tuned, tempered HMC (ATHMC)

Initialize: Let FROZEN \leftarrow FALSE
Insert the following code between lines 4 and 5 in Algorithm 1:
if not FROZEN **then**
 Refresh $\eta_* \leftarrow \max(\eta_* - 1, 0.5)$ in order to avoid a monotonic increase in η_* over
 the MCMC steps
 Update η_* , $a = \frac{2}{\gamma+2}$, K , and $\bar{\epsilon}$ by using Algorithm 2
 Let $\eta_k = \frac{2\eta_*}{K} \min\{k, K - k\}$, $k = 0, \frac{1}{2}, \dots, K$
 Let $l_{\text{tuning}}(i)$ be the number of iterative tuning cycles for the i -th MCMC step
 (Optional) **if** $\sum_{j=i-4}^i l_{\text{tuning}}(j) < 20$ **then**
 | FROZEN \leftarrow TRUE
 end
end

the average estimates over 20 independently constructed chains plus and minus two standard errors. Fast convergence to the ergodic mean $\frac{1}{2}$ implies that the constructed chains frequently jump between the two isolated modes. For $\gamma = 1$, standard HMC, implemented by running tempered HMC with $\eta_k \equiv 0$, exhibits relatively slower convergence than ATHMC. For $\gamma = 2$ and 3, the target distribution is strongly multimodal, because $\Delta - \frac{d}{2} \approx \|\frac{\mu_1 - \mu_2}{2}\|^\gamma - \frac{d}{2} \gg 1$ in Equation 5. For these cases, not a single jump occurred between the modes when standard HMC was used. ATHMC enabled reasonably frequent jumps between the modes for all cases. The numerical results were comparable between the piecewise linear and the sinusoidal $\{\eta_k\}$ sequences, while the former led to slightly faster convergence.

4.3 Comparison with parallel tempering

We compare automatically tuned, tempered HMC (Algorithm 3) with parallel tempering, using the bimodal target density (22), $\pi(x) \propto e^{-\|x-\mu_1\|^\gamma} + e^{-\|x-\mu_2\|^\gamma}$, with $\gamma = 2$. For parallel tempering, we employed $K = 15$ parallel chains, each targeting the tempered density proportional to π^{1/α_k} where $1 = \alpha_1 < \alpha_2 < \dots < \alpha_{15}$. Adopting the strategy proposed by Syed et al. (2022), swaps between adjacent pairs of parallel chains were carried out in an alternating manner, such that in even numbered iterations the pairs $(k, k+1)$ were swapped for even k 's, and in odd numbered iterations the pairs $(k, k+1)$ were swapped for odd k 's. The temperature levels were adaptively tuned using the method proposed by Miasojedow et al. (2013). Specifically, if we denote by $p_k^{(i)}$ the acceptance probability for the swap between the k -th and the $k+1$ -st chain states on the i -th MCMC iteration, we let

$$\alpha_1^{(i+1)} = 1, \quad \alpha_{k+1}^{(i+1)} = \alpha_k^{(i+1)} + e^{\rho_k^{(i+1)}}, \quad k \in 1:K-1,$$

where

$$\rho_k^{(i+1)} = \rho_k^{(i)} + \frac{1}{(i+1)^{0.6}} (p_k^{(i)} - 0.234).$$

Here the target acceptance probability 0.234 was proposed by Kone and Kofke (2005) and Atchadé et al. (2011). The parallel chain for each temperature level was constructed using standard HMC that simulates a path with one hundred leapfrog steps of size $\epsilon = 0.5$ in each

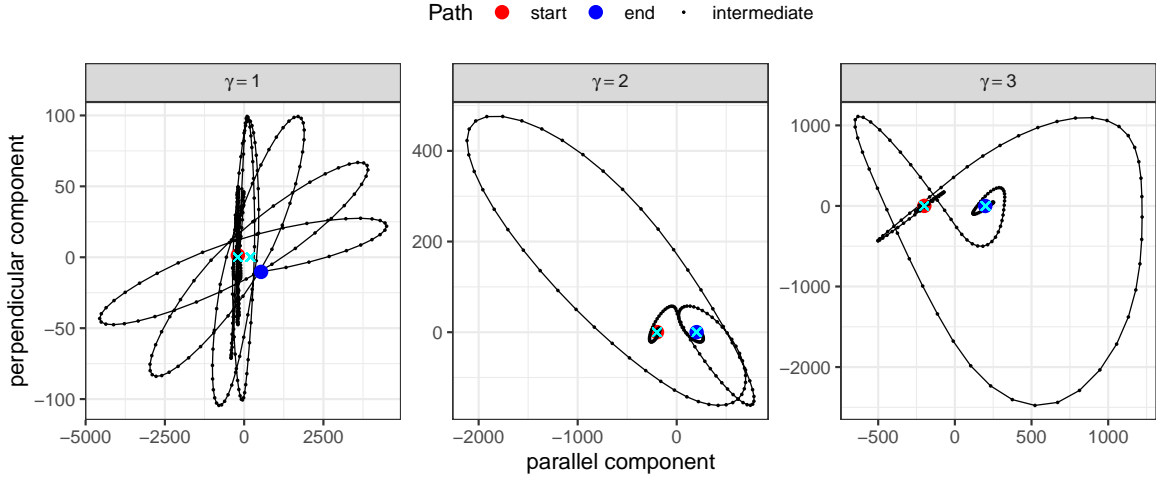


Figure 7: Example paths simulated for $d = 10,000$ dimensional target density (22) for $\gamma = 1, 2,$ and 3 . The x -axis shows the coordinate in the direction parallel to the vector $\mu_2 - \mu_1$, and the y -axis displays the coordinate in a random direction perpendicular to $\mu_2 - \mu_1$. The initial and the terminal points are marked in red and blue, respectively. The centers of the two mixture components, μ_1 and μ_2 , are indicated by cyan ‘x’.

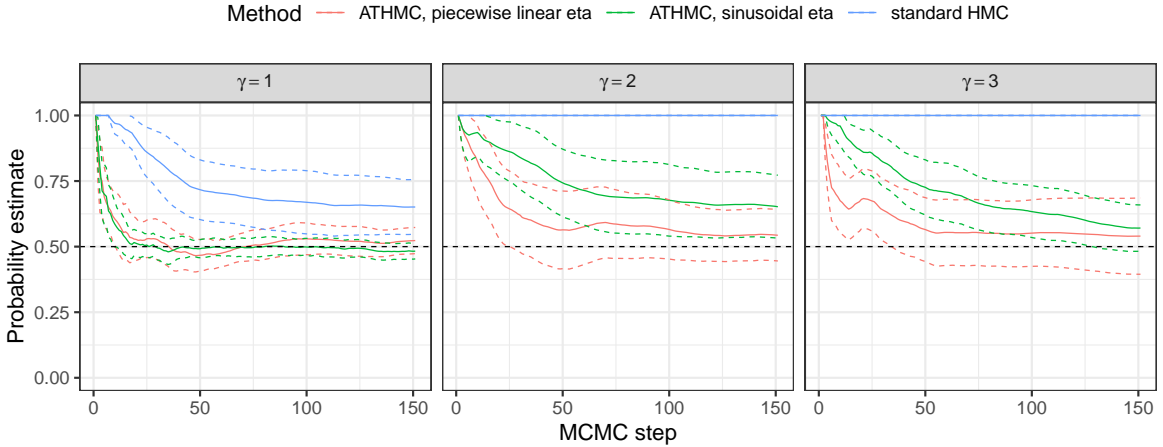


Figure 8: Running estimates of the probability $P_{\pi}[\|X - \mu_1\| < \|X - \mu_2\|]$ for the target density (22) where automatically tuned, tempered HMC (ATHMC, Algorithm 3) is used to construct chains. This probability has an exact value of $\frac{1}{2}$, thanks to the symmetry of the two modes. ATHMC employing a piecewise linear $\{\eta_k\}$ (24) and a sinusoidal $\{\eta_k\}$ (25) are compared with standard HMC, which employs constant $\eta_k \equiv 0$. The solid curves show the averages over 20 independently constructed chains, and the dashed curves mark ± 2 standard errors.

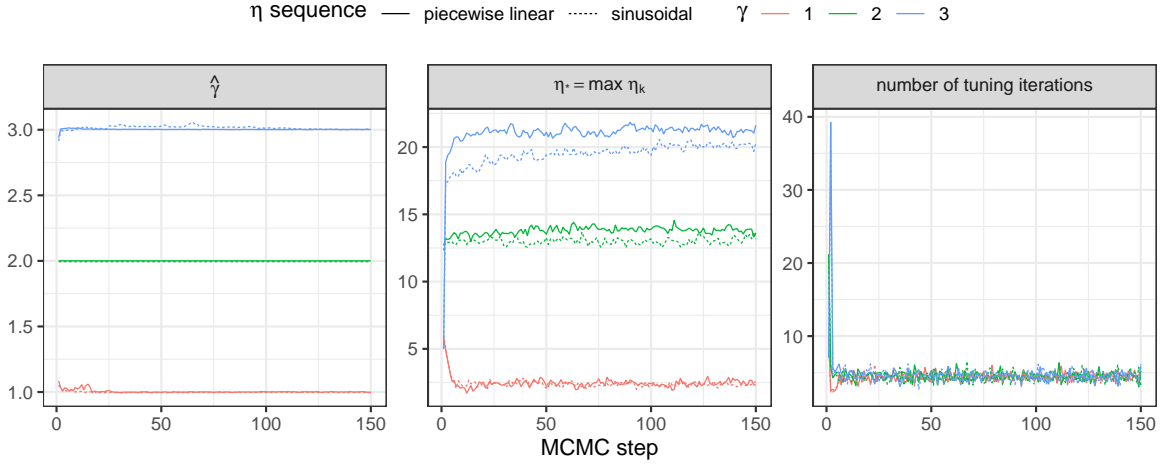


Figure 9: The tuned values for $\hat{\gamma}$ and η_* and the number of tuning cycles for the chains constructed by ATHMC (Algorithm 3). The averages over 20 independently constructed chains are shown for piecewise linear and sinusoidal $\{\eta_k\}$ sequences.

iteration. Thus in each iteration $15 \times 100 = 1500$ leapfrog steps were carried out for all parallel chains. Ten independent replications of adaptive parallel tempering were conducted for each of the settings $(d, \|\mu_1 - \mu_2\|) = (1, 400), (10, 400), (100, 400), (1000, 400), (10000, 400), (10000, 4), (10000, 40)$, where d denotes the space dimension and $\|\mu_1 - \mu_2\|$ denotes the mode separation distance.

For comparison, ATHMC was used to sample from the same target distribution ten times for each setting, where all parameters were tuned automatically. We used the rectangular search scope (29) with center point $x^0 = \mathbf{0} \in \mathbb{R}^d$ and coordinate-wise half widths given by $s_j = 1000/\sqrt{d}$ for all $j \in 1:d$ regardless of the mode separation distance. We recorded the cumulative numbers of leapfrog steps, including those carried out during the tuning process. The total number of leapfrog steps was used to represent the total computational costs for both parallel tempering and ATHMC methods.

Figure 10 shows the cumulative number of transitions between the two modes as MCMC progresses, averaged over ten replications. ATHMC enabled significantly more transitions between modes than adaptive parallel tempering. Indeed, when adaptive parallel tempering was used, the constructed chain at the lowest temperature level barely moved between the modes except when $d = 1$. Moreover, even for $d = 1$, the transitions between the modes did not happen until the temperature sequence $\{\alpha_k\}$ was suitably tuned by the adaptive method. The left panel of Figure 11 shows the number of transitions between the modes per leapfrog step for both methods for varying d where the mode separation distance $\|\mu_1 - \mu_2\| = 400$ was fixed. ATHMC exhibited significantly better scaling with increasing dimensions than adaptive parallel tempering. For ATHMC, the rate of transitions decreased approximately as $d^{-0.22}$. The right panel of Figure 11 shows the rate of transitions for varying mode separation distances where the dimension $d = 10000$ was fixed. The degree of multimodality of the target distribution did not significantly affect the rate of transitions when ATHMC was employed with the same search scope.

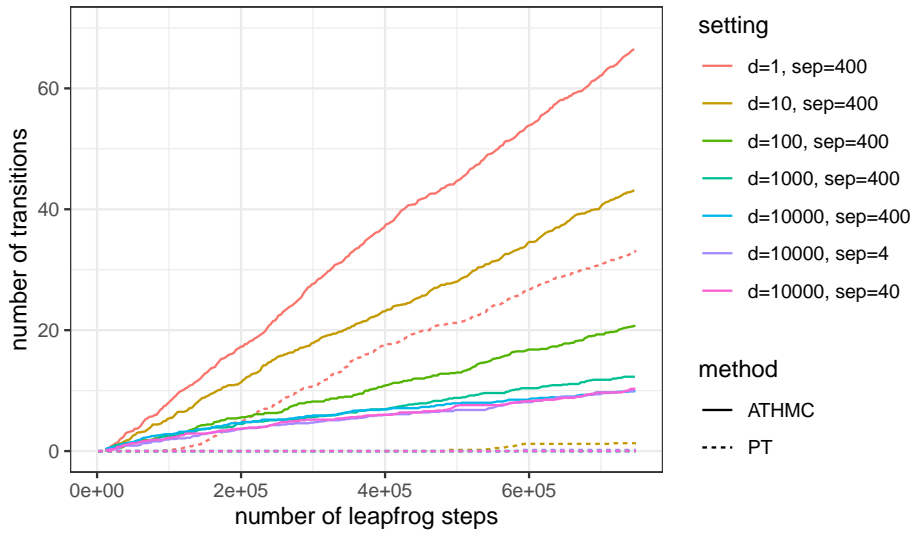


Figure 10: The cumulative number of transitions between the two modes for the bimodal target density (22) as a function of the cumulative number of leapfrog steps. ATHMC (solid line) and adaptive parallel tempering (dashed line) are compared under various settings for dimension d and mode separation $\|\mu_1 - \mu_2\|$.

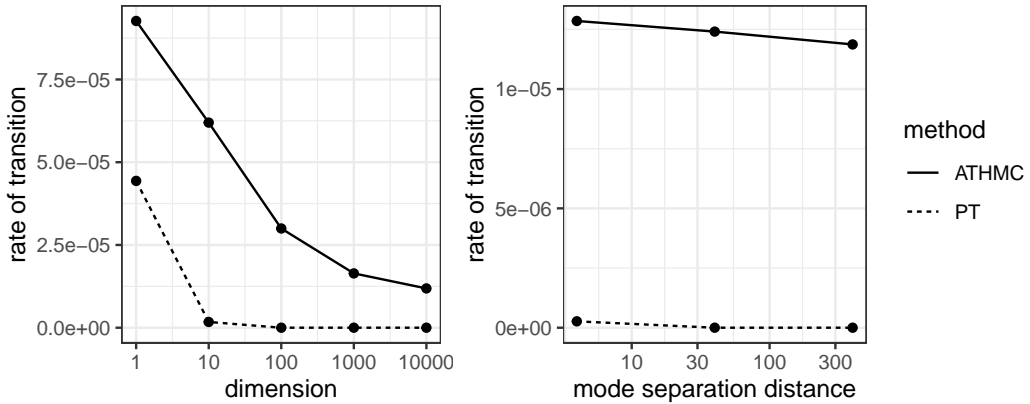


Figure 11: Left, the number of inter-mode transitions per leapfrog step for varying dimensions where the mode separation $\|\mu_2 - \mu_1\| = 400$ was fixed. Right, the rate of inter-mode transitions for varying mode separation distances where $d = 10000$ was fixed.

4.4 ATHMC within the Gibbs sampler

Our ATHMC has a particular advantage compared to other tempering based methods when used within the Gibbs sampler. In the Gibbs sampler, a component X_1 of the variable $X = (X_1, X_{-1})$ is updated by drawing a sample from the conditional distribution $\pi_{X_1|X_{-1}}$. If this conditional distribution is multimodal, a tempering technique may need to be employed within each Gibbs iteration.

However, if parallel tempering or the equi-energy sampler was used, all of the tempered distributions targeted by the parallel chains would change as X_{-1} varied. Hence, lengthy runs for the parallel chains would be required for each Gibbs iteration to ensure that those chains converge to their respective tempered distributions. Additionally, the temperature levels $1 = \alpha_1 < \alpha_2 < \dots < \alpha_K$ for the parallel chains may need to be adjusted depending on the value of X_{-1} by employing an adaptive method like that proposed by [Miasojedow et al. \(2013\)](#).

Simulated tempering involves random transitions across temperature levels $1 = \alpha_1 < \alpha_2 < \dots < \alpha_K$, aiming to obtain the next draw from a different mode with high probability. In the Gibbs sampler setting, the mixture weights $\{w_k; k \in 1:K\}$ for the tempered conditional densities $\pi_{k, X_1|X_{-1}} \propto (\pi_{X_1|X_{-1}})^{1/\alpha_k}$ need to be continually adjusted as X_{-1} changes over the iterations using an adaptive method such as the Wang-Landau algorithm ([Wang and Landau, 2001](#); [Atchadé and Liu, 2010](#)). Moreover, in order to obtain a new state on a different mode with reasonably high probability, a high temperature level should have been visited before returning to the lowest temperature level. However, taking a draw conditional on having completed a round trip from the lowest to the highest temperature level disrupts the invariance of the target distribution. Hence, the next draw should be the N -th return visit to the lowest temperature level, where N does not depend on the history of the visited temperature levels. Tuning for N , as well as $\{w_k\}$, over the Gibbs iterations may be challenging in practice.

Our ATHMC facilitates the acquisition of a draw from the multimodal conditional density $\pi_{X_1|X_{-1}}$ on a different mode by employing an automatically tuned tempering (i.e., mass scaling) schedule. The automatic tuning is carried out by simulating several paths in each Gibbs iteration. This approach contrasts with the adaptive parallel tempering or simulated tempering methods, which often require a considerable number of iterations for successful parameter adjustments. Figure 10 illustrated the lag where transitions between modes occurred only after a certain adaptation period when parallel tempering was used. In contrast, ATHMC enabled inter-mode transitions without the adaptation lag, demonstrating its usefulness within the Gibbs sampler.

4.5 Challenges in sampling from high-dimensional mixtures of components having different scales

In this section, we briefly discuss a fundamental challenge MCMC methods face when the isolated modes have different width scales in a high dimensional space. Figure 12 shows the log-density of a target distribution comprising two normal mixture components having different scales,

$$\bar{\pi}(x) = \frac{1}{2}\phi(x; -200, 4^2) + \frac{1}{2}\phi(x; 200, 1^2). \quad (30)$$

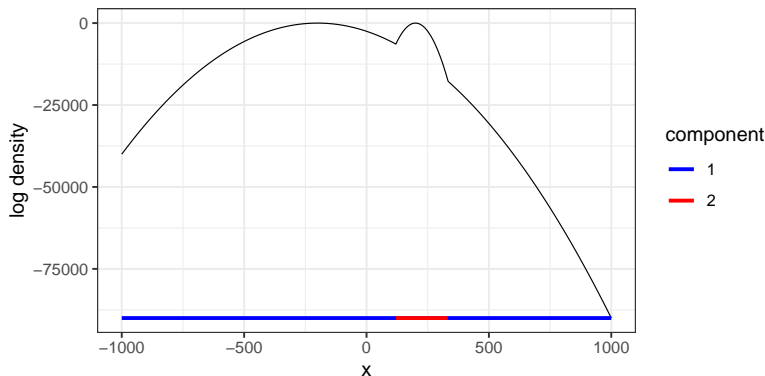


Figure 12: The logarithm of the density function (30) comprising two normal mixture components with different standard deviations. The region where the mixture component with the larger standard deviation has relatively higher conditional probability is marked in blue at the bottom. In this blue region, the gradient of the log target density is almost entirely determined by the target density function of the mixture component having the relatively larger standard deviation.

The region where the first mixture component has relatively higher conditional probability given the point is marked in blue at the bottom, and the region where the second component has higher conditional probability in red. In the blue region, the shape of the log density function is determined almost exclusively by the density of the first component. Consider a high-dimensional target density having mixture components of different scales. The region where the mixture component having the smaller scale has relatively higher conditional probability (i.e., the red region) has an exponentially small relative volume as the dimension d grows. Outside that small volume, the gradient of the potential function $U(x)$ is mostly determined by the density of the component having the larger scale. Thus, on the vast majority of the target space, the simulated Hamiltonian path is barely impacted by the density component having the relatively smaller scale. If a Hamiltonian path was constructed with time-varying mass starting from the blue region, the probability that it reached the red region would be exponentially small in d . Therefore, the proposed candidate would almost never be found in the red region, which might occupy a substantial probability in the target distribution. Since ATHMC constructs a reversible Markov chain (if we ignore the issue of dependently tuned parameters), the rate of jumps from the blue region to the red region is equal to the rate of jumps from the red region to the blue region. Hence, the probability of a jump from the red region to the blue region would be almost zero as well. Since a simulated path starting from the red region would end in the blue region with high probability, the low jump rate would be realized by an exponentially small acceptance probability, or a large net increase in Hamiltonian.

The fundamental challenge of sampling from high-dimensional, multimodal target distributions comprising isolated modes having different scales is faced by all other tempering based methods, including parallel tempering and simulated tempering (Woodard et al., 2009a,b; Bhatnagar and Randall, 2016). This is due to the fact that a mode having relatively small scale occupies exponentially small probability (in d) with respect to the tempered distribution $\pi^\beta(x)$ where the inverse temperature β is much smaller than 1. Since the mode having the smaller scale is almost never visited at high temperature levels, it remains unvisited as

the temperature cools down. Neal (1996, Section 5) discusses this issue in a greater detail. Tawn et al. (2020) propose a technique for stabilizing the mixture weights at varied tempered distributions by incorporating the Hessian of the log target density. However, this method requires knowing the mode locations in advance.

5 Applications

5.1 Self-localization of a sensor network

We apply ATHMC (Algorithm 3) to a sensor network self-localization problem, which was considered by Ihler et al. (2005). Noisy pairwise distance measurements data are available, and the goal is to localize the positions of eight sensors (labelled 1 through 8) in a two dimensional square $[0, 1]^2$. Additionally, there are three sensors (labelled 9, 10, and 11) at known locations, which resolve the unidentifiability issue with respect to translation, rotation, and reflection. However, we consider a situation where these three sensors are positioned approximately collinearly, so that the locations of the other eight sensors are identifiable only up to the reflection about the line connecting the three sensors. The true locations of all eleven sensors are marked on the plots in Figure 13, where the reflection symmetry is indicated by a red dashed line. Not all pairwise distances are measured, and the probability that two sensors t and u located at $\mathbf{x}_t = (x_t, y_t)$ and $\mathbf{x}_u = (x_u, y_u)$ have a distance measurement is given by $e^{-\|\mathbf{x}_t - \mathbf{x}_u\|^2 / (2R^2)}$, where $R = 0.3$. If the distance between the sensors t and u is measured, the noisy measurement follows the distribution $\mathcal{N}(\|\mathbf{x}_t - \mathbf{x}_u\|, \sigma_e^2)$ where $\sigma_e = 0.02$. We generated distance measurements data under this model.

For Bayesian inference, we assume independent uniform prior distributions on the square $[0, 1]^2$ for the locations of sensors labelled 1-8. Denoting by $d_{t,u}$ the distance measurements between sensors t and u and by $\iota_{t,u} \in \{0, 1\}$ the binary variable indicating whether the distance is measured, $1 \leq t \leq 8$ and $t < u \leq 11$, the posterior density for $\mathbf{x}_{1:8}$ given the measurement data is given by

$$\begin{aligned} \pi(\mathbf{x}_{1:8} | \{(\iota_{t,u}, d_{t,u}); 1 \leq t \leq 8, t < u \leq 11\}) \\ \propto \prod_{\substack{1 \leq t \leq 8, \\ t < u \leq 11}} \left[(e^{-\|\mathbf{x}_t - \mathbf{x}_u\|^2 / 2R^2})^{\iota_{t,u}} (1 - e^{-\|\mathbf{x}_t - \mathbf{x}_u\|^2 / 2R^2})^{1 - \iota_{t,u}} \right] \\ \cdot \prod_{\substack{1 \leq t \leq 8, \\ t < u \leq 11, \\ \iota_{t,u} = 1}} \frac{1}{2\pi\sigma_e^2} e^{-(\|\mathbf{x}_t - \mathbf{x}_u\| - d_{t,u})^2 / 2\sigma_e^2} \cdot \prod_{t=1}^8 \mathbf{1}[\mathbf{x}_t \in [0, 1]^2]. \quad (31) \end{aligned}$$

Due to the reflection symmetry about the line connecting the three sensors of known locations ($\mathbf{x}_{9:11}$), the posterior distribution of the unknown sensor locations is bimodal.

Automatically tuned HMC (Algorithm 3) and standard HMC were used to construct twelve chains each for the target posterior density (31). The simulated path rebounded whenever any of the sensors reached the boundary of the square (see the supplementary section S5 for the construction of this rebound step ensuring the reversibility of the constructed chains). Each chain constructed by ATHMC started at an approximate location of one of the posterior modes found by running standard HMC for ten iterations, in order to

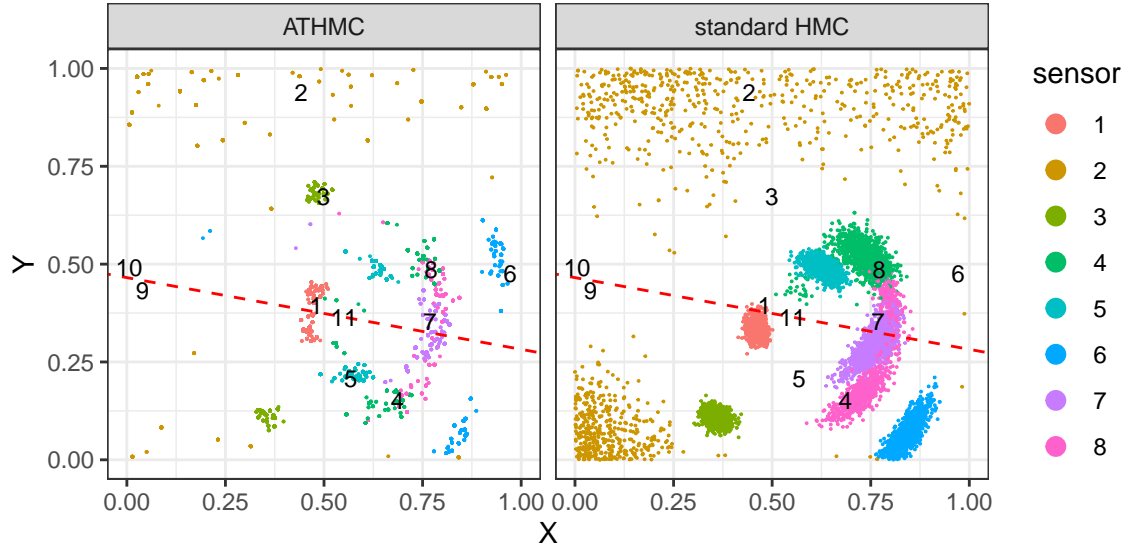


Figure 13: The sample points for the eight sensor locations in chains constructed by ATHMC and standard HMC for the sensor self-localization example with the posterior density given by (31). The true location of each sensor is marked by its number ID. A line approximately connecting the three sensors of known locations (9, 10, 11) is marked by a red dashed line. The true posterior density should be bimodal, where marginally for each sensor the locations corresponding to the two modes should be approximately symmetric with respect to the red dashed line. The parameters $R = 0.3$ and $\sigma_e = 0.02$ were assumed to be known.

facilitate proper automatic tuning in early iterations. ATHMC used a piecewise linear $\{\eta_k\}$ sequence (24) and a rectangular search scope described by (29) with the center point $(\frac{1}{2}, \frac{1}{2})$ and half-width $\frac{1}{6}$ in both x and y coordinates for every sensor.

Figure 13 shows the sampled sensor locations in different colors for one of the twelve chains constructed by each method. The true sensor locations are marked by their number IDs. The sample points obtained by ATHMC exhibit both modes of the posterior density, as can be clearly seen for the marginal draws for sensor #3 (dark green) and sensor #6 (light blue). In contrast, all sample points obtained by standard HMC are in one of the two posterior modes. The estimated locations are different than the true locations. Figures S-2 and S-3 in the supplementary section S5 show that all twelve chains constructed by ATHMC show both posterior modes and that all twelve chains constructed by standard HMC show only one of the two modes. We note that sensor #2 has no distance measurements with any other sensors, so its marginal posterior draws are scattered where there are no sensors nearby.

Figure 14 shows the traceplots of the potential function U and the y -coordinates of the third and the sixth sensors. Both of the chains constructed by ATHMC and standard HMC have similar levels of U , implying that the chains stay near one of the two posterior modes. However, the y -coordinates for sensor #3 and #6 show that the chain constructed by ATHMC frequently jumps between two posterior modes, whereas that constructed by standard HMC does not. Figure 15 shows the tuned values for the parameters $\hat{\gamma}$, η_* , $\bar{\epsilon}$, and K . All tuning parameters exhibit a stationary sequence, indicating that tuning was stable and consistent. The estimated $\hat{\gamma}$ values were around 2.2, in accordance with the fact that the log of the

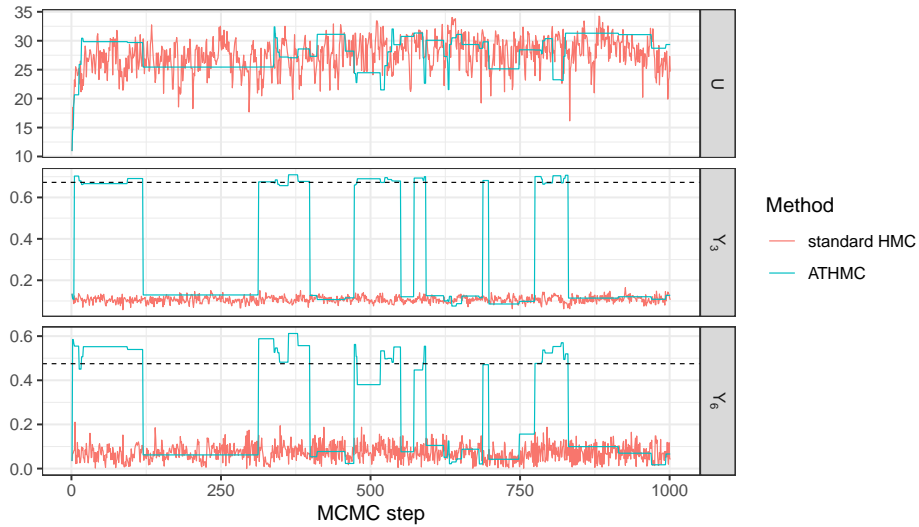


Figure 14: The traceplots of the potential energy $U(\mathbf{x}_{1:8}) = -\log \pi(\mathbf{x}_{1:8})$ and the y -coordinates of the third and the sixth sensors for one of the twelve chains constructed by ATHMC and standard HMC. The parameters $R = 0.3$ and $\sigma_e = 0.02$ were assumed to be known. The true y -coordinates for the third and the sixth sensors are indicated by horizontal dashed lines.

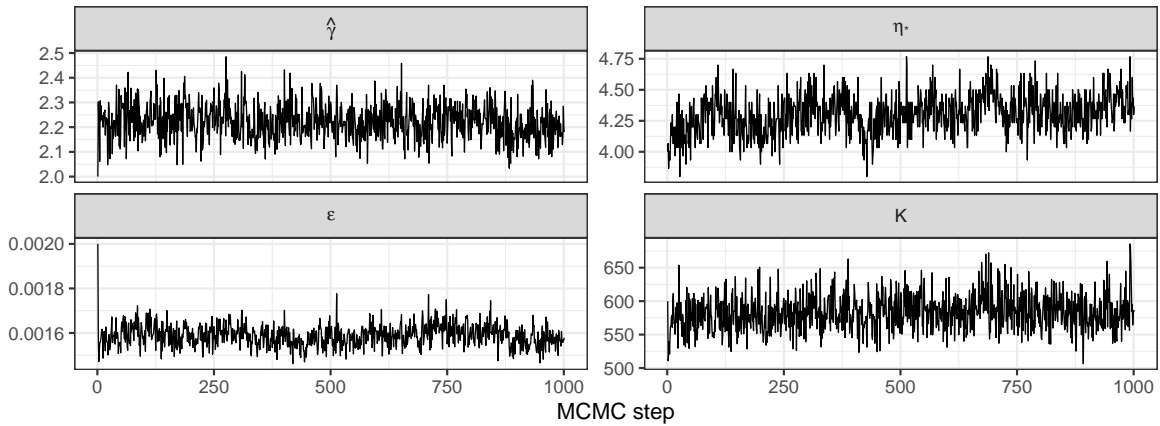


Figure 15: The traceplots for the tuning parameters $\hat{\gamma}$, η_* , $\bar{\epsilon}$, and K for the chains constructed by ATHMC. The plots show the average over twelve constructed chains. The parameters $R = 0.3$ and $\sigma_e = 0.02$ were assumed to be known.

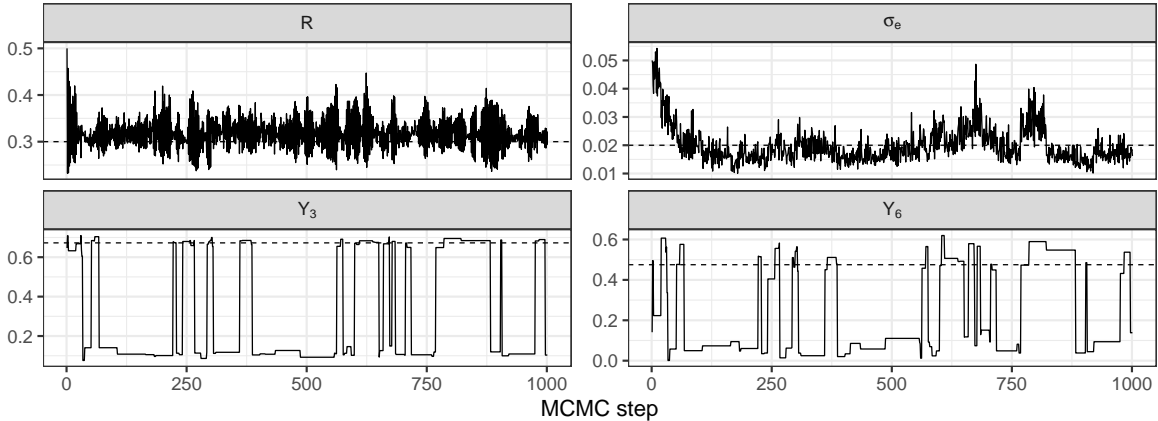


Figure 16: The traceplots for R , σ_e , and the y -coordinates of the third and the sixth sensors for a chain constructed by ATHMC within Gibbs. The values of R and σ_e were considered unknown. The true value for each variable is indicated by a dashed horizontal line.

posterior density (31) was quadratic in $\mathbf{x}_{1:8}$.

5.2 Self-localization of a sensor network for unknown R^2 and σ_e^2

We estimated R and σ_e jointly with the unknown sensor locations in order to demonstrate the use of automatically tuned tempered Hamiltonian Monte Carlo within the Gibbs sampler. For each iteration of the Gibbs sampler, the sensor locations $\mathbf{x}_{1:8}$ were updated by running one iteration of ATHMC targeting $\bar{\pi}(\mathbf{x}_{1:8}|R, \sigma_e)$, and then R and σ_e were updated using standard HMC, targeting $\bar{\pi}(R|\mathbf{x}_{1:8}, \sigma_e)$ and $\bar{\pi}(\sigma_e|\mathbf{x}_{1:8}, R)$, respectively. The density $\bar{\pi}(\mathbf{x}_{1:8}|R, \sigma_e)$ targeted by ATHMC changed over the iterations of the Gibbs sampler. In this situation, parallel tempering and simulated tempering face challenges for implementation, as explained in Section 1.

We constructed twelve independent chains targeting the joint posterior distribution for \mathbf{x} , R , and σ_e using ATHMC within the Gibbs sampler. The prior distributions for R and σ_e were given by the exponential distributions with rates $1/0.5$ and $1/0.05$, respectively. Figure 16 shows the traceplots of Y_3 , Y_6 , R , and σ_e for one of the twelve constructed chains. The sample draws for Y_3 and Y_6 show that both posterior modes were visited frequently. The sample draws for R and σ_e were close to the values we used to generate the data. Figure 17 shows the values of the tuning parameters $\hat{\gamma}$, η_* , $\bar{\epsilon}$, and K , averaged over the twelve constructed chains. All of the tuning parameters were stationary over the Gibbs iterations.

6 Other recent approaches to sampling from multimodal distributions

In this section, we briefly review some of the recent approaches to sampling from multimodal distributions. Continuous tempering is a strategy originally developed for, akin to various other tempering methods, simulating molecular dynamics where the free energy function has multiple isolated modes (Gobbo and Leimkuhler, 2015; Lerner and Mathias, 2016). It

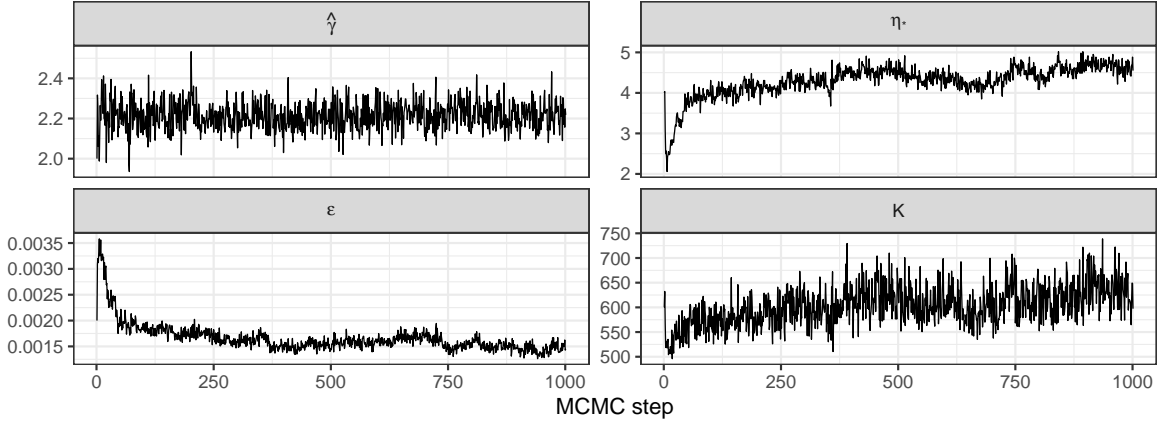


Figure 17: The traceplots for the tuning parameters $\hat{\gamma}$, η_* , $\bar{\epsilon}$, and K for the chains constructed by ATHMC targeting the joint posterior for $\mathbf{x}_{1:8}$, R , and σ_e . The plots show the average over twelve constructed chains.

extends the Hamiltonian system by including a variable $x_T \in \mathbb{R}$ linked to the temperature level and the associated velocity variable v_T . The extended Hamiltonian can be written in the form of

$$\hat{H}(x, v, x_T, v_T) = H(x, v) - f(x_T)G(x, v) + w(x_T) + \frac{1}{2}m_T v_T^2$$

where f , G and w are some functions and $m_T \in \mathbb{R}$ represents the mass associated with the added variable x_T . The link function f is chosen such that $f(x_T) = 0$ for a certain interval, say for $x_T \in (-c_T, c_T)$. The states in the constructed Markov chain for which $x_T \in (-c_T, c_T)$ may then be considered as draws from the original target density $\Pi(x, v) \propto e^{-H(x, v)}$. [Graham and Storkey \(2017\)](#) considered the case

$$f(x_T) = 1 - \beta(x_T), \quad G(x, v) = U(x) + \log g(x)$$

where $\beta(x_T)$ represents the inverse temperature and $g(x)$ is the normalized density function of a certain base distribution. In this case, the extended Hamiltonian defines a smooth transition between the target density $e^{-U(x)}$ and $g(x)$ such that the distribution of X given $\beta(x_T) = \beta^*$ has density

$$p(x|\beta(x_T) = \beta^*) \propto e^{-U(x)\beta^*} g(x)^{1-\beta^*}.$$

This density function has the same form as the bridging density commonly used by annealed importance sampling ([Neal, 2001](#)). Like simulated tempering, the continuous tempering strategy becomes efficient when the temperature variable is marginally evenly distributed across its range. If the marginal distribution is highly concentrated on low temperature values, mode hopping between isolated modes may occur with extremely low probability. On the contrary, if the distribution is concentrated on high temperature values, the samples from the original target distribution may be obtained rarely. In order to achieve an even distribution of temperature, techniques such as adaptive biasing force have been used ([Darve and Pohorille, 2001](#)). [Luo et al. \(2018\)](#) considered continuously tempered Hamiltonian Monte Carlo using the adaptive biasing force. They further developed the method for the case where

mini-batches are used, by introducing Nose-Hoover thermostats (Nosé, 1984; Hoover, 1985). The adaptive biasing technique, however, uses the history of the Markov chain and therefore experiences the same issue of slow adaptation, which can be problematic in Gibbs sampling.

Darting Monte Carlo uses independence Metropolis-Hastings proposals to facilitate jumps between isolated density components (Andricioaei et al., 2001; Sminchisescu and Welling, 2011). The modes of the target density are often found by a deterministic gradient ascent method started at different initial conditions to discover as many local maxima as possible. A mixture of density components centered at the discovered modes is often used by the independence Metropolis-Hastings (MH) sampler as a proposal distribution. The proposal distribution in this independence MH sampler can be adaptively tuned at regeneration times (Ahn et al., 2013). Darting Monte Carlo methods can be efficient for finding the relative probability masses of the discovered density components, but one of its drawbacks is that an external procedure for finding the modes and approximating the shapes of the modes needs to be employed. Another issue is the unfavorable scaling properties with increasing dimensions, as noted by Ahn et al. (2013).

Wormhole Hamiltonian Monte Carlo (Lan et al., 2014) connects the known locations of the modes by modifying the metric so that the modes are close to each other under the modified metric. The method then runs Riemannian manifold Hamiltonian Monte Carlo, which takes into account the given metric while simulating the Hamiltonian paths (Girolami and Calderhead, 2011).

Tak et al. (2018) developed a novel strategy that attempts a MH move that favors *low* target probability density points before attempting another MH move that favors high density points. In their algorithm, the proposal is first repelled from the the current state and then attracted by a local mode, which may be a different mode than that it started from. The authors, however, could only develop their method for symmetric proposal kernels, such as zero-mean random walk perturbations. Due to the use of random walk kernels, the scaling rate with respect to the space dimension is not likely to be more favorable than methods based on HMC. Moreover, the random walk variance greatly affects the probability of transitions from one mode to another, but the tuning may not be straightforward in practice.

There are interesting recent developments in sampling techniques that offer alternatives to the MCMC framework. For instance, Qiu and Wang (2023) developed a method for sampling from multimodal distributions by applying a series of invertible maps constructed by neural networks to draws from a simple base distribution (Hoffman et al., 2019; Kingma et al., 2016). These invertible maps bridge a sequence of intermediate tempered distributions, trained in a way that approximates the Wasserstein gradient flow. One potential drawback of this method is that the normalizing constants of the tempered distributions need to be estimated by importance sampling, which often does not scale to high dimensions. In general, the construction of a manageable pullback distribution for a complex target distribution can complement MCMC sampling, and vice versa.

7 Discussion

We developed a Markov chain Monte Carlo method that enables sampling from high-dimensional, multimodal distributions by simulating Hamiltonian dynamics with time-varying mass. The mass scaling along the trajectory is equivalent to tempering, as demonstrated by (9). Our

tempered Hamiltonian Monte Carlo can be conceptualized as a tempered transitions approach pioneered by Neal (1996) (refer to Section S2 in the supplementary text for further elucidation). We have developed an automatic tuning algorithm for our method by examining certain stability properties of the Hamiltonian dynamics with time-varying mass, as outlined in (12). ATHMC requires minimal customization, requiring only the specification of the search scope for isolated modes. The efficacy of our automatically-tuned, tempered Hamiltonian Monte Carlo (ATHMC) was demonstrated through its applications to mixtures of high-dimensional, log-polynomial distributions and a sensor network self-localization problem.

The computational complexity of standard HMC scales with the space dimension as $O(d^{5/4})$ (Beskos et al., 2013). Our automatic tuning strategy for tempered HMC does not explicitly depend on the dimension, instead only considering approximate stationarity of the scaled velocity $\bar{v}(\bar{t})$. Numerical results demonstrated that this tuning strategy was successful for high dimensional ($d = 10000$) bimodal distributions. For a bimodal, log-polynomial density, we empirically found that the rate of transitions between modes decreased approximately as $O(d^{-0.22})$, although we do not exactly know if the computational complexity of our tempered HMC scales at the same polynomial rate as standard HMC.

Our method does not require prior knowledge of the mode locations. It uses the gradient of the log target density to guide the search path toward isolated modes. However, if this local gradient information is not useful for finding certain modes, for instance when some local basins of the potential energy occupy relatively small volumes in a high-dimensional target space, then our method may fail to explore all modes properly. Strategies that utilize known mode locations and shapes, such as those proposed by Tawn et al. (2020) and Andrieu et al. (2011), may work synergistically with our method.

Some target distributions possess widely varying geometric properties across different regions of the space, as often encountered in posteriors for hierarchical Bayesian models. In such cases, our mass scaling strategy may be complemented by Riemannian manifold Hamiltonian Monte Carlo proposed by Betancourt and Girolami (2015), which employs a position-dependent mass matrix. The detailed exploration and development of this combined approach are deferred to future study.

Acknowledgements: The author thanks Dr. Yves Atchadé for his comments on an earlier draft of this manuscript.

References

- Ahn, S., Chen, Y. and Welling, M. (2013) Distributed and adaptive darting Monte Carlo through regenerations. In *Artificial Intelligence and Statistics*, 108–116. PMLR.
- Andricioaei, I., Straub, J. E. and Voter, A. F. (2001) Smart darting Monte Carlo. *The Journal of Chemical Physics*, **114**, 6994–7000.
- Andrieu, C., Jasra, A., Doucet, A. and Moral, P. D. (2011) On nonlinear Markov chain Monte Carlo. *Bernoulli*, **17**, 987 – 1014. URL: <https://doi.org/10.3150/10-BEJ307>.
- Andrieu, C. and Thoms, J. (2008) A tutorial on adaptive MCMC. *Statistics and Computing*, **18**, 343–373.

- Atchadé, Y. F. and Liu, J. S. (2010) The Wang-Landau algorithm in general state spaces: applications and convergence analysis. *Statistica Sinica*, 209–233.
- Atchadé, Y. F., Roberts, G. O. and Rosenthal, J. S. (2011) Towards optimal scaling of Metropolis-coupled Markov chain Monte Carlo. *Statistics and Computing*, **21**, 555–568.
- Beskos, A., Pillai, N., Roberts, G., Sanz-Serna, J.-M. and Stuart, A. (2013) Optimal tuning of the hybrid Monte Carlo algorithm. *Bernoulli*, **19**, 1501–1534.
- Betancourt, M. and Girolami, M. (2015) Hamiltonian Monte Carlo for hierarchical models. *Current trends in Bayesian methodology with applications*, **79**, 2–4.
- Bhatnagar, N. and Randall, D. (2016) Simulated tempering and swapping on mean-field models. *Journal of Statistical Physics*, **164**, 495–530.
- Bouchard-Côté, A., Vollmer, S. J. and Doucet, A. (2018) The bouncy particle sampler: A nonreversible rejection-free Markov chain Monte Carlo method. *Journal of the American Statistical Association*, **113**, 855–867.
- Brooks, B. R., Brooks III, C. L., Mackerell Jr., A. D., Nilsson, L., Petrella, R. J., Roux, B., Won, Y., Archontis, G., Bartels, C., Boresch, S., Caffisch, A., Caves, L., Cui, Q., Dinner, A. R., Feig, M., Fischer, S., Gao, J., Hodoscek, M., Im, W., Kuczera, K., Lazaridis, T., Ma, J., Ovchinnikov, V., Paci, E., Pastor, R. W., Post, C. B., Pu, J. Z., Schaefer, M., Tidor, B., Venable, R. M., Woodcock, H. L., Wu, X., Yang, W., York, D. M. and Karplus, M. (2009) CHARMM: The biomolecular simulation program. *Journal of Computational Chemistry*, **30**, 1545–1614. URL: <https://onlinelibrary.wiley.com/doi/abs/10.1002/jcc.21287>.
- Campos, C. M. and Sanz-Serna, J. (2015) Extra chance generalized hybrid Monte Carlo. *Journal of Computational Physics*, **281**, 365–374.
- Darve, E. and Pohorille, A. (2001) Calculating free energies using average force. *The Journal of chemical physics*, **115**, 9169–9183.
- Duane, S., Kennedy, A. D., Pendleton, B. J. and Roweth, D. (1987) Hybrid Monte Carlo. *Physics letters B*, **195**, 216–222.
- Gelman, A., Carlin, J. B., Stern, H. S., Dunson, D. B., Vehtari, A. and Rubin, D. B. (2013) *Bayesian data analysis*. CRC press, 3 edn.
- Geyer, C. J. (1991) Markov chain Monte Carlo maximum likelihood. *Interface Foundation of North America*. Retrieved from the University of Minnesota Digital Conservancy.
- Girolami, M. and Calderhead, B. (2011) Riemann manifold langevin and hamiltonian Monte Carlo methods. *Journal of the Royal Statistical Society: Series B (Statistical Methodology)*, **73**, 123–214.
- Gobbo, G. and Leimkuhler, B. J. (2015) Extended Hamiltonian approach to continuous tempering. *Physical Review E*, **91**, 061301.

- Graham, M. and Storkey, A. (2017) Continuously tempered Hamiltonian Monte Carlo. In *Proceedings of the Thirty-Third Conference on Uncertainty in Artificial Intelligence* (eds. G. Elidan, K. Kersting and A. T. Ihler). AUAI Press.
- Hoffman, M., Sountsov, P., Dillon, J. V., Langmore, I., Tran, D. and Vasudevan, S. (2019) Neutralizing bad geometry in hamiltonian Monte Carlo using neural transport. *arXiv preprint arXiv:1903.03704*.
- Hoover, W. G. (1985) Canonical dynamics: Equilibrium phase-space distributions. *Physical review A*, **31**, 1695.
- Ihler, A. T., Fisher, J. W., Moses, R. L. and Willsky, A. S. (2005) Nonparametric belief propagation for self-localization of sensor networks. *IEEE Journal on Selected Areas in Communications*, **23**, 809–819.
- Kingma, D. P., Salimans, T., Jozefowicz, R., Chen, X., Sutskever, I. and Welling, M. (2016) Improved variational inference with inverse autoregressive flow. *Advances in neural information processing systems*, **29**.
- Kone, A. and Kofke, D. A. (2005) Selection of temperature intervals for parallel-tempering simulations. *The Journal of chemical physics*, **122**.
- Kou, S., Zhou, Q., Wong, W. H. et al. (2006) Equi-energy sampler with applications in statistical inference and statistical mechanics. *The Annals of Statistics*, **34**, 1581–1619.
- Lan, S., Streets, J. and Shahbaba, B. (2014) Wormhole Hamiltonian Monte carlo. In *Proceedings of the AAAI Conference on Artificial Intelligence*, vol. 28.
- Landau, D. and Binder, K. (2021) *A guide to Monte Carlo simulations in statistical physics*. Cambridge university press.
- Leimkuhler, B. and Reich, S. (2004) *Simulating Hamiltonian dynamics*, vol. 14. Cambridge university press.
- Lenner, N. and Mathias, G. (2016) Continuous tempering molecular dynamics: A deterministic approach to simulated tempering. *Journal of chemical theory and computation*, **12**, 486–498.
- Luo, R., Wang, J., Yang, Y., Jun, W. and Zhu, Z. (2018) Thermostat-assisted continuously-tempered Hamiltonian Monte Carlo for Bayesian learning. In *Advances in Neural Information Processing Systems*, 10673–10682.
- Mangoubi, O., Pillai, N. S. and Smith, A. (2018) Does Hamiltonian Monte Carlo mix faster than a random walk on multimodal densities? *arXiv preprint arXiv:1808.03230*.
- Marinari, E. and Parisi, G. (1992) Simulated tempering: a new Monte Carlo scheme. *EPL (Europhysics Letters)*, **19**, 451.
- Miasojedow, B., Moulines, E. and Vihola, M. (2013) An adaptive parallel tempering algorithm. *Journal of Computational and Graphical Statistics*, **22**, 649–664.

- Mira, A. (2001) On metropolis-hastings algorithms with delayed rejection. *Metron*, **59**, 231–241.
- Neal, R. M. (1996) Sampling from multimodal distributions using tempered transitions. *Statistics and computing*, **6**, 353–366.
- (2001) Annealed importance sampling. *Statistics and Computing*, **11**, 125–139.
- (2011) MCMC using Hamiltonian dynamics. In *Handbook of Markov chain Monte Carlo* (eds. S. Brooks, A. Gelman, G. Jones and X.-L. Meng), 113–162. CRC press.
- (2012) *Bayesian learning for neural networks*, vol. 118. Springer Science & Business Media.
- Nosé, S. (1984) A unified formulation of the constant temperature molecular dynamics methods. *The Journal of chemical physics*, **81**, 511–519.
- Park, J. and Atchadé, Y. F. (2020) Markov chain Monte Carlo algorithms with sequential proposals. *Statistics and Computing*.
- Pompe, E., Holmes, C. and Łatuszyński, K. (2020) A framework for adaptive MCMC targeting multimodal distributions. *The Annals of Statistics*, **48**, 2930–2952.
- Qiu, Y. and Wang, X. (2023) Efficient multimodal sampling via tempered distribution flow. *Journal of the American Statistical Association*, **0**, 1–15. URL: <https://doi.org/10.1080/01621459.2023.2198059>.
- Roberts, G. O., Gelman, A. and Gilks, W. R. (1997) Weak convergence and optimal scaling of random walk Metropolis algorithms. *The Annals of Applied Probability*, **7**, 110–120.
- Roberts, G. O. and Rosenthal, J. S. (1998) Optimal scaling of discrete approximations to Langevin diffusions. *Journal of the Royal Statistical Society: Series B (Statistical Methodology)*, **60**, 255–268.
- (2007) Coupling and ergodicity of adaptive Markov chain Monte Carlo algorithms. *Journal of Applied Probability*, **44**, 458–475.
- Sminchisescu, C. and Welling, M. (2011) Generalized darting Monte Carlo. *Pattern Recognition*, **44**, 2738–2748.
- Swendsen, R. H. and Wang, J.-S. (1986) Replica Monte Carlo simulation of spin-glasses. *Physical review letters*, **57**, 2607–2609.
- Syed, S., Bouchard-Côté, A., Deligiannidis, G. and Doucet, A. (2022) Non-reversible parallel tempering: a scalable highly parallel MCMC scheme. *Journal of the Royal Statistical Society Series B: Statistical Methodology*, **84**, 321–350.
- Tak, H., Meng, X.-L. and van Dyk, D. A. (2018) A repelling–attracting Metropolis algorithm for multimodality. *Journal of Computational and Graphical Statistics*, **27**, 479–490.
- Tawn, N. G., Roberts, G. O. and Rosenthal, J. S. (2020) Weight-preserving simulated tempering. *Statistics and Computing*, **30**, 27–41.

- Vanetti, P., Bouchard-Côté, A., Deligiannidis, G. and Doucet, A. (2017) Piecewise deterministic Markov chain Monte Carlo. *arXiv preprint arXiv:1707.05296*.
- Wang, F. and Landau, D. P. (2001) Efficient, multiple-range random walk algorithm to calculate the density of states. *Physical review letters*, **86**, 2050–2053.
- Woodard, D., Schmidler, S. and Huber, M. (2009a) Sufficient Conditions for Torpid Mixing of Parallel and Simulated Tempering. *Electronic Journal of Probability*, **14**, 780 – 804. URL: <https://doi.org/10.1214/EJP.v14-638>.
- Woodard, D. B., Schmidler, S. C. and Huber, M. (2009b) Conditions for rapid mixing of parallel and simulated tempering on multimodal distributions. *The Annals of Applied Probability*, **19**, 617 – 640. URL: <https://doi.org/10.1214/08-AAP555>.

Supporting materials for *Sampling from high-dimensional,
multimodal distributions using automatically-tuned,
tempered Hamiltonian Monte Carlo*

Joonha Park
Department of Mathematics
University of Kansas
Lawrence, KS 66045, USA
email: j.park@ku.edu

Supplementary Content

S1 Proofs	S-1
S2 Connection between the tempered transitions method by Neal [1996] and our tempered Hamiltonian Monte Carlo	S-3
S3 Auxiliary strategy when the support is disconnected	S-5
S4 Relationship between tempered HMC (Algorithm 1) and the velocity scaling method by Neal [2011, Section 5.5.7]	S-7
S5 Additional figures for Section 5	S-9
S6 Mass-enhanced HMC with sequential proposals	S-11
S6.1 Examples: mixtures of multivariate normal distributions	S-13
S6.2 Tuning of parameters	S-17
S6.2.1 Mass–time scale equivariance and the choice of leapfrog step size	S-17
S6.2.2 The choice of α , L , N	S-18
S6.3 Theoretical explanations of when mass-enhanced HMC does and does not work	S-22
S6.3.1 The case where mass-enhanced HMC works	S-22
S6.3.2 The case where mass-enhanced HMC does not work	S-23
S7 Tempered Hamiltonian Monte Carlo with sequential proposals	S-24

S1 Proofs

Lemma S1. *The map $\check{\mathcal{S}}_1^K$ given by (18) satisfies an extension of the reversibility condition (4), namely*

$$\check{\mathcal{T}} \circ \check{\mathcal{S}}_1^K \circ \check{\mathcal{T}} \circ \check{\mathcal{S}}_1^K(x, 0, \check{v}) = (x, 0, \check{v}), \quad \forall x, \check{v},$$

where

$$\check{\mathcal{T}}(x, k, \check{v}) := (x, K - k, -\check{v}), \quad \forall x, k, \check{v}.$$

Proof. We first show that

$$\check{\mathcal{T}} \circ \check{\mathcal{S}}_1 \circ \check{\mathcal{T}} \circ \check{\mathcal{S}}_1(x, k, \check{v}) = (x, k, \check{v}), \quad \forall x, k, \check{v}.$$

Writing $\check{\mathcal{S}}_1(x\{k\}, k, \check{v}\{k\}) = (x\{k+1\}, k+1, \check{v}\{k+1\})$, we have

$$\check{\mathcal{T}} \circ \check{\mathcal{S}}_1(x\{k\}, k, \check{v}\{k\}) = (x\{k+1\}, K - k - 1, -\check{v}\{k+1\}).$$

Note that $\check{\mathcal{S}}_1(x\{k+1\}, K - k - 1, -\check{v}\{k+1\})$ is obtained by carrying out one leapfrog step from the initial position $x\{k+1\}$ and initial velocity $-\check{v}\{k+1\}$ with mass $\alpha_{K-k-1+\frac{1}{2}}M$ and time step $\check{\epsilon} = \alpha_{K-k-1+\frac{1}{2}}^a \epsilon$. Due to the symmetry of $\{\alpha_k\}$, we have $\alpha_{K-k-\frac{1}{2}} = \alpha_{k+\frac{1}{2}}$. The forward map $\check{\mathcal{S}}_1(x\{k\}, k, \check{v}\{k\}) = (x\{k+1\}, k+1, \check{v}\{k+1\})$ is exactly reversed, leading to

$$\begin{aligned} \check{\mathcal{S}}_1(x\{k+1\}, K - k - 1, -\check{v}\{k+1\}) &:= (x, K - k, -\check{v}), \quad \text{where} \\ -\check{v}\{k + \frac{1}{2}\} &= -\check{v}\{k+1\} - \frac{\check{\epsilon}}{2} \{\alpha_{k+\frac{1}{2}}M\}^{-1} \nabla U(x\{k+1\}) \\ x\{k\} &= x\{k+1\} + \check{\epsilon}(-\check{v}\{k + \frac{1}{2}\}) \\ -\check{v}\{k\} &= -\check{v}\{k + \frac{1}{2}\} - \frac{\check{\epsilon}}{2} \{\alpha_{k+\frac{1}{2}}M\}^{-1} \nabla U(x\{k\}). \end{aligned}$$

Thus we have $\check{\mathcal{S}}_1 \circ \check{\mathcal{T}} \circ \check{\mathcal{S}}_1(x\{k\}, k, \check{v}\{k\}) = (x\{k\}, K - k, -\check{v}\{k\}) = \check{\mathcal{T}}(x\{k\}, k, \check{v}\{k\})$. Since $\check{\mathcal{T}}$ is self-inverse, this shows that $\check{\mathcal{T}} \circ \check{\mathcal{S}}_1 \circ \check{\mathcal{T}} \circ \check{\mathcal{S}}_1$ is the identity map. We then proceed by induction, which easily follows since

$$\check{\mathcal{T}} \circ \check{\mathcal{S}}_1^k \circ \check{\mathcal{T}} \circ \check{\mathcal{S}}_1^k = \check{\mathcal{T}} \circ \check{\mathcal{S}}_1^{k-1} \circ (\check{\mathcal{S}}_1 \circ \check{\mathcal{T}} \circ \check{\mathcal{S}}_1) \circ \check{\mathcal{S}}_1^{k-1} = \check{\mathcal{T}} \circ \check{\mathcal{S}}_1^{k-1} \circ \check{\mathcal{T}} \circ \check{\mathcal{S}}_1^{k-1}.$$

Therefore, we have that $\check{\mathcal{T}} \circ \check{\mathcal{S}}_1^K \circ \check{\mathcal{T}} \circ \check{\mathcal{S}}_1^K$ is equal to the identity map. For our purpose, we only need the special case where the map is applied to $k = 0$. \square

Proof of Proposition 1.

Proof. Lemma S1 shows that Algorithm 1 belongs to the class of MCMC algorithms targeting the extended target distribution $\Pi(x, k, \check{v})$. Thus Proposition 2 in Park and Atchadé [2020] shows that $\{X^{(i)}\}$ is reversible with respect to $\bar{\pi}(x)$. \square

Proof of Proposition 2.

Proof. We have

$$\nabla U(x) = \nabla(x^\top Bx)^{\gamma/2} = \frac{\gamma}{2} \cdot (x^\top Bx)^{\frac{\gamma}{2}-1} \cdot 2Bx = \gamma \|x\|_B^{\gamma-2} Bx.$$

From (13), we see that $(\bar{x}, \bar{v}, \bar{t})$ satisfy the differential equations

$$\begin{aligned}
\frac{d\bar{x}}{d\bar{t}} &= \frac{dx}{dt} e^{-a\eta} - x \cdot a \frac{d\eta}{dt} e^{-a\eta} = \left(e^{2a\eta} \frac{dx}{dt} \right) \cdot e^{-a\eta} - \bar{x} \cdot a \frac{d\eta}{d\bar{t}} = \bar{v} - \bar{x} \cdot a \frac{d\eta}{d\bar{t}}, \\
\frac{d\bar{v}}{d\bar{t}} &= \frac{d\check{v}}{dt} \cdot e^{a\eta} + \check{v} \cdot a \frac{d\eta}{dt} e^{a\eta} \\
&= e^{2a\eta} \cdot \left\{ -(e^{2\eta} M)^{-1} \nabla U(x) \right\} \cdot e^{a\eta} + \bar{v} \cdot a \frac{d\eta}{d\bar{t}} \\
&= -e^{(3a-2)\eta} M^{-1} \gamma \|x\|_B^{\gamma-2} Bx + \bar{v} \cdot a \frac{d\eta}{d\bar{t}} \\
&= -e^{(3a-2)\eta} M^{-1} \gamma e^{(\gamma-1)a\eta} \|\bar{x}\|_B^{\gamma-2} B\bar{x} + \bar{v} \cdot a \frac{d\eta}{d\bar{t}} \\
&= -e^{\{a(\gamma+2)-2\}\eta} M^{-1} \nabla U(\bar{x}) + \bar{v} \cdot a \frac{d\eta}{d\bar{t}}.
\end{aligned}$$

□

Proof of Corollary 1.

Proof. From Proposition 2 we know that $(\bar{x}, \bar{v}, \bar{t})$ solves linear differential equations

$$\frac{d}{d\bar{t}} \begin{pmatrix} \bar{x} \\ \bar{v} \end{pmatrix} = \begin{pmatrix} -a(d\eta/d\bar{t})I & I \\ -2M^{-1}B & a(d\eta/d\bar{t})I \end{pmatrix} \begin{pmatrix} \bar{x} \\ \bar{v} \end{pmatrix}. \quad (\text{S1})$$

Since B is symmetric and positive definite, the matrix $M^{-1}B = M^{-1}B^{1/2}B^{1/2}$ has the same set of eigenvalues as $B^{1/2}M^{-1}B^{1/2}$, which is positive definite. Therefore all eigenvalues of $M^{-1}B$ are positive. Let $\lambda_1, \dots, \lambda_d$ be the eigenvalues of $M^{-1}B$, with associated eigenvectors u_1, \dots, u_d . It can be readily checked that the eigenvalues of the rate matrix in (S1) are given by $\pm\sqrt{-2\lambda_j + a^2(d\eta/d\bar{t})^2}$ with associated eigenvectors

$$\left(u_j^\top, \left\{ a(d\eta/d\bar{t}) \pm \sqrt{-2\lambda_j + a^2(d\eta/d\bar{t})^2} \right\} u_j^\top \right)^\top.$$

All of these eigenvalues are purely imaginary if $2\lambda_{\min}(M^{-1}B) > a^2(d\eta/d\bar{t})^2$. Therefore the solutions of (S1) are linear combinations of sinusoidal functions with frequencies $\sqrt{2\lambda_j - a^2(d\eta/d\bar{t})^2}$, $j = 1, \dots, d$. □

S2 Connection between the tempered transitions method by Neal [1996] and our tempered Hamiltonian Monte Carlo

The tempered transitions method by Neal [1996] applies a sequence of transition kernels having varied tempered distributions as stationary distributions, increasing the chance that the end state is on a different mode than the mode the initial state was in. The sequence of states are denoted by

$$\hat{x}_0 \xrightarrow{T_1} \hat{x}_1 \xrightarrow{T_2} \cdots \hat{x}_{n-1} \xrightarrow{T_n} \bar{x}_n \xrightarrow{\check{T}_n} \check{x}_{n-1} \xrightarrow{\check{T}_{n-1}} \cdots \check{x}_1 \xrightarrow{\check{T}_1} \check{x}_0,$$

where \hat{x}_0 is the initial state and \check{x}_0 is the final state, which becomes the proposed candidate for the next state of the Markov chain constructed by the method. The transition kernels $T_1, \dots, T_n, \check{T}_1, \dots, \check{T}_n$ satisfy the relationship

$$p_k(x_k)dx_k T_k(x_k, dx'_k) = p_k(x'_k)dx'_k \check{T}_k(x'_k, dx_k) \quad (\text{S2})$$

where $p_k(x_k)$ denotes the density of the k -th auxiliary distribution. The density of the target distribution that we want to sample from is denoted by $p_0(x)$. The auxiliary distributions often represent the distribution at various temperature levels. For example, we may employ $p_k(x) \propto p_0^{\beta_k}(x)$, where β_k denotes the i -th inverse temperature, facilitating global mixing for multimodal distributions. The acceptance probability for the proposed candidate \check{x}_0 is given by

$$\min \left[1, \frac{p_1(\hat{x}_0)}{p_0(\hat{x}_0)} \cdot \frac{p_2(\hat{x}_1)}{p_1(\hat{x}_1)} \cdot \dots \cdot \frac{p_n(\hat{x}_{n-1})}{p_{n-1}(\hat{x}_{n-1})} \cdot \frac{p_{n-1}(\check{x}_{n-1})}{p_n(\check{x}_{n-1})} \cdot \dots \cdot \frac{p_0(\check{x}_0)}{p_1(\check{x}_0)} \right]. \quad (\text{S3})$$

It can be shown that the density p_0 is invariant, for any choice of auxiliary densities $\{p_k; 1 \leq k \leq n\}$.

In practice, the kernels T_k and \check{T}_k are often constructed using the Metropolis-Hastings strategy. For example, a sequence of proposal kernels Q_k can be used to draw

$$\hat{x}_0 \xrightarrow{Q_1} \hat{x}_1 \xrightarrow{Q_2} \dots \hat{x}_{n-1} \xrightarrow{Q_n} \bar{x}_n \xrightarrow{Q_{n+1}} \check{x}_{n-1} \xrightarrow{Q_{n+2}} \dots \check{x}_1 \xrightarrow{Q_{2n}} \check{x}_0. \quad (\text{S4})$$

Accepting each state in the sequence using the Metropolis-Hastings ratios of the form

$$\frac{p_k(\hat{x}_k)d\hat{x}_k Q_k(\hat{x}_k, d\hat{x}_{k-1})}{p_k(\hat{x}_{k-1})d\hat{x}_{k-1} Q_{2n-k+1}(\hat{x}_{k-1}, \hat{x}_k)} \quad \text{or} \quad \frac{p_k(\check{x}_{k-1})d\check{x}_{k-1} Q_k(\check{x}_{k-1}, d\check{x}_k)}{p_k(\check{x}_k)d\check{x}_k Q_{2n-k+1}(\check{x}_k, d\check{x}_{k-1})} \quad (\text{S5})$$

lead to the construction of the transition kernels T_k and \check{T}_k satisfying (S2). Here we understand $\hat{x}_n = \check{x}_n = \bar{x}_n$. Instead of accepting or rejecting each state on the sequence, we can continue drawing $\hat{x}_1, \dots, \bar{x}_n, \dots, \check{x}_0$ using the proposal kernels Q_1, \dots, Q_{2n} and combine the ratios of the form (S5) with the acceptance ratio in (S3). The combined acceptance probability for the final state \check{x}_0 is given by

$$\min \left[1, \frac{p_0(\check{x}_0)d\check{x}_0 Q_1(\check{x}_0, d\hat{x}_1) \dots Q_n(\check{x}_{n-1}, d\bar{x}_n) Q_{n+1}(\bar{x}_n, d\hat{x}_{n-1}) \dots Q_{2n}(\hat{x}_1, d\hat{x}_0)}{p_0(\hat{x}_0)d\hat{x}_0 Q_1(\hat{x}_0, d\hat{x}_1) \dots Q_n(\hat{x}_{n-1}, d\bar{x}_n) Q_{n+1}(\bar{x}_n, d\check{x}_{n-1}) \dots Q_{2n}(\check{x}_1, d\check{x}_0)} \right].$$

Tempered Hamiltonian Monte Carlo (Algorithm 1) can be thought of as a variant of the tempered transitions method (S4) where the states \hat{x}_k or \check{x}_k are given by the pair (x_k, \check{v}_k) for $k = 0, 1, \dots, K = 2n$ and where the kernel $Q_k(x_{k-1}, \check{v}_{k-1}; dx_k d\check{v}_k)$ puts all its mass at point

$$\Psi_{\check{\epsilon}_{k-\frac{1}{2}}}^{\check{\epsilon}_{k-\frac{1}{2}}}(x_{k-1}, \check{v}_{k-1}; \alpha_{k-\frac{1}{2}} M, \check{\epsilon}_{k-\frac{1}{2}}),$$

which is obtained by carrying out one leapfrog step with step size $\check{\epsilon}_{k-\frac{1}{2}} = \alpha_{k-\frac{1}{2}}^{\frac{2}{7+2}}$ and mass $\alpha_{k-\frac{1}{2}} M$. The proposal kernels Q_1, \dots, Q_{2n} are symmetric in the sense that $Q_j = Q_{2n+1-j}$ for $j \in 1 : n$. The initial and final densities are given by

$$p_0(x_0, \check{v}_0) = e^{-U(x_0)} \det \left(\frac{\alpha_0 M}{2\pi} \right)^{1/2} e^{-\check{v}_0^\top (\alpha_0 M) \check{v}_0 / 2},$$

$$p_{2n}(x_{2n}, \check{v}_{2n}) = e^{-U(x_{2n})} \det \left(\frac{\alpha_{2n} M}{2\pi} \right)^{1/2} e^{-\check{v}_{2n}^\top (\alpha_{2n} M) \check{v}_{2n} / 2}.$$

In order to obtain the acceptance probability for the final pair, we view the sequence of transitions in the following way:

$$\begin{aligned}
(x_1, \check{v}_1) &= \Psi_{\check{\epsilon}_{\frac{1}{2}}} (x_0, \check{v}_0; \alpha_{\frac{1}{2}} M, \check{\epsilon}_{\frac{1}{2}}) \\
(x_2, \check{v}_2) &= \Psi_{\check{\epsilon}_{\frac{3}{2}}} (x_1, \check{v}_1; \alpha_{\frac{3}{2}} M, \check{\epsilon}_{\frac{3}{2}}) \\
&\dots \\
(x_n, \check{v}_n) &= \Psi_{\check{\epsilon}_{n-\frac{1}{2}}} (x_{n-1}, \check{v}_{n-1}; \alpha_{n-\frac{1}{2}} M, \check{\epsilon}_{n-\frac{1}{2}}) \\
(x_n, \check{v}'_n) &= \mathcal{T}(x_n, \check{v}_n) = (x_n, -\check{v}_n) \\
(x_{n+1}, \check{v}'_{n+1}) &= \Psi_{-\check{\epsilon}_{n+\frac{1}{2}}} (x_n, \check{v}'_n; \alpha_{n+\frac{1}{2}} M, \check{\epsilon}_{n+\frac{1}{2}}) \\
&\dots \\
(x_{2n}, \check{v}'_{2n}) &= \Psi_{-\check{\epsilon}_{2n-\frac{1}{2}}} (x_{2n-1}, \check{v}'_{2n-1}; \alpha_{2n-\frac{1}{2}} M, \check{\epsilon}_{2n-\frac{1}{2}})
\end{aligned}$$

Here \mathcal{T} is the velocity reflection operator. Since

$$(x_{n+1}, \check{v}'_{n+1}) = \Psi_{-\check{\epsilon}_{n+\frac{1}{2}}} (x_n, \check{v}'_n; \alpha_{n+\frac{1}{2}} M, \check{\epsilon}_{n+\frac{1}{2}}) = \mathcal{T} \circ \Psi_{\check{\epsilon}_{n+\frac{1}{2}}} (x_n, \check{v}_n; \alpha_{n+\frac{1}{2}} M, \check{\epsilon}_{n+\frac{1}{2}}) = (x_{n+1}, -\check{v}_{n+1})$$

and the same relation holds recursively for all subsequent transitions, we see that $\check{v}'_{n+m} = -\check{v}_{n+m}$ for $m \in 0 : n$. The reason that we view the sequence of transitions this way is the following symmetry:

$$\begin{aligned}
(x_{2n}, \check{v}'_{2n}) &= \Psi_{-\check{\epsilon}_{2n-\frac{1}{2}}} \circ \dots \circ \Psi_{-\check{\epsilon}_{n+\frac{1}{2}}} \circ \mathcal{T} \circ \Psi_{\check{\epsilon}_{n-\frac{1}{2}}} \circ \dots \circ \Psi_{\check{\epsilon}_{\frac{1}{2}}} (x_0, \check{v}_0) \\
(x_0, \check{v}_0) &= \Psi_{-\check{\epsilon}_{\frac{1}{2}}} \circ \dots \circ \Psi_{-\check{\epsilon}_{n-\frac{1}{2}}} \circ \mathcal{T} \circ \Psi_{\check{\epsilon}_{n+\frac{1}{2}}} \circ \dots \circ \Psi_{\check{\epsilon}_{2n-\frac{1}{2}}} (x_{2n}, \check{v}'_{2n})
\end{aligned}$$

The acceptance probability for $(x_{2n}, \check{v}'_{2n})$ is given by

$$\begin{aligned}
&\frac{p_{2n}(x_{2n}, \check{v}'_{2n}) dx_{2n} d\check{v}'_{2n} \delta_{\Psi_{\check{\epsilon}_{2n-\frac{1}{2}}}(x_{2n}, \check{v}'_{2n})}(dx_{2n-1} d\check{v}'_{2n-1}) \dots \delta_{\Psi_{-\check{\epsilon}_{\frac{1}{2}}}(x_1, \check{v}_1)}(dx_0 d\check{v}_0)}{p_0(x_0, \check{v}_0) dx_0 d\check{v}_0 \delta_{\Psi_{\check{\epsilon}_{\frac{1}{2}}}(x_0, \check{v}_0)}(dx_1 d\check{v}_1) \dots \delta_{\Psi_{-\check{\epsilon}_{2n-\frac{1}{2}}}(x_{2n-1}, \check{v}'_{2n-1})}(dx_{2n} d\check{v}'_{2n})} \\
&= \frac{p_{2n}(x_{2n}, \check{v}'_{2n})}{p_0(x_0, \check{v}_0)} \left| \frac{d(x_{2n}, \check{v}'_{2n})}{d(x_0, \check{v}_0)} \right| \dots \quad (\text{S6})
\end{aligned}$$

Since the leapfrog method preserves the volume element $dx d\check{v}$ and $\check{v}'_n = -\check{v}_n$, the Jacobian determinant in the right hand side of (S6) is equal to unity.

S3 Auxiliary strategy when the support is disconnected

In this section, we propose an auxiliary strategy for applying tempered HMC when the support of the target distribution is separated. If the support of the target density $\text{supp}(\pi) := \{x \in \mathbf{X}; \pi(x) > 0\}$ has disconnected components, the Hamiltonian path started from one density component cannot reach other disconnected components, since the potential energy $U(x) = -\log \pi(x)$ is infinite on $\text{supp}(\pi)^c = \{x; \pi(x) = 0\}$. We consider addition of a small mixture component to the unnormalized target density,

$$\pi^+(x) = \pi(x) + \nu g(x).$$

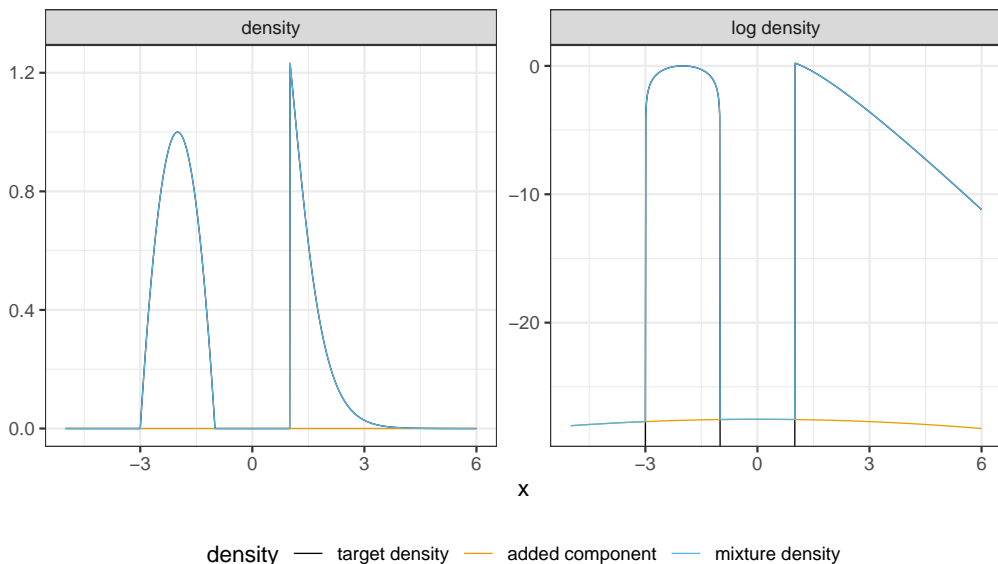


Figure S-1: An illustrative diagram showing the effect of adding a small mixture component. The target density $\pi(x)$ and the mixture density $\pi^+(x)$ are visually indistinguishable on the natural (non-log) scale, because the weight of the added mixture component $\nu = e^{-25}$ is tiny. However, $\log\{\pi^+(x)\}$ is lower bounded by $\log\{\nu g(x)\}$, so finite everywhere.

Here $\pi(x) = Z\bar{\pi}(x)$ is an unnormalized target density function, ν a small positive constant, and $g(x)$ the probability density of the added mixture component. We assume that $g(x)$ can be evaluated pointwise. This mixture component is intended to bridge separated density components. Figure S-1 shows $\pi(x)$, $\nu g(x)$, and the sum $\pi^+(x)$ where

$$\begin{aligned} \text{supp}(\pi) &= (-3, -1) \cup (1, \infty), \\ \pi^+(x) &= \pi(x) + e^{-25}\phi(x; 0, 5^2). \end{aligned}$$

Since $\log \pi^+(x)$ is lower bounded by $\log(\nu g(x))$, tempered HMC (Algorithm 1) can enable jumps between the two separated components of $\text{supp}(\pi)$. Once a sample Markov chain has been constructed by Algorithm 1 targeting $\pi^+(x)$, draws from the original target density $\pi(x)$ can be obtained using rejection sampling. Provided that the states of the constructed Markov chain can be considered as draws from π^+ , rejection sampling accepts a state x with probability

$$\frac{\pi(x)}{\pi(x) + \nu g(x)}.$$

It can be readily checked that the accepted draws can be considered as samples from the original target density:

$$\frac{\pi(x) + \nu g(x)}{Z + \nu} \cdot \frac{\pi(x)}{\pi(x) + \nu g(x)} \propto \frac{\pi(x)}{Z}.$$

In order to reduce the number of draws lost by the rejection sampling, the mixture weight ν can be chosen such that $\nu g(x) \ll \pi(x)$ for typical posterior draws. Section 4 shows that Algorithm 1 can enable jumps across a potential energy barrier whose height Δ scales exponentially with the maximum increase in the mass scaling schedule $\eta(t)$. Thus for a typical

posterior draw x_1 from π and a point x_2 in $\text{supp}(\pi)^c$, we can choose ν such that the difference in the potential energy, which is approximately

$$\log \pi^+(x_1) - \log \pi^+(x_2) \approx \log \pi(x_1) - \log(\nu g(x_2)),$$

is on the order of $e^{\gamma a \{\max \eta(t) - \min \eta(t)\}}$ (see (23)). Therefore, the mixture weight ν can be chosen exponentially small. For such tiny ν , it is likely that all of the MCMC draws from $\pi^+(x)$ survive the rejection sampling.

The mixture density $g(x)$ should be chosen such that the graph of $\log g(x)$ is more flat than that of $\log \pi(x)$, so that the disconnected components of $\text{supp}(\pi)$ are bridged by $g(x)$. However, if it is excessively flat, the constructed Hamiltonian paths may unnecessarily reach far beyond the region where most of the probability mass of $\pi(x)$ is placed. A reasonable choice in practice may be to let $g(x)$ be the density of a normal distribution that covers most of the region where the support of $\pi(x)$ is expected to be located.

S4 Relationship between tempered HMC (Algorithm 1) and the velocity scaling method by Neal [2011, Section 5.5.7]

In this section, we elaborate on the relationship between our tempered HMC algorithm (Algorithm 1) and the method of *tempering during a trajectory* proposed by Neal [2011, Section 5.5.7]. Neal [2011]’s idea is to scale the velocity by a certain factor before and after each leapfrog step. This approach is a discretization of dynamics described by Equation (15).

Our Algorithm 1 numerically simulates dynamics (13) with leapfrog step sizes $\check{\epsilon} = e^{2a\eta\bar{\epsilon}}$ where $\bar{\epsilon}$ is a fixed, baseline leapfrog step size. The optimal value for a is $\frac{2}{\gamma+2}$, where γ is the polynomial degree of the local growth of $U(x)$. This numerical simulation is essentially equivalent to the numerical simulation of (15) with leapfrog step sizes $\epsilon = e^{(2a-1)\eta\bar{\epsilon}} = e^{-\eta\check{\epsilon}}$, as we will see below. Note that (15) is defined on t scale, so the leapfrog step size is denoted by ϵ . Neal [2011]’s velocity scaling method employs constant leapfrog step size, which corresponds to a fixed choice $a = \frac{1}{2}$, which is not optimal if $\gamma \neq 2$. The equivalence between the tempered HMC algorithm (Algorithm 1) and Neal [2011]’s velocity scaling method can be explicitly confirmed as follows. The mass-scaling method simulates dynamics on \check{t} scale, and the velocity scaling method simulates dynamics on t scale, where the two time scales are related via $d\check{t} = e^\eta dt$. Since $v = \frac{dx}{dt}$ and $\check{v} = \frac{dx}{d\check{t}}$, we have $\check{v} = e^{-\eta}v$. Let the velocity and the position variable at the end of the k -th leapfrog step be denoted by $v\{k\}$ and $x\{k\}$. The leapfrog step for the mass-scaling method is given by

$$\begin{aligned} \check{v}\{k + \frac{1}{2}\} &= \check{v}\{k\} - \left(e^{2\eta_{k+\frac{1}{2}}} M \right)^{-1} \frac{\partial U}{\partial x}(x\{k\}) \cdot e^{2a\eta_{k+\frac{1}{2}}} \frac{\bar{\epsilon}}{2} \\ &= \check{v}\{k\} - e^{2(a-1)\eta_{k+\frac{1}{2}}} M^{-1} \frac{\partial U}{\partial x}(x\{k\}) \frac{\bar{\epsilon}}{2}, \\ x\{k + 1\} &= x\{k\} + e^{2a\eta_{k+\frac{1}{2}}} \check{v}\{k + \frac{1}{2}\} \bar{\epsilon}, \\ \check{v}\{k + 1\} &= \check{v}\{k + \frac{1}{2}\} - e^{2(a-1)\eta_{k+\frac{1}{2}}} M^{-1} \frac{\partial U}{\partial x}(x\{k + 1\}) \frac{\bar{\epsilon}}{2}. \end{aligned}$$

Applying $v\{k\} = e^{\eta_k} \check{v}\{k\}$, we have

$$\begin{aligned}
v\{k + \frac{1}{2}\} &= e^{\eta_{k+\frac{1}{2}}} \left[e^{-\eta_k} v\{k\} - e^{2(a-1)\eta_{k+\frac{1}{2}}} M^{-1} \frac{\partial U}{\partial x}(x\{k\}) \frac{\bar{\epsilon}}{2} \right] \\
&= e^{\eta_{k+\frac{1}{2}} - \eta_k} v\{k\} - e^{(2a-1)\eta_{k+\frac{1}{2}}} M^{-1} \frac{\partial U}{\partial x}(x\{k\}) \frac{\bar{\epsilon}}{2}, \\
x\{k + 1\} &= x\{k\} + e^{2a\eta_{k+\frac{1}{2}}} e^{-\eta_{k+\frac{1}{2}}} v\{k + \frac{1}{2}\} \bar{\epsilon}, \\
v\{k + 1\} &= e^{\eta_{k+1}} \left[e^{-\eta_{k+\frac{1}{2}}} v\{k + \frac{1}{2}\} - e^{2(a-1)\eta_{k+\frac{1}{2}}} M^{-1} \frac{\partial U}{\partial x}(x\{k + 1\}) \frac{\bar{\epsilon}}{2} \right] \\
&= e^{\eta_{k+1} - \eta_{k+\frac{1}{2}}} \left[v\{k + \frac{1}{2}\} - e^{(2a-1)\eta_{k+\frac{1}{2}}} M^{-1} \frac{\partial U}{\partial x}(x\{k + 1\}) \frac{\bar{\epsilon}}{2} \right].
\end{aligned}$$

Let

$$\begin{aligned}
v\{k-\} &= v\{k\} \cdot e^{-(\eta_k - \eta_{k-\frac{1}{2}})}, \\
v\{k+\} &= v\{k\} \cdot e^{\eta_{k+\frac{1}{2}} - \eta_k}.
\end{aligned}$$

The velocity $v\{k-\}$ represents the velocity right after the k -th leapfrog step, but before multiplying $e^{\eta_k - \eta_{k-\frac{1}{2}}}$ to obtain $v\{k\}$. The velocity $v\{k+\}$ represents the velocity obtained after multiplying $e^{\eta_{k+\frac{1}{2}} - \eta_k}$ to $v\{k\}$ but before carrying out the $k + 1$ -st leapfrog step. Then the above equations can be written as

$$\begin{aligned}
v\{k + \frac{1}{2}\} &= v\{k+\} - e^{(2a-1)\eta_{k+\frac{1}{2}}} M^{-1} \frac{\partial U}{\partial x}(x\{k\}) \frac{\bar{\epsilon}}{2}, \\
x\{k + 1\} &= x\{k\} + e^{(2a-1)\eta_{k+\frac{1}{2}}} v\{k + \frac{1}{2}\} \bar{\epsilon}, \\
v\{(k + 1)-\} &= v\{k + \frac{1}{2}\} - e^{(2a-1)\eta_{k+\frac{1}{2}}} M^{-1} \frac{\partial U}{\partial x}(x\{k + 1\}) \frac{\bar{\epsilon}}{2},
\end{aligned}$$

and

$$v\{(k + 1)+\} = v\{(k + 1)-\} \cdot e^{\eta_{k+\frac{3}{2}} - \eta_{k+\frac{1}{2}}}.$$

The initial velocity is given by $v\{0\} \sim N(0, M^{-1})$, and the first leapfrog step starts with $v\{0+\} = v\{0\} \cdot e^{\frac{\eta_1}{2}}$. The last leapfrog step ends with $v\{K-\}$, and the final velocity used for checking acceptance of the proposal is obtained by $v\{K\} = v\{K-\} \cdot e^{\eta_K - \eta_{K-\frac{1}{2}}} = v\{K-\} \cdot e^{-\eta_{K-\frac{1}{2}}}$. For the piecewise linear η -sequence given by $\eta_k = \frac{2\eta_*}{K} \min\{k, K - k\}$, we have $\eta_{\frac{1}{2}} = \frac{\eta_*}{K}$ and

$$\eta_{k+\frac{1}{2}} - \eta_{k-\frac{1}{2}} = \begin{cases} \frac{2\eta_*}{K} & \text{if } k \leq \frac{K-1}{2} \\ 0 & \text{if } k = \frac{K}{2} \\ -\frac{2\eta_*}{K} & \text{if } k \geq \frac{K+1}{2} \end{cases}$$

When $\gamma = 2$, the optimal value for a is equal to $\frac{1}{2}$, coinciding with the implicit choice by Neal [2011]. If $a = \frac{1}{2}$ is used for other values of γ , then $\bar{v}(\bar{t}) = \check{v}(\check{t}) \cdot e^{a\eta}$ does not exhibit stationary oscillations, so our tuning algorithm applies poorly. The transition rate between isolated modes will likely be low if $a = \frac{1}{2}$ is used instead of its optimal value $\frac{2}{\gamma+2}$.

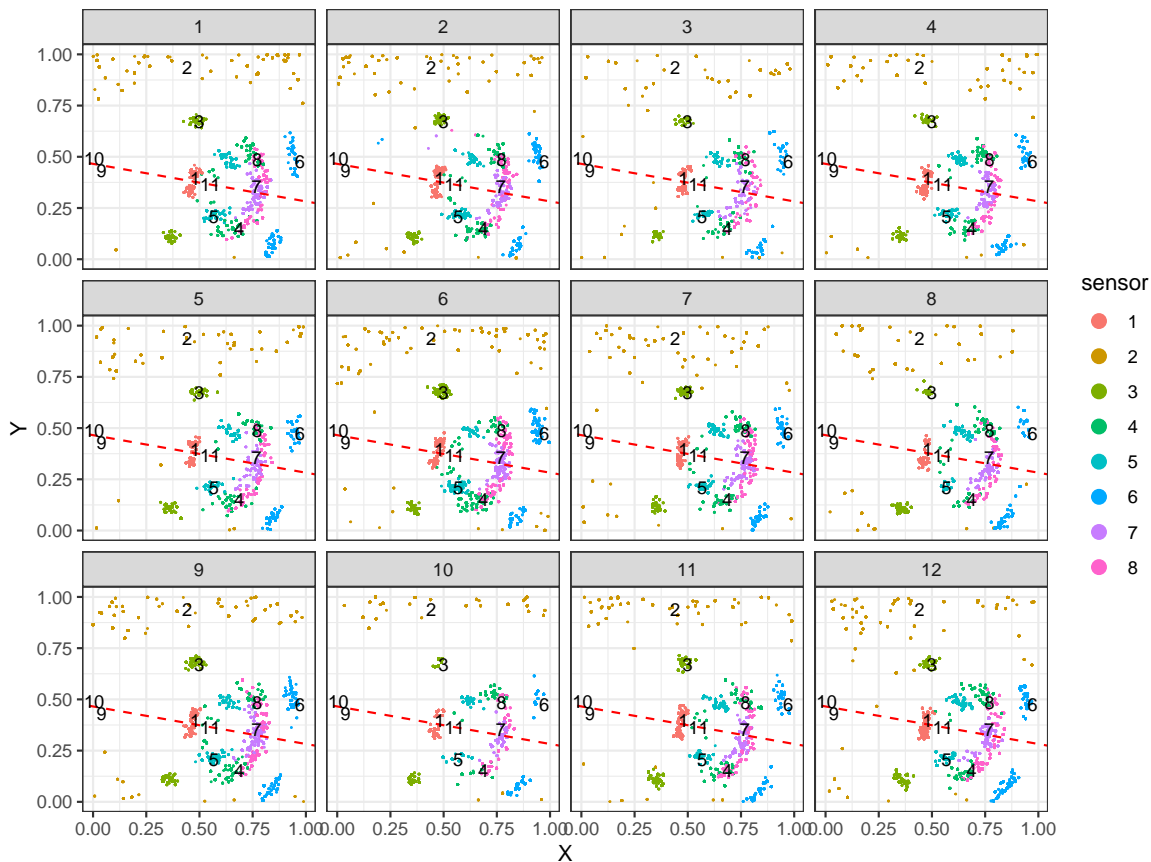


Figure S-2: The marginal sample points for the eight unknown sensor locations in twelve chains constructed by ATHMC for the sensor self-localization example with the posterior density given by (31). The true location of each sensor is marked by its number ID. A line approximately connecting the three sensors of known locations (9, 10, 11) is marked by a red dashed line. The true posterior density should be bimodal, where the marginal sensor locations for the two modes should be approximately symmetric with respect to the red dashed line. The parameters $R = 0.3$ and $\sigma_e = 0.02$ were assumed to be known.

S5 Additional figures for Section 5

In this supplementary section, we provide some additional details and figures for Section 5. In Section 5, we considered a sensor network self-localization problem where the locations of eight sensors with unknown positions are estimated by noisy, pairwise distances between the sensors.

In order to ensure that every sensor is located inside the unit square along the simulated path, we reflected the velocities of the sensors when they reached the boundary of the square. Specifically, if during each leapfrog step, the scalar velocity v_x or v_y for the sensor that went outside the square was negated. This rebound step was inserted in between the two divided half steps for $x\{k+1\} = x\{k\} + \check{\epsilon}_{k+\frac{1}{2}}\check{v}\{k+\frac{1}{2}\}$ in (18). The modified leapfrog update map (call it \mathcal{S}'_1) also satisfies time reversibility, that is, $\mathcal{T} \circ \mathcal{S}'_1 \circ \mathcal{T} \circ \mathcal{S}'_1$ is the identity map.

Figure S-2 shows the estimated positions for the eight sensors obtained by twelve chains in-

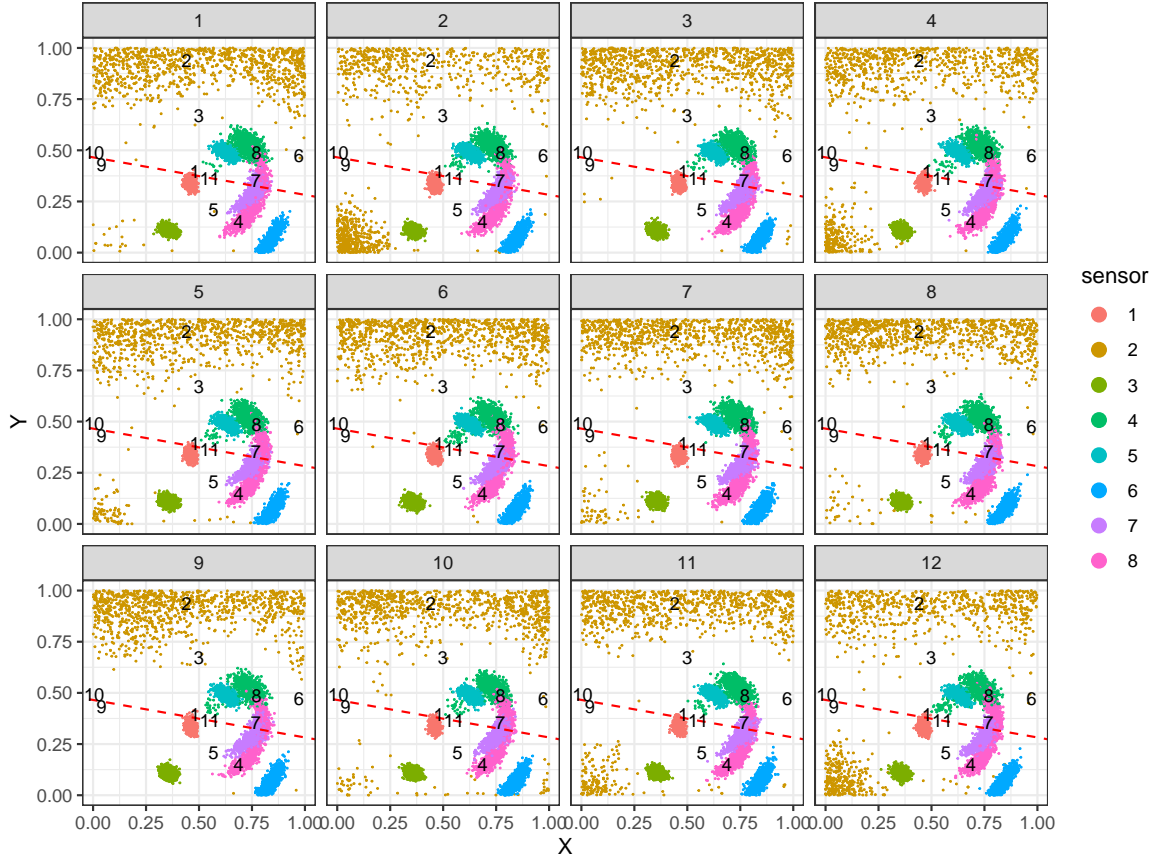


Figure S-3: The marginal sample points for the eight unknown sensor locations in twelve chains constructed by standard HMC for the sensor self-localization example with the posterior density given by (31). The parameters $R = 0.3$ and $\sigma_e = 0.02$ were assumed to be known. The true posterior density should be bimodal, but all twelve constructed chains dwelled in only one of the modes (compare with Figure S-2.)

independently constructed by running our automatically-tuned, tempered Hamiltonian Monte Carlo (ATHMC, Algorithm 3). The posterior distribution is strongly multimodal, and all twelve chains correctly visit both modes. To see this, note that there are two isolated point clouds for both sensor #3 (dark green) and for sensor #6 (blue), roughly symmetric about the dashed line passing through the three sensors of known locations. Figure S-3 shows the estimated positions for the same eight sensors obtained by twelve chains independently constructed by running standard Hamiltonian Monte Carlo. All twelve chains explored only a single mode, as can be noted by the fact that there is a single point cloud for each sensor #3 or #6. These results show that our ATHMC facilitates transitions between isolated modes, whereas standard HMC does not. The fact that the point clouds look relatively denser in Figure S-3 for chains constructed by standard HMC is because the acceptance probability was on average higher for chains constructed by standard HMC than those by ATHMC. The ATHMC method focuses on making global transitions between isolated modes, and thus the average acceptance probability is relatively low. However, local explorations within each mode can be readily carried out by complementing ATHMC by occasionally employing standard HMC kernels.

S6 Mass-enhanced HMC with sequential proposals

In Section 2.2 of the main text, we briefly discussed the idea of employing enhanced (but constant) mass for Hamiltonian Monte Carlo. In the current section, we delve into this approach, termed as mass-enhanced HMC (Algorithm S1). This method simulates the Hamiltonian dynamics for an enhanced mass $\check{M} = \alpha M$ where $\alpha > 1$ is constant. Here M denotes the inverse covariance matrix of the multivariate normal distribution for the initial velocity.

Mass-enhanced HMC (Algorithm S1) uses the sequential-proposal strategy proposed by Park and Atchadé [2020]. Under this strategy, a collection of candidates are sequentially considered for the next state of the Markov chain, where the acceptance of each candidate is decided using a shared Uniform(0,1) draw. In mass-enhanced HMC, the collection of candidates are obtained by simulating (11) for time increments of $\check{\epsilon}$. These candidates, denoted by $\check{\Psi}_{n\check{\epsilon}}(x(0), v(0))$, $1 \leq n \leq N$, are either accepted or rejected based on the criterion (7) where a common Uniform(0,1) draw Λ is used for *all* candidates. Park and Atchadé [2020] gives a proof of the fact that $\bar{\pi}(x)$ is invariant for the Markov chains constructed by using this sequential proposal strategy. The choice of the step size $\check{\epsilon}$ for numerical simulation will be discussed in Section S6.2.1.

The use of the sequential-proposal strategy is critical for mass-enhanced HMC, because, unlike standard HMC, the acceptance probability varies greatly along the path. Let $\check{K}(v) = \frac{1}{2}v^\top \check{M}v$ and $\check{H}(x, v) = U(x) + \check{K}(v)$. We have

$$\begin{aligned}
 H\{x(t), v(t)\} &= U(x(t)) + \alpha^{-1}\check{K}(v(t)) \\
 &= \alpha^{-1}\check{H}\{x(t), v(t)\} + (1 - \alpha^{-1})U(x(t)) \\
 &\approx \alpha^{-1}\check{H}\{x(0), v(0)\} + (1 - \alpha^{-1})U(x(t)) \\
 &= H\{x(0), v(0)\} + (1 - \alpha^{-1})\{U(x(t)) - U(x(0))\},
 \end{aligned}
 \tag{S7}$$

which implies that if $\alpha \gg 1$, the amount of change in Hamiltonian H is close to the change in the potential energy. Since the simulation with enhanced mass $\check{M} = \alpha M$ enables the

Algorithm S1: Mass-enhanced HMC using sequential proposals (toy algorithm)

Input : Potential energy function $U(x) = -\log \pi(x)$; Mass matrix, M ; Mass enhancement ratio, $\alpha > 1$; Leapfrog step size, $\check{\epsilon}$; Number of algorithm iterations, I ; Maximum number of proposals per iteration, N ; Number of acceptable states to be found per iteration, L

```

1 Initialize: Choose  $X^{(0)}$  arbitrarily
2 for  $i \leftarrow 0 : I-1$  do
3   Draw  $\Lambda \sim \text{Uniform}(0, 1)$ 
4   Draw  $W_0 \leftarrow \mathcal{N}(0, M^{-1})$  // initial velocity
5   Let  $Y_0 \leftarrow X^{(i)}$ 
6   Let  $X^{(i+1)} \leftarrow X^{(i)}$  // the case where fewer than  $L$  acceptable states
   were found
7   Let  $n_{acc} \leftarrow 0$  // the number of acceptable candidate states found
8   for  $n \leftarrow 1 : N$  do
9      $(Y_n, W_n) \leftarrow \check{\Psi}_{\check{\epsilon}}(Y_{n-1}, W_{n-1})$  obtained by numerically simulating (11) for time
      $\check{\epsilon}$  with mass  $\check{M} = \alpha M$  using the leapfrog method with step size  $\check{\epsilon}$ .
10    if  $\Lambda < \exp\{-H(Y_n, W_n) + H(Y_0, W_0)\}$  then
11      |  $n_{acc} \leftarrow n_{acc} + 1$ 
12    end
13    if  $n_{acc} = L$  then
14      | Let  $X^{(i+1)} \leftarrow Y_n$ 
15      | break
16    end
17  end
18 end
Output: A draw of Markov chain,  $(X^{(i)})_{i \in 1 : I}$ 

```

Hamiltonian path to reach high potential energy regions that are rarely visited under the stationary distribution $\bar{\pi}(x)$, there is large potential energy increase $U(x(t)) - U(x(0))$ along the path, and the acceptance probability for such $x(t)$ is exponentially small. We have from (7) and (S7) that the acceptance ratio for the proposed candidate $\check{\Psi}_t(x(0), v(0))$ can be approximated by

$$e^{-H\{x(t), v(t)\} + H\{x(0), v(0)\}} \approx e^{-(1-\alpha^{-1})\{U(x(t)) - U(x(0))\}} = \left\{ \frac{\pi(x(t))}{\pi(x(0))} \right\}^{1-\alpha^{-1}},$$

which can be extremely small if $\pi(x(t)) \ll \pi(x(0))$ and $\alpha \gg 1$. The sequential-proposal strategy allows for the simulation to be continued until a low potential energy state is visited and an acceptable candidate is found.

A sequence of proposed candidates $\{(Y_n, W_n); n \geq 1\}$ is obtained by the recursion $(Y_n, W_n) = \check{\Psi}_{\check{\epsilon}}(Y_{n-1}, W_{n-1})$, where $Y_0 = X^{(i)}$ and $W_0 \sim \mathcal{N}(0, M^{-1})$. A candidate (Y_n, W_n) is considered acceptable if

$$\Lambda < e^{-H(Y_n, W_n) + H(Y_0, W_0)}, \quad (\text{S8})$$

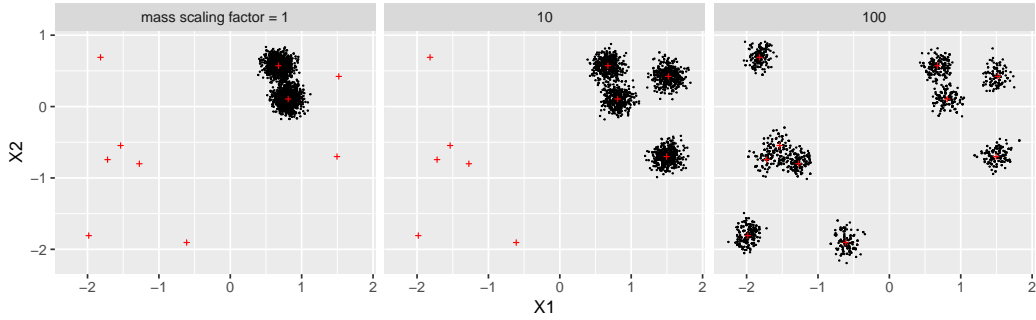


Figure S-4: Sample draws of Markov chains constructed by mass-enhanced HMC (Algorithm S1) with various mass scale factors ($\alpha = 1, 10,$ and 100) for the target distribution considered in Example S6.1. The centers of the ten Gaussian components are marked by red '+' signs.

where a random number $\Lambda \sim \text{Uniform}(0, 1)$ is drawn independently of all proposed candidates. The L -th acceptable proposal in the sequence $\{(Y_n, W_n); n \geq 0\}$ is taken as the next state of the Markov chain, where L can be any number greater than or equal to one. The number of candidates proposed in each iteration is capped at N in order to avoid indefinite simulation of the Hamiltonian path. If there are less than L acceptable proposals among the first N in a given iteration, the next state of the Markov chain stays at the current state: $X^{(i+1)} = X^{(i)}$. This method constructs Markov chains that leave the extended target density $\Pi(x, v)$ invariant [Park and Atchadé, 2020].

This algorithm (Algorithm S1) can be successful for low-dimensional multimodal target distributions (say $d \leq 5$) or for some special high-dimensional distributions such as a mixture of Gaussian distributions where all mixture components have the same covariance matrix Σ . However, in general, mass-enhanced HMC (Algorithm S1) is ineffective in high dimensions, due to the fact that the simulated paths with enhanced mass \tilde{M} may only rarely visit regions of low potential energy. For this reason, we developed our tempered Hamiltonian Monte Carlo algorithm (Algorithm 1) that gradually increases and then decreases the mass with which the Hamiltonian dynamics is simulated, so that at the end of the path the particle may settle down at a low potential energy region.

S6.1 Examples: mixtures of multivariate normal distributions

Here we demonstrate the performance of mass-enhanced HMC (Algorithm S1) for mixtures of normal distributions. Examples S6.1 and S6.2 show that the method can construct globally mixing Markov chains for mixtures of high-dimensional normal distributions in the special case where all mixture components have the same covariance that is equal to the mass matrix M . Example S6.3 show that in general, however, the method may fail if the mixture covariances are different.

We first note that if every mixture component has the same covariance given by Σ , then by choosing the mass matrix M equal to Σ^{-1} , one can effectively turn the target distribution into a mixture of normal components with a shared covariance I . To see this, consider a

transformation of variables

$$x' := \Sigma^{-1/2}x, \quad v' := \Sigma^{-1/2}v \quad (\text{S9})$$

where $\Sigma^{-1/2}$ is the inverse of the symmetric square-root matrix of Σ . This linear transformation make the target distribution a mixture of normal components with covariance I . These transformed variables (x', v') satisfy the Hamiltonian equation of motion with unit mass, as follows:

$$\begin{aligned} \frac{dx'}{dt} &= \Sigma^{-1/2} \frac{dx}{dt} = v', \\ \frac{dv'}{dt} &= \Sigma^{-1/2} \frac{dv}{dt} = -\Sigma^{-1/2} \cdot M^{-1} \frac{\partial U}{\partial x} = -\Sigma^{1/2} \frac{\partial U}{\partial x} = -\frac{\partial U}{\partial x'}. \end{aligned}$$

Thus for the case where all mixture components have the same covariance, we can without loss of generality assume that the common covariance is equal to I .

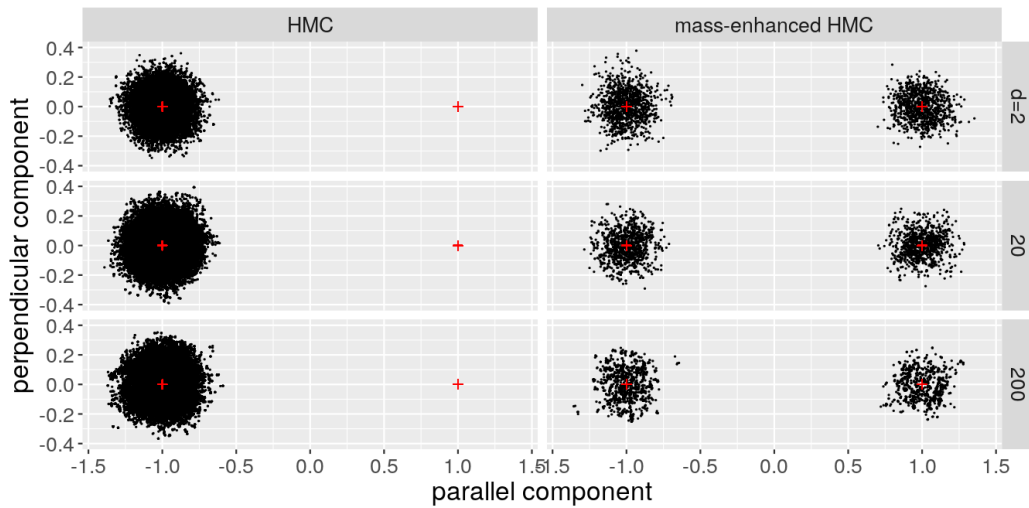
Example S6.1 Figure S-4 shows the sample draws for a two-dimensional mixture distribution of ten Gaussian components. The target density is given by

$$\pi(x) = \frac{1}{10} \sum_{j=1}^{10} \phi(x; \mu_j, \sigma^2 I), \quad x \in \mathbb{R}^2,$$

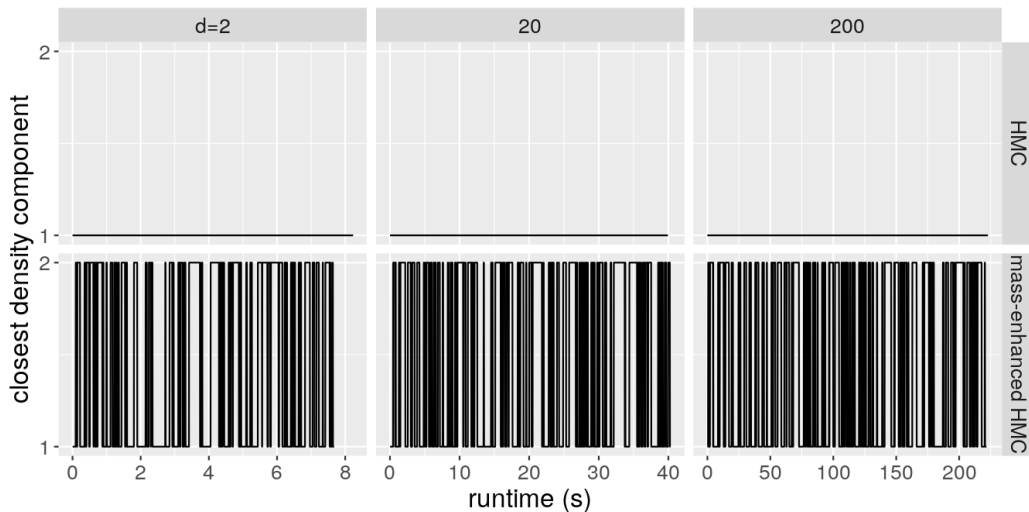
where the centers of the density components μ_j , $j \in 1:10$, are distributed randomly across the square $[-2, 2]^2$ as shown in Figure S-4. The standard deviation of each component σ was 0.1. We constructed Markov chains of length two thousand using Algorithm S1 with three different values of the mass scale factors, $\alpha = 1, 10$, and 100. The leapfrog step size varied linearly with the square root of the mass scale factor ($\epsilon = 0.1 \cdot \sqrt{\alpha}$). The first acceptable proposal was taken for the next state of the Markov chain (i.e., $L = 1$), and each iteration was terminated if no acceptable proposal was found among the first $N = 10$ proposals. The inverse covariance matrix for the velocity distribution was equal to the identity matrix ($M = I$). The numerical results shown in Figure S-4 show that using mass enhancement ratio $\alpha > 1$ can enable jumps between separated density components. When we run sequential-proposal HMC *without* mass enhancing (i.e., $\alpha = 1$), the Markov chain could reach only one density component nearest to the initial component. When $\alpha = 10$, the sample Markov chain reached more density components but not remotely separated ones. When $\alpha = 100$, the chain reached all components. \square

Example S6.2 Next we demonstrate how Algorithm S1 scales with increasing space dimension d . Since it is sufficient to demonstrate that the algorithm facilitates jumps from one density component to another, we set the target distribution to be a mixture of two Gaussian components where the distance between the center of the components and the standard deviation of both components are fixed:

$$\pi_d(x_d) = \frac{1}{2} \sum_{j=1}^2 \phi(x_d; \mu_{j,d}, \sigma^2 I_d), \quad x_d \in \mathbb{R}^d, \quad (\text{S10})$$



(a) Sample draws of the constructed Markov chains. The x -axis shows the projection onto the direction from one density mode to the other (i.e., $\mu_{2,d} - \mu_{1,d}$), and the y -axis shows the projection onto a randomly selected direction perpendicular to $\mu_{2,d} - \mu_{1,d}$. The experimental settings are the same as those in Figure S-5b.



(b) The closest density component (1 or 2) for each state of the constructed Markov chains. The number of algorithm iterations (I) was two thousand for mass-enhanced HMC, and HMC was run for approximately the same amount of time. The leapfrog step size of 0.1 was used for both HMC and mass-enhanced HMC. For mass-enhanced HMC, the number of acceptable candidates searched for in each iteration was $L = 1$; maximum number of proposed candidates per iteration was $N = 1000$; mass enhancement ratio was $\alpha = 100$.

Figure S-5: Markov chains constructed by HMC and mass-enhanced HMC (Algorithm S1) where the target density is given by (S10) ($d = 2, 20, 200$).

where $\|\mu_{1,d} - \mu_{2,d}\| = 2$, $\sigma \equiv 0.1$ for $d = 2, 20$, and 200 . The directions of $\mu_{1,d} - \mu_{2,d}$ were randomly generated from spherically uniform distributions. We ran both a standard HMC and mass-enhanced HMC (Algorithm S1) for these target distributions. For mass-enhanced HMC, the mass enhancement ratio was $\alpha = 100$, the number of acceptable proposals found in each iteration was $L = 1$, and the maximum number of proposals in each iteration was $N = 1000$. The mass-enhanced HMC method was run for $I = 2000$ iterations, and the standard HMC method was run for roughly the same amount of time. Each proposal in mass-enhanced HMC was obtained by extending the numerical simulation by one leapfrog step. The proposals in HMC were obtained by making five leapfrog jump steps with a randomly drawn initial velocity. The leapfrog step size of 0.1 was used.

Figure S-5b shows the closest density component (1 or 2) for each state of the Markov chains constructed by both methods. Whereas the Markov chains constructed by standard HMC failed to jump from one density component to the other, the Markov chains constructed by mass-enhanced HMC made frequent jumps between the density components. Figure S-5a shows the states in the constructed Markov chains, projected to the direction connecting the two density modes (i.e., $\mu_{2,d} - \mu_{1,d}$) and to a randomly selected direction connecting the two density modes (i.e., $\mu_{2,d} - \mu_{1,d}$) and to a randomly selected direction perpendicular to $\mu_{2,d} - \mu_{1,d}$. Standard HMC drew samples from only one density component, but mass-enhanced HMC was able to sample from both density components. Considering that the second density component has most of its mass on an exponentially small part of the d dimensional target space, we think mass-enhanced HMC shows a remarkable efficiency in finding in a remote density component in high dimensions. As pointed out previously, this is due to the fact that the mass-enhanced HMC method searches the target space by exploiting the geometry of the log target density function via the Hamiltonian dynamics. \square

The tuning of the leapfrog step size, as well as other parameters in Algorithm S1 such as α , L , and N , will be discussed in Section S6.2.

Example S6.3 Previous examples showed that when the mixture components have the same covariance, mass-enhanced HMC can construct Markov chains that hop frequently between the components. Example S6.2 in particular showed that the method works well for high-dimensional target distributions. In general, however, when the mixture components have different covariances, mass-enhanced HMC fails to facilitate jumps between the components. This motivated the main algorithm of this paper (Algorithm 1), tempered Hamiltonian transitions).

If the covariances of the mixture components are not the same, then obviously, the mass matrix M cannot be equal to the inverse of every mixture covariance. Therefore it suffices to show that if M is not equal to the inverse of the covariance matrix Σ , mass-enhanced HMC fails. For simplicity, we consider a Gaussian target distribution, that is, a mixture consisting of a single component. Without loss of generality, we let the covariance Σ be a diagonal matrix. The target space dimension is ten, and the square roots of the diagonal entries of Σ are randomly drawn from the uniform distribution between 0.5 and 4 . The mass matrix M is equal to the identity matrix, and the mass-scaling factor α is equal to 2000 . Starting from a point randomly drawn from the target distribution $\mathcal{N}(0, \Sigma)$, an example path was simulated with mass $\tilde{M} = \alpha M = 2000I$ and leapfrog step size $\tilde{\epsilon} = 0.1\sqrt{\alpha} = \sqrt{20}$. The Hamiltonian evaluated at every leapfrog step is shown in Figure S-6. The Hamiltonian values

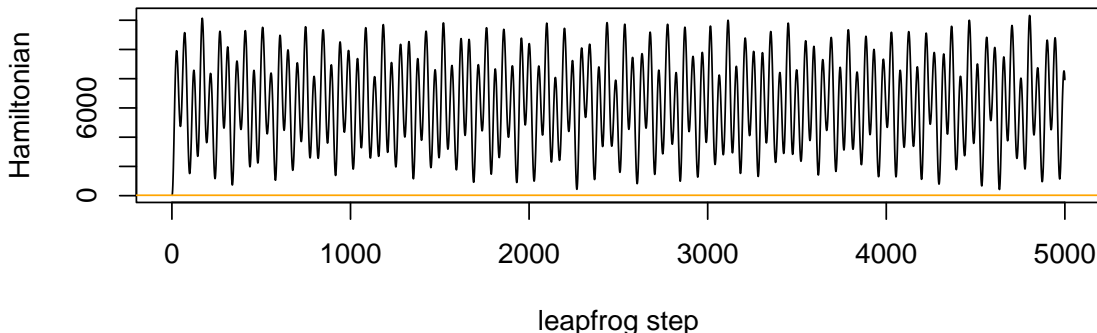


Figure S-6: The Hamiltonian evaluated along an example path for the ten-dimensional Gaussian target distribution $\mathcal{N}(0, \Sigma)$ considered in Example S6.3 where the mass matrix M is not equal to Σ .

are consistently higher than the initial value indicated by the yellow horizontal line. This result indicates that when the mass matrix M is not equal to the inverse of the covariance matrix, the simulated paths with enhanced mass may not reach an acceptable state for a very long time. A theoretical analysis shows that this is the case in general when M is not a scalar multiple of Σ^{-1} (see Section S6.3.2). \square

S6.2 Tuning of parameters

S6.2.1 Mass–time scale equivariance and the choice of leapfrog step size

We consider a transformation of variables that offers insight into tuning of the leapfrog step size for mass-enhanced HMC. The following lemma is a consequence of what we call *mass–time scale equivariance* (see Section 3.1 in the main text).

Lemma S2. *The leapfrog method constructs the same path when simulating the Hamiltonian dynamics with M , initial velocity $v(0)$, and step size ϵ and when simulating it with mass $\tilde{M} = \alpha M$, initial velocity $\alpha^{-1/2}v(0)$, and step size $\check{\epsilon} = \alpha^{1/2}\epsilon$.*

Proof. Consider a transformation of variables given by

$$\begin{aligned}\check{t} &= \alpha^{1/2}t, \\ \check{v} &= \alpha^{-1/2}v.\end{aligned}\tag{10}$$

Then we can see that the following differential equations hold:

$$\begin{aligned}\frac{dx}{d\check{t}} &= \alpha^{-1/2}\frac{dx}{dt} = \alpha^{-1/2}v = \check{v}, \\ \frac{d\check{v}}{d\check{t}} &= \frac{\alpha^{-1/2}}{\alpha^{1/2}}\frac{dv}{dt} = \alpha^{-1}M^{-1}\frac{\partial U}{\partial x} = \check{M}^{-1}\frac{\partial U}{\partial x}.\end{aligned}\tag{11}$$

Thus the transformed variables $(x, \check{v}, \check{t})$ is a solution to the same differential equations as the HEM (11) with mass \check{M} . This mass-time scale equivariance implies that the discrete-time numerical simulation described by (3) with LF step size

$$\check{\epsilon} = \alpha^{1/2}\epsilon$$

and initial state $(x(0), \check{v}(0)) = (x(0), \alpha^{-1/2}v(0))$ and mass \check{M} constructs the same path as the LF numerical simulation with mass M , initial condition $(x(0), v(0))$, and step size ϵ . We can see this explicitly from the following equations:

$$\begin{aligned} \check{v}\left(\check{t} + \frac{\check{\epsilon}}{2}\right) &= \alpha^{-1/2}v\left(t + \frac{\epsilon}{2}\right) = \alpha^{-1/2}v(t) - \alpha^{-1/2}\frac{\epsilon}{2}M^{-1}\nabla U(x(t)) \\ &= \check{v}(\check{t}) - \frac{\check{\epsilon}}{2}(\alpha M)^{-1}\nabla U(x(\check{t})), \\ x(\check{t} + \check{\epsilon}) &= x(t + \epsilon) = x(t) + \epsilon v\left(t + \frac{\epsilon}{2}\right) \\ &= x(t) + \alpha^{-1/2}\check{\epsilon}\alpha^{1/2}\check{v}\left(\check{t} + \frac{\check{\epsilon}}{2}\right) \\ &= x(\check{t}) + \check{\epsilon}\check{v}\left(\check{t} + \frac{\check{\epsilon}}{2}\right), \\ \check{v}(\check{t} + \check{\epsilon}) &= \alpha^{-1/2}v(t + \epsilon) = \alpha^{-1/2}v\left(t + \frac{\epsilon}{2}\right) - \alpha^{-1/2}\frac{\epsilon}{2}M^{-1}\nabla U(x(t + \epsilon)) \\ &= \check{v}\left(\check{t} + \frac{\check{\epsilon}}{2}\right) - \frac{\check{\epsilon}}{2}(\alpha M)^{-1}\nabla U(x(\check{t} + \check{\epsilon})). \end{aligned}$$

Furthermore, since there is a one-to-one correspondence between the coordinate systems (t, x, v) and $(\check{t}, x, \check{v})$, the numerical simulation of $(\check{t}, x, \check{v})$ is stable if and only if the numerical simulation of (t, x, v) is stable. \square

Lemma S2 suggests a tuning of the leapfrog step size given by $\check{\epsilon} = \sqrt{\alpha}\epsilon$ for Algorithm S1. However, we note that Algorithm S1 simulates the HEM with the initial velocity $v(0)$ instead of $\check{v}(0) = \alpha^{-1/2}v(0)$. Thus it constructs the same as that obtained by numerically simulating the Hamiltonian dynamics with mass M and *increased* initial velocity $\alpha^{1/2}v(0)$. The mass-time scale equivariance (12) shows that the following two ways of enhancing the initial kinetic energy $K(v(0)) = \frac{1}{2}v(0)^\top Mv(0)$ by a factor of α are equivalent:

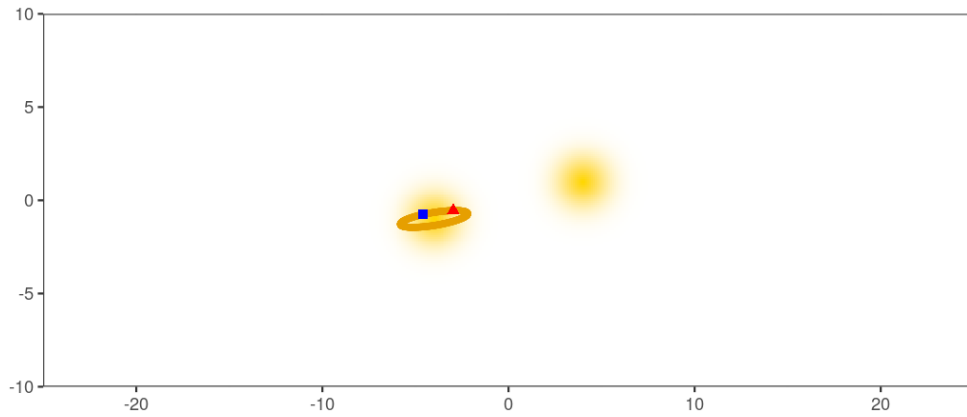
1. increase the mass from M to αM , or
2. increase the initial velocity from $v(0)$ to $\alpha^{1/2}v(0)$.

If the curvature of the potential energy function is not constant, the suggested scaling $\check{\epsilon} = \sqrt{\alpha}\epsilon$ may lead to numerical instability, because the Hessian at $x(\epsilon) = x(0) + \epsilon\alpha^{1/2}v(0)$ may differ greatly from the Hessian at $x(0)$. In this case, $\check{\epsilon}$ may need to be chosen smaller than $\alpha^{1/2}\epsilon$.

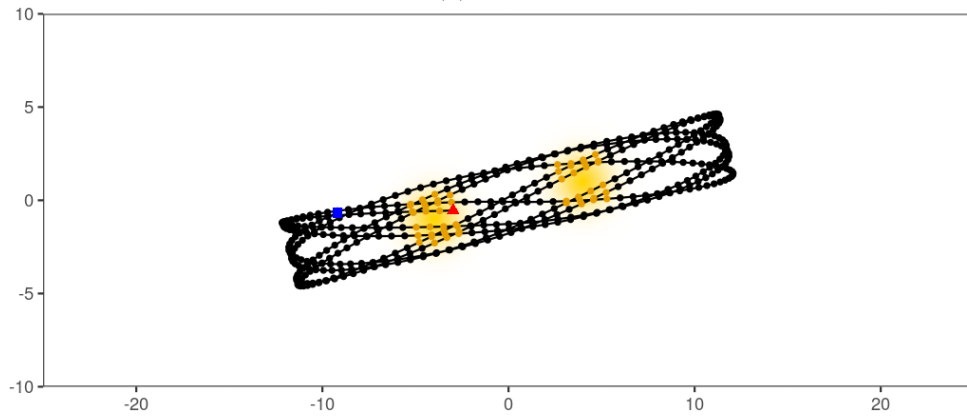
S6.2.2 The choice of α , L , N

In mass-enhanced HMC with sequential proposals (Algorithm S1), the mass scale factor α implicitly determines the search scope for separated density components. Since $U(x(t)) + \check{K}(v(t))$ is approximately conserved on the simulated path, every point on the path satisfies

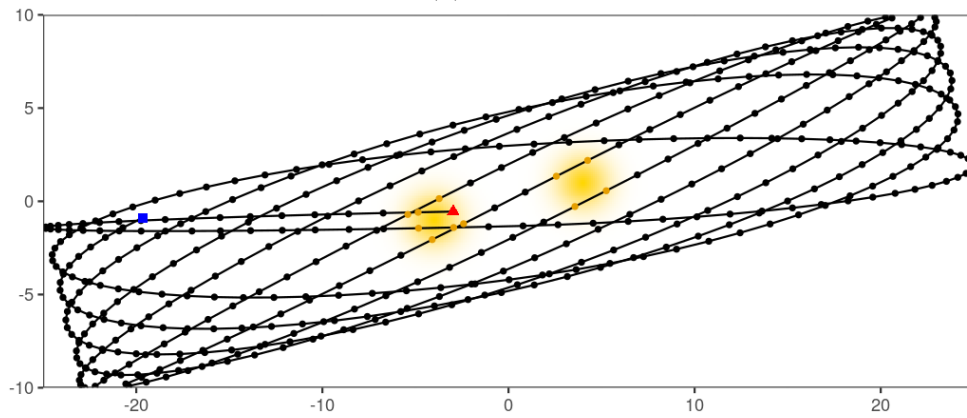
$$U(x(t)) \lesssim U(x(0)) + \alpha K(v(0)), \quad (\text{S11})$$



(a) $\alpha = 1$



(b) $\alpha = 30$



(c) $\alpha = 200$

Figure S-7: Numerically simulated Hamiltonian paths with varied mass scale factor α for a mixture of two normal target density considered in Example S6.4. The two modes of the target distribution are represented by yellow color gradient. Acceptable points when the uniform $(0, 1)$ random number Λ is equal to 0.5 is shown as orange dots. The initial position is marked by a red triangle, and the 500-th position by a blue square.

Parameter	Description	Tuning guidelines
α	Mass scale factor	The simulated paths should be able to reach the desired search scope for isolated modes.
ϵ	Leapfrog step size	As large as possible while ensuring that the numerical simulation is stable ($\check{\epsilon} = \sqrt{\alpha} \cdot \epsilon$).
L	Number of acceptable proposals to be found in each iteration	Large enough so that the simulated path can escape the local basin it starts from.
N	Maximum number of proposals to be made in each iteration	Large enough so that the simulated path can reach a new density component, while ensuring that the algorithm is not excessively slowed down in case $v(0)$ and Λ are drawn unfavorably.

Table S-1: Tuning guidelines for parameters in Algorithm S1

where $K(v(0)) \sim \frac{1}{2}\chi_d^2$. Therefore, with increasing α , the area reachable by the simulated paths are expanded, and the depth of the potential energy barrier that can be crossed is increased.

Example S6.4 Figure S-7 shows the simulated Hamiltonian paths with mass enhancement ratios $\alpha = 1, 30$, and 200 where the target distribution π is a mixture of two Gaussian density components:

$$\pi(x) = \frac{1}{2}\phi\{x; (-4, -1), I_{2 \times 2}\} + \frac{1}{2}\phi\{x; (4, 1), I_{2 \times 2}\}. \quad (\text{S12})$$

Here $\phi(x; \mu, I_{2 \times 2})$ denotes the multivariate Gaussian density with mean μ and the covariance matrix equal to the two dimensional identity matrix. All three paths start with the same initial velocity $v(0)$. The points on the numerically simulated paths are marked by orange dots if they are acceptable according to the criteria $H(x, v) < H\{x(0), v(0)\} - \log \Lambda$, where the Uniform(0,1) random number Λ is assumed to take value 0.5. Figure S-8 plots the potential energy, the kinetic energy, and the Hamiltonian of the points along the simulated path where the mass is either M or $\check{M} = \alpha M$ where $\alpha = 30$. The Hamiltonian H with mass \check{M} , indicated by the dashed black line, is approximately constant, but the Hamiltonian \check{H} with mass M , indicated by the solid black line, fluctuates depending on the proportions of \check{H} made up by the potential energy U and the kinetic energy \check{K} . A point on the path is acceptable if the Hamiltonian H is less than $H(x(0), v(0)) - \log \Lambda$, which is indicated by the green horizontal line.

When $\alpha = 1$ (Figure S-7a), the Hamiltonian path does not leave the density component where the current state of the Markov chain is located. However, the simulated paths can move across the region of low target density between the two modes when $\alpha = 30$ (Figure S-7b). If α is even greater ($\alpha = 200$), the simulated Hamiltonian path reaches a wider area (Figure S-7c). Since the simulated path traverses a wider area when $\alpha = 200$, the proportion of acceptable states along the path may be smaller than when $\alpha = 30$. Thus tuning $\alpha = 30$ may lead to more efficient sampling than $\alpha = 200$ for this target density given by (S12). However, if there was another density component at a remote location (say at $(-20, -5)$), the simulation with $\alpha = 200$ would be able to reach it whereas that with $\alpha = 30$ would not. Therefore, the mass enhancement ratio α may be chosen based on the desired search scope for isolated modes. The search area is dependent on the geometry of the surface of the log

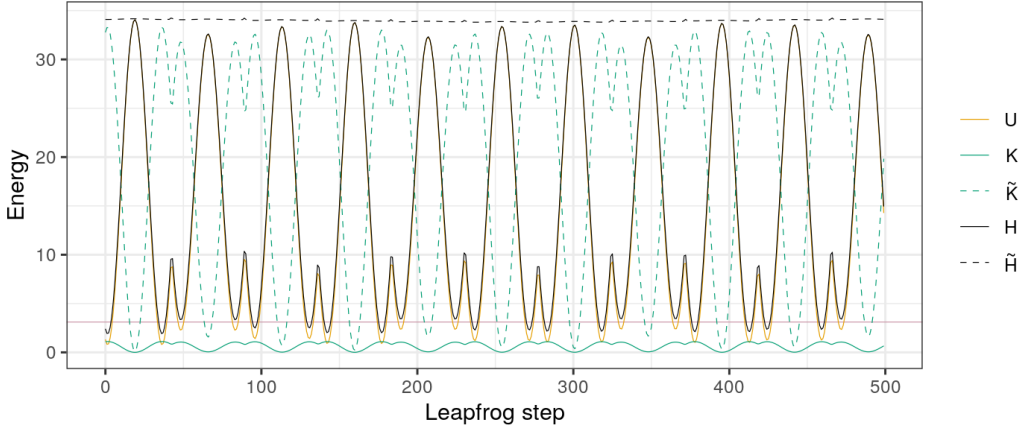


Figure S-8: The traceplots for $U(x(t))$, $K(v(t))$, $\tilde{K}(v(t))$, $H\{x(t), v(t)\}$, and $\tilde{H}\{x(t), v(t)\}$ for the simulated path shown in Figure S-7b. The horizontal line at around 3 marks the acceptability criterion $H\{x(0), v(0)\} - \log(0.5)$, assuming that $\Lambda = 0.5$.

target density function. In Figure S-7b and S-7c, the simulated Hamiltonian paths stay along the direction connecting the two density modes, where the potential energy is relatively low. Algorithm S1 is assisted by the local geometry of the potential energy landscape so that it can efficiently search for isolated modes regardless of the space dimension.

Insight into the simulated paths can be gained by looking at the traceplot of $H\{x(t), v(t)\}$. Figure S-8 shows the traceplots for $U(x(t))$, $K(v(t))$, $H\{x(t), v(t)\}$, $\tilde{K}(v(t))$, and $\tilde{H}\{x(t), v(t)\}$ for the simulated path for $\alpha = 30$ (Figure S-7b). The value of $\tilde{H}\{x(t), v(t)\} = U(x(t)) + \tilde{K}(v(t))$ is approximately constant, whereas the value of $H\{x(t), v(t)\}$ is mostly affected by $U(x(t))$. For numerically stable paths, $U(x(t))$ and $K(v(t))$ should have oscillatory traceplots. Acceptable points are those for which $H\{x(t), v(t)\}$ is less than $H\{x(0), v(0)\} - \log \Lambda$, and those points occur periodically. \square

The parameter L in Algorithm S1 should be chosen large enough that the simulated path may leave the local mode it starts from. This makes it more likely that the next state of the constructed Markov chain, which is the L -th acceptable proposal along the path, is found in a different density component. In Figure S-7b, the simulated path starts from the red triangle and leaves the acceptable region around the first density component in four steps. Thus in this case, if L is suitably large, say $L \geq 4$, the next state of the constructed Markov chain may be found near the other mode located at $(4, 1)$.

The parameter N sets an upper bound on the simulation time per iteration. Therefore, it needs to be large enough to allow the simulated path to reach a remote density component. However, in some cases such as when the log density surface is flat, the simulated path may head to a wrong direction for a prolonged amount of time. Moreover, in rare cases where the current state of the Markov chain is close to the maximum of the target density and the drawn uniform random number Λ is close to one, acceptable points may only be found in a very small area of \mathbf{X} where the target density is higher than the starting point. The parameter N needs to be set appropriately so as to avoid spending an excessive amount of time on finding an acceptable candidate in these unfavorable cases. Table S-1 summarizes the parameters in the algorithm and guidelines for tuning parameters.

S6.3 Theoretical explanations of when mass-enhanced HMC does and does not work

S6.3.1 The case where mass-enhanced HMC works

The fact that mass-enhanced HMC can construct globally mixing Markov chains for high-dimensional target distributions of the form

$$\pi(x) = \frac{1}{2} \sum_{j=1}^2 \phi(x; \mu_j, I), \quad x \in \mathbb{R}^d$$

as in Example S6.2 can be mathematically explained as follows. The target density is proportional to

$$\pi(x) \propto e^{-\|x-\mu_1\|^2/2} + e^{-\|x-\mu_2\|^2/2} =: c_1(x) + c_2(x),$$

where without loss of generality we assume that

$$\mu_1 = (\mu_1^1, 0, \dots, 0), \quad \mu_2 = (\mu_2^1, 0, \dots, 0).$$

For simplicity we suppose $M = I$. We have

$$\frac{\partial U}{\partial x} = -\frac{\partial}{\partial x} \log \pi(x) = \frac{c_1(x) \cdot (x - \mu_1) + c_2(x) \cdot (x - \mu_2)}{c_1(x) + c_2(x)},$$

or

$$\frac{\partial U}{\partial x_i} = \begin{cases} \frac{c_1(x)(x_1 - \mu_1^1) + c_2(x)(x_1 - \mu_2^1)}{c_1(x) + c_2(x)} & \text{for } i = 1 \\ x_i & \text{for } i \geq 2. \end{cases}$$

Thus for $i \geq 2$ the Hamiltonian equations of motion for (x_i, v_i) can be solved independently:

$$\frac{dx_i}{dt} = v_i, \quad \frac{dv_i}{dt} = -\check{M}^{-1} \frac{\partial U}{\partial x_i} = -\alpha^{-1} x_i.$$

The solution is given by

$$x_i(t) = A_i \sin(\omega t + \varphi_i), \quad v_i(t) = A_i \omega \cos(\omega t + \varphi_i)$$

where $\omega = \sqrt{\alpha^{-1}}$. The amplitude A_i satisfies

$$A_i^2 = x_i(0)^2 + \omega^{-2} v_i(0)^2 = x_i(0)^2 + \alpha v_i(0)^2,$$

and the initial phase $\varphi_i \in [0, 2\pi)$ satisfies

$$x_i(0) = A_i \sin(\varphi_i), \quad v_i(0) = A_i \omega \cos(\varphi_i)$$

Since $\omega = \sqrt{\alpha^{-1}} \gg 1$ and both $x_i(0)$ and $v_i(0)$ are random draws from $\mathcal{N}(0, 1)$, the value of $\sin \varphi$ is close to zero and $\cos \varphi$ is close to one.

For $i = 1$, we can consider a division of the space into three regions, $R_1 = \{x; c_1(x) \gg c_2(x)\}$, $R_2 = \{x; c_1(x) \ll c_2(x)\}$, and $R_3 = (R_1 \cup R_2)^c$. Since both $c_1(x)$ and $c_2(x)$ are exponential quadratic functions of x , most points in the space belongs to either the first or

the second region. Suppose without loss of generality that $x(0)$ belongs to R_1 . In this region, $(x_1(t), v_1(t))$ approximately has a similar form as that for $i \leq 2$, namely

$$x_1(t) - \mu_1^1 = A_1 \sin(\omega t + \varphi_1), \quad v_1(t) = A_1 \omega \cos(\omega t + \varphi_1).$$

As the path enters the region R_3 , the amplitude and the phase change in a way that is hard to predict, but after the path passes through R_3 and enters R_2 the solution becomes again approximately sinusoidal:

$$x_1(t) - \mu_2^1 = A_1' \sin(\omega t + \varphi_1'), \quad v_1(t) = A_1' \omega \cos(\omega t + \varphi_1').$$

The Hamiltonian in R_2 can be expressed as

$$\begin{aligned} H(t) &\approx \frac{1}{2} \|x - \mu_2\|^2 + \frac{1}{2} \|v\|^2 \\ &= \frac{1}{2} (x_1 - \mu_2^1)^2 + \frac{1}{2} v_1(t)^2 + \sum_{i \geq 2} \left[\frac{1}{2} x_i(t)^2 + \frac{1}{2} v_i(t)^2 \right] \\ &= \left\{ \frac{1}{2} A_1'^2 \sin^2(\omega t + \varphi_1') + \frac{1}{2} A_1'^2 \omega^2 \cos^2(\omega t + \varphi_1') \right\} + \left\{ \sum_{i \geq 2} \left[\frac{1}{2} A_i^2 \sin^2(\omega t + \varphi_i) + \frac{1}{2} A_i^2 \omega^2 \cos^2(\omega t + \varphi_i) \right] \right\} \\ &:= H_1(t) + H_{i \geq 2}(t) \end{aligned}$$

Since the angular frequency is the same and equal to ω for all $i \geq 2$, the second term can be expressed as

$$H_{i \geq 2}(t) = B^0 + B^1 \cos(2\omega t + \theta) \quad (\text{S13})$$

for some constants B^0, B^1 , and θ . Therefore, $\Delta H_{i \geq 2}(t) := H_{i \geq 2}(t) - H_{i \geq 2}(0)$ periodically becomes zero or negative value with frequency ω/π , regardless of the dimension d . The quantity $H_1(t)$ is also periodic with frequency ω/π . Therefore if φ_1' is such that both $\Delta H_1(t)$ and $\Delta H_{i \geq 2}(t)$ can be simultaneously small at some point, that point can be accepted with a reasonably large probability. As α increases, $H_{i \geq 2}(0)$ becomes closer to the minimum of its cycle, and the combined phase θ in (S13) approaches π . Thus the range of ωt for which $\Delta H_{i \geq 2}$ is below zero becomes narrower, and the chance that a point is accepted during the time a path stays in R_2 decreases. In this case, many re-entering into R_2 may be necessary before the phase φ_1' takes a fortunate value that allows a point on the path to be accepted. In conclusion, as the distance between the two modes $\|\mu_1 - \mu_2\|$ increases, a larger value of α will need to be used in order to enable the simulated path to reach a different mode, and the probability of accepted jump from one mode to another decreases. However, the jump probability is not sensitive to the space dimension d ; this conclusion is consistent with the results shown in Figure S-5.

S6.3.2 The case where mass-enhanced HMC does not work

Now we consider the case where mass-enhanced HMC does not work well; Example S6.3 illustrates this case. Consider again a unimodal Gaussian distribution $\mathcal{N}(0, \Sigma)$ where Σ is not equal to a scalar multiple of the mass inverse matrix M^{-1} . Using the linear transformation (S9), we can simplify the case such that $M = I$ and Σ is anisotropic (i.e., not a scalar multiple

of the identity matrix). Without loss of generality, suppose that Σ is diagonal with entries σ_{ii}^2 , $i = 1, \dots, d$ and that these d variances are all different. The solution to the Hamiltonian equations of motion

$$\frac{dx_i}{dt} = v_i, \quad \frac{dv_i}{dt} = -\check{M}^{-1} \frac{\partial U}{\partial x_i} = -\alpha^{-1} \sigma_{ii}^{-2} x_i$$

for the i -th component is given by

$$x_i(t) = A_i \sin(\omega_i t + \varphi_i), \quad v_i(t) = A_i \omega_i \cos(\omega_i t + \varphi_i)$$

where $\omega_i = \sqrt{\alpha^{-1} \sigma_{ii}^{-1}}$. If $\alpha \gg 1$, the d components are almost in sync, because

$$\frac{\sin(\varphi_i)}{\cos(\varphi_i)} = \frac{x_i(0)}{v_i(0)} \omega_i = \frac{x_i(0)}{v_i(0)} \sqrt{\alpha^{-1} \sigma_{ii}^{-1}} \approx 0, \quad \forall i.$$

However, as time progresses, the d components become asynchronized due to the fact that ω_i are all different. It takes an exponentially long time in d for all the components to be in sync again. Therefore for $\alpha \gg 1$ and large d , the increase in Hamiltonian $\Delta H(t)$ is consistently large for a very long time. This phenomenon was demonstrated by Example [S6.3](#).

S7 Tempered Hamiltonian Monte Carlo with sequential proposals

The sequential proposal strategy proposed by [Park and Atchadé \[2020\]](#) can be employed by tempered Hamiltonian Monte Carlo (Algorithm [1](#)). However, incorporating the sequential proposal strategy into tempered HMC did not substantially improve the numerical results in our experiments. Here we briefly describe the method and provide a pseudocode for tempered HMC with sequential proposal (Algorithm [S2](#)) for potential interest in this idea.

Tempered HMC with sequential proposals (Algorithm [S2](#)) targets the extended target density given by

$$\Pi(x, k, \check{v}) := \bar{\pi}(x) \psi_K(k) \phi(\check{v}; 0, \alpha_k^{-1} M^{-1}),$$

where $\phi(\cdot; 0, \alpha_k^{-1} M^{-1})$ denotes the multivariate normal density with mean 0 and variance $\alpha_k^{-1} M^{-1}$. The discrete distribution $\psi_K(k)$ defined on the space of integers modulo K must be symmetric, that is, $\psi_K(k) = \psi_K(-k)$ for all $k \pmod{K}$. The initial value of k and the initial velocity for each iteration step are drawn from the extended target density:

$$k_0 \sim \psi_K(k), \quad \check{v}(0) \sim \mathcal{N}(0, \alpha_{k_0}^{-1} M^{-1}).$$

We consider the extended Hamiltonian defined by

$$H^{\text{mod,sp}}(x, k, \check{v}) = U(x) - \log \psi_K(k) + \frac{1}{2} \check{v}^\top \{\alpha_k M\} \check{v} - \frac{1}{2} \log \det \{\alpha_k M\}. \quad (\text{S14})$$

Since the maximum increase in $\eta(t)$ along a simulated path relative its starting value determines the search scope, it is beneficial to start the path at the smallest values of $\eta(t)$. Thus, the distribution on k of the form

$$\psi_K(k) = \frac{\mathbf{1}[\eta_k \leq c]}{\sum_{k'=1}^K \mathbf{1}[\eta_{k'} \leq c]} \quad \text{for some } c$$

Algorithm S2: Tempered Hamiltonian Monte Carlo with sequential proposals

Input : Potential energy function $U(x) = -\log \pi(x)$; Mass matrix, M ; Mass scaling schedule, $\{\alpha_k = e^{2\eta k}; k = 0, \frac{1}{2}, 1, \dots, K - \frac{1}{2}, K\}$; Baseline leapfrog step size, $\bar{\epsilon}$; Simulation time scale coefficient, a ; Length of constructed Markov chain, I ; Discrete distribution $\psi_K(k)$ on $0 : (K-1)$; Maximum number of candidate proposals per iteration step, N ; Number of acceptable states to be found per iteration step, L

```
1 Initialize: Set  $X^{(0)}$  arbitrarily
2 for  $i \leftarrow 0 : I-1$  do
3   Draw  $\Lambda \sim \text{Uniform}(0, 1)$ 
4   Draw  $k_0 \sim \psi_K(k)$ 
5   Let  $Y_0 \leftarrow X^{(i)}$  and draw  $W_0 \sim \mathcal{N}(0, \alpha_{k_0}^{-1} M^{-1})$ 
6   Let  $H_0 \leftarrow H(Y_0, k_0, W_0)$  where  $H$  is defined in (S14)
7   Let  $X^{(i+1)} \leftarrow X^{(i)}$ , for the case where fewer than  $L$  acceptable states were found
8   Let  $n_{acc} \leftarrow 0$ , the number of acceptable candidate states found
9   for  $n \leftarrow 1 : N$  do
10    Set  $\check{\epsilon} \leftarrow \bar{\epsilon} \cdot \alpha_{k_0+n-\frac{1}{2}}^a$ 
11     $(Y_n, W_n) \leftarrow \Psi_{\check{\epsilon}}(Y_{n-1}, W_{n-1}; \alpha_{k_0+n-\frac{1}{2}} M, \check{\epsilon})$  obtained by carrying out one
    leapfrog step (3) from  $(Y_{n-1}, W_{n-1})$  with mass  $\alpha_{k_0+n-\frac{1}{2}} M$  and step size  $\check{\epsilon}$ 
12    if  $\Lambda < \exp\{-H^{\text{mod,sp}}(Y_n, k_0+n, W_n) + H^{\text{mod,sp}}(Y_0, k_0, W_0)\}$  then
13      |  $n_{acc} \leftarrow n_{acc} + 1$ 
14    end
15    if  $n_{acc} = L$  then
16      | Set  $X^{(i+1)} \leftarrow Y_n$ 
17      | break
18    end
19  end
20 end
Output: A draw of Markov chain,  $(X^{(i)})_{i \in 1 : I}$ 
```

can lead to a higher mode hopping frequency. This choice has an additional advantage that it can reduce the number of Hamiltonian evaluations. The Hamiltonian $H^{\text{mod,sp}}(Y_n, k_0+n, W_n)$ is evaluated in line 12 of Algorithm S2 to check if a proposed candidate is acceptable. The evaluation of the Hamiltonian is only necessary for k_0+n in the support of ψ_K , because otherwise the $-\log \psi_K(k_0+n)$ term in the Hamiltonian function is equal to infinity.

Supplementary References

- R. M. Neal. Sampling from multimodal distributions using tempered transitions. *Statistics and computing*, 6(4):353–366, 1996.
- R. M. Neal. MCMC using Hamiltonian dynamics. In S. Brooks, A. Gelman, G. Jones, and X.-L. Meng, editors, *Handbook of Markov chain Monte Carlo*, pages 113–162. CRC press, 2011.
- J. Park and Y. F. Atchadé. Markov chain Monte Carlo algorithms with sequential proposals. *Statistics and Computing*, 2020.